ANNALES
UNIVERSITATIS SCIENTIARUM BUDAPESTINENSIS DE ROLANDO EÖTVÖS NOMINATAE

SECTIO GEOLOGICA

TOMUS XX.
1978

REDIGUNT
B. GÉCZY
J. KISS
L. STEGENA

BUDAPEST
1978

ANNALES

UNIVERSITATIS SCIENTIARUM BUDAPESTINENSIS DE ROLANDO EÖTVÖS NOMINATAE

SECTIO BIOLOGICA
incepit anno MCMLVII

SECTIO CHIMICA
incepit anno MCMLIX

SECTIO GEOLOGICA
incepit anno MCMLVII

SECTIO GEOGRAPHICA
incepit anno MCMLVII

SECTIO HISTORICA
incepit anno MCMLVII

SECTIO IURIDICA
incepit anno MCMLIX

SECTIO LINGUISTICA
incepit anno MCMLXIX

SECTIO MATHEMATICA
incepit anno MCMLVIII

SECTIO PAEDAGOGICA ET PSYCHOLOGICA
incepit anno MCMLXX

SECTIO PHILOLOGICA
incepit anno MCMLVII

SECTIO PHILOSOPHICA ET SOCIOLOGICA
incepit anno MCMLXII

ON THE AGE OF THE RZEHAKIA-BEDS AND GARÁB SCHLIER BASED ON FORAMINIFERA AND NANNOPLANKTON INVESTIGATIONS

M. HORVÁTH and A. NAGYMAROSY

Department of Geology, Eötvös University, Budapest

Received: April 1978

SUMMARY

Microflora – and fauna – studies of schlier and Rzehakian strata of Carpathian age are dealt with, carried out on the surface as well as on deep drilling profiles of the Salgótarján basin and of the area of Northern-Mátra. It has been stated that both overlying coal bed and the schlier should be placed into the NN 4 nannozone. Within the Carpathian foraminiferal fauna four associations have been separated, these being also indicators of facies. On the basis of the studies the Garáb Schlier can be well correlated with several Austrian and Slovakian sites.

1. Introduction

Some surface localities and borehole profiles of Karpatian age from the territory of the Northern-Mátra and the Salgótarján basin were examined in the last years.

The geological features and occurence of these formations are relatively wellknown, but paleontologically they are rather poorly investigated. Though a great number of authors have been dealing with the macrofauna of the Salgótarján Brown-coal Formation, of the Cardium-, Rzehakia- and Chlamys-bearing sandstones and of the Garáb Schlier (without a claim for completeness: Bartkó L., 1961–62; Csepreghyné Meznerics I., 1951, 1954, 1960; Horuschitzky F., 1939; id. Noszky J., 1930; Schréter Z., 1940, the number of the publications on the foraminiferafauna of these formations is negligible. (The comprehensive list of the foraminifera species and their references are collected in Balogh et al. 1966. pp. 52–65, and Alföldy L. et al. 1975. pp. 140–150.). The nannofloras of Karpatian age of North-Hungary were described by Báldi-Beke M. (1960) from point-like exposures. Besides those mentioned above a lot of unpublished paleontological data can be found in the documentations of the deep-drilling profiles.

Our paper will give some nannofloras and foraminiferafaunas of the Rzehakia-beds and the Garáb Schlier, and we make an attempt to emplace these formations in the Standard Neogene Nannoplankton Zonation.

2. The geology of the territory and profiles studied

2.1. The higher regressive part of the Nógrád Glauconitic Sandstone is overlain by the Zagyvapálfalva Red Beds in the Salgótarján Basin and in the surroundings of Mátraalmás. In the Recsk area the latter formation does not occur. The Gyulakeszi Rhyolith-Tuff Formation (lower rhyolith tuff) is covered by the Salgótarján Brown-Coal Formation, which is wedged out towards the basin edges. The Brown-Coal Formation is overlain by the brackish water Cardium- and Rzehakia-bearing and marin Chlamys-bearing sandstones, finally by the pelitic Garáb Schlier, which is expanded far beyond the borders of the territory dealt with. The stratigraphically higher regressive part of the Schlier is covered by the Tar Rhyolith-Tuff Formation (middle rhyolith tuff) and Mátra Andesite Formation of Badenian age.

According to the statement of the Miocene Subcommission of the Hungarian Stratigraphical Committee – proposition of G. Hámor 1977- the age of the lower rhyolith tuff, the brown-coal series and the Cardium Rzehakia beds is Ottnangian, the age of the Chlamys-bearing sandstone and of the Schlier is Karpatian.

2.2. *The borehole profiles studied in the Mátraalmás area* (Fig. 1)

The T – 9. borehole, which penetrated the most complete profile, terminated in the Ilonavölgy Sandstone (a part of Nógrád Sandstone) of Eggenburgian age. It is followed upwards by a thin red bed, which is lacking in the other profiles. The lower rhyolith tuff is supposed to be not deposited into water, but in the higher part of borehole T – 4. it shows some traces of water movement and yields conglomerates. The brown coal series – in contrary to its mid-basin development – has only one coal layer The overlying stratas consist of tuff, tuffit, tuffitic sandstone with a thickness between 20 – 50 meters, which yield only few fossils. These stratas are covered by the thick sandy, clayey silt (Garáb Schlier Formation), which in its lower (transgressive) and higher (regressive) part has Arca- and Corbula-bearing middle- and fine-grained sandstone-interbeddings. (The genus were determined by Mrs. Bohn – Havas). None of the three boreholes in Mátraalmás penetrated the covering volcano-series of Badenian age.

2.3. *The profiles of the Recsk – 103, -109 and the Sirok – 1 boreholes*

The most complete profiles in the Recsk area were penetrated by the Rm – 103 borehole, but the profile of the Rm – 109 is also very similar Both profiles are yielding the complete Oligocene series with faunas and nannofloras. The Oligocene stratas are covered by the Ilonavölgy Sandstone (Nógrád Glauconitic Sandstone) of Eggenburgian age and further by the lower rhyolith tuff. The red beds in the Recsk area are lacking. The transgressive basal stratas of the Tertiary in the borehole Sirok – 1 are laying

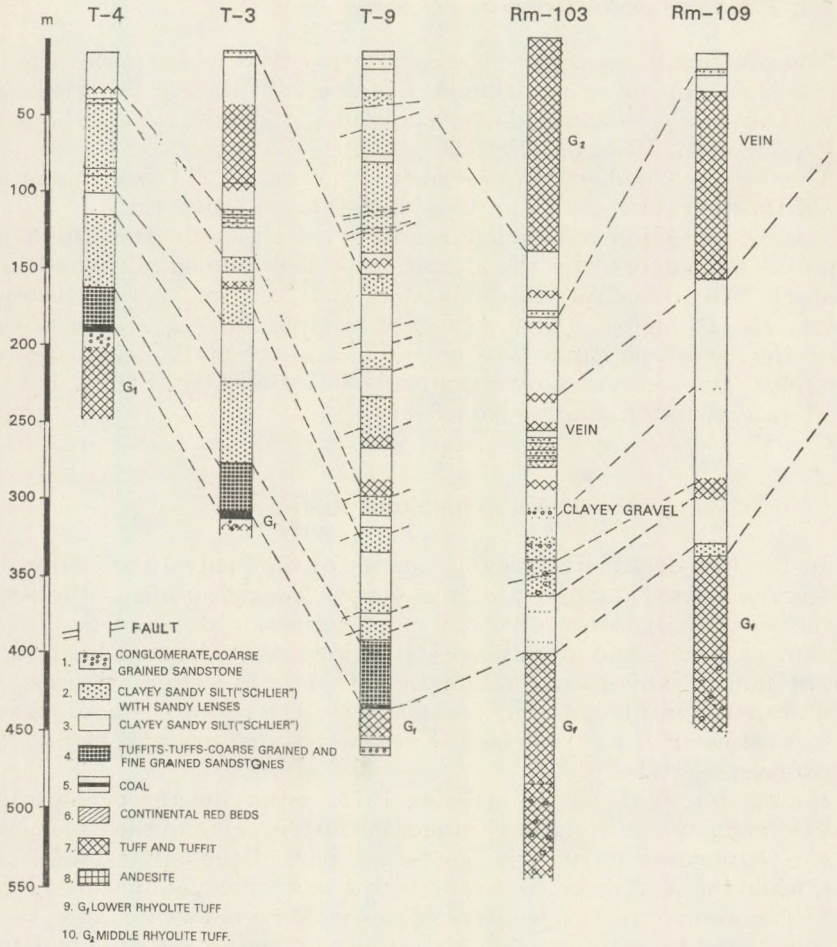

Fig. 1. Profiles of the T – 3, T – 4 and T – 9 boreholes from the Mátraalmás, Rm – 103, Rm – 109 boreholes from the Recsk area.

immediately on the diabase of the mesozoic basement and are consisting of reworked clastics of sandy rhyolith tuff.

All of the three boreholes penetrated the Garáb Schlier in different thicknesses (270 meter in the Rm – 103, 180 meter in the Rm – 109, 130 meter in the Sirok – 1 boreholes). The Schlier has some thin sandy interbeddings and is penetrated by some thin andesite-dykes too. The covering layers of middle rhyolith tuff are 70 m thick in the profile Sirok – 1 and 150 meter thick in the Rm – 103 section. The youngest formation of the area, the Mátra Andesite was observed only in the Sirok – 1 profile.

2.4. *The "Ottnangian" exposure of Kazár*

The covering formations of the Salgótarján Brown Coal Series and the Garáb Schlier crop out in a thickness of 34 m east of the gipsy's row Kazár village. The profile is described and represented in details by G. Hámor (in Papp et al. 1973, pp. 206–209.).

The deepest members of the series on the surface at this moment are a 50 centimeters thick coarse grained sandstone and over this the brown-coal bed No–1. (First nannoplankton sample.) Upwards from this point the profile is composed by the alteration of fine grained clayey silt and sandstone. An abundant Cardium- and Rzehakia-fauna was observed between 13–16 meters. (Nannoplankton samples No–2–7.) In dip direction the sandstone banks became absent and the grain structure turns to be finer. The series goes over gradually into the Garáb Schlier Formation. (Nannoplankton samples No–8–14.)

3. Nannoplankton studies

In the last decade the regional stages of the Central Paratethys became more accepted and used also in Hungary. The definitions of the stage-boundaries are based on the entrance or exctinction datas of mollusc or foraminifera species and assemblages. It follows, that the zone boundaries of the Standard Nannoplankton Zonation of Martini and Worsley (1970) do not coincide with the boundaries of the regional stages. Therefore it is necessary to parallelize the regional stage stratotypes and the nannozonation precisely.

Martini et Müller (1975a, 1975b) studying the type-profiles of the Ottnangian and Karpatian stages in Austria came to the conclusion, that the Ottnangian stage corresponds to a part of the nannozones NN 3 and 4, while the Karpatian corresponds to a part of the nannozones NN 4 and 5. The absence of *Sphenolithus belemnos* Bramlette and Wilcoxon raised some difficulties, because its extinction defines the boundary between the zones NN 3 and 4. Consequently the relation between the stage Ottnangian and the nannozonation is unsolved. The *Sphenolithus heteromorphus* Bramlette and Wilcoxon existing in the zones NN 4 and 5, occurs only in some of the examined type localities of the Karpatian. Based on these results, the above mentioned authors have pointed out, that the *Sphenolithus heteromorphus* invaded the Paratethys only in the late Karpatian.

3.1. *The Mátraalmás area* (Tables I–II)

The profiles of boreholes T–3, –4, –9 were sampled at about 10 m intervals. All samples of T–9 borehole (containing the most complete profile) were examined, while a sufficient number of samples were studied from the lowest and highest parts of T–3 and –4 for to enable to place

The nannoplankton in the profile of the borehole T – 9.

	460–461 m	430–431 m	427 m	410–415 m	405–407 m	390–391 m	381–382 m	375–377 m	366–368 m	357–358 m	345–347 m	338–339 m	324–328 m	317–315 m	301–302 m	295–296 m	287–288 m	274–276 m	266–267 m	254–255 m	245–246 m	237–239 m	226–227 m	224–226 m	216–217 m	204–205 m	194–196 m	184–185 m	175–177 m	164–165 m	155–157 m	144–146 m	136–137 m	128–129 m	115–117 m	103–105 m	95–97 m	85–87 m	76–78 m	64–66 m	52–54 m	45–46 m	36–37 m	27–28 m	16–18 m
Reticulofenestra excavata						●	●	●	●	●																																				
R. minuta	●			●	●		●	●	●	●	●	●	●	●	●	●	●	●	●	●	●	●	●	●	●	●	●	●	●	●	●	●	●	●	●	●	●	●	●	●	●	●	●	●
R. pseudoumbilica				●		●	●	●	●	●	●	●	●	●	●	●	●	●	●	●	●	●	●	●	●	●	●	●	●	●	●	●	●	●	●	●	●	●	●	●	●	●	●	●	●
Coccolithus miopelagicus									●	●						●	●	●	●	●				●	●																					
C. pelagicus				●	●	●	●	●	●	●	●	●	●	●	●	●	●	●	●	●	●	●	●	●	●	●	●	●	●	●	●	●	●	●	●	●	●	●	●	●	●	●	●	●	●
C. sp.									●	●								●																●	●	●										
Cyclococcolithus floridanus		●	●				●	●	●	●	●	●	●	●	●	●					●	●	●			●	●	●	●	●	●	●	●	●					●	●	●	●	●	●	●	●
C. leptoporus									●	●								●	●																											
C. rotula																						●																									
Syracosphaera pulchra													●	●																		●	●						●							
Discolithina multipora		●	●	●	●				●	●	●	●	●	●	●			●	●	●	●	●	●			●	●	●	●	●	●	●	●	●	●	●	●	●	●	●	●	●	●	●	●
Helicopontosphaera ampliaperta				●	●	●	●	●	●	●		●	●	●	●	●	●	●	●	●	●	●	●	●	●	●	●	●	●	●	●	●	●	●	●						●	●	●	●
H. euphratis																		●			●													●	●										
H. kamptneri							●	●	●	●	●	●	●	●	●	●	●	●	●	●	●	●	●	●	●	●	●	●	●	●	●	●	●	●	●			●	●	●	●	●	●	●	●
H. cf. wallichi											●	●	●	●	●			●	●	●						●	●	●	●	●									●	●	●	●	●	●	●	●
Thoracosphaera sp.						●							●	●	●	●	●	●	●	●	●			●	●																					
Rhabdosphaera pannonica																						●																								

Table I.

	460—464 m 430—431 m 427 m 410—415 m 405—407 m	390—391 m 381—382 m 375—377 m 366—368 m 357—358 m	345—347 m 338—339 m 324—328 m 317—315 m 301—302 m	295—296 m 287—288 m 274—276 m 266—267 m 254—255 m	245—246 m 237—239 m 226—227 m 224—226 m 216—257 m	204—205 m 194—196 m 184—185 m 175—177 m 164—165 m	155—157 m 144—146 m 136—137 m 128—129 m 115—117 m	103—105 m 95—97 m 85—87 m 76—78 m 64—66 m	52—54 m 45—46 m 36—37 m 27—28 m 16—18 m
Sphenolithus cf. conicus	...	...							
Sph. heteromorphus		.. —	... ..	.. ..			..		
Sph. moriformis	.. ..	.. — ...	....	.. —	... .	... —	.....	— — . —	— .. . —
Braarudosphaera bigelowi			..			...	..	...	
Discoaster adamanteus						..		..	
D. cf. aulakos								..	
D. deflandrei			...				...		
D. divaricatus						..			
D. druggii	...			..		..			..
D. musicus									..
D. trinidadensis					...				
D. variabilis									..
Cricolithus jonesi	— —	..... —	—	— — — —	— — — —	— — — —	— — — —	— — — —	...
Coronocyclus nitescens		... —	..	..	... ...	...	...	...	
Redeposition from Oligocene		.....	...	...		.. —	..... —	.. —	.. ..
Redeposition from Eocene	—	.....	.. —	.....	— — — —	— — — —	.. ... —	— .. — —	— .. — .....
Redeposition from Cretaceous	.. ..	—	.. ..	.. —	— — — —	— — — —	—	... — —	

Rare .....
Some — — —
Common ——
Abundant ——

Table II.

The nannoplakton in the profiles of the boreholes T – 3. and T – 4.

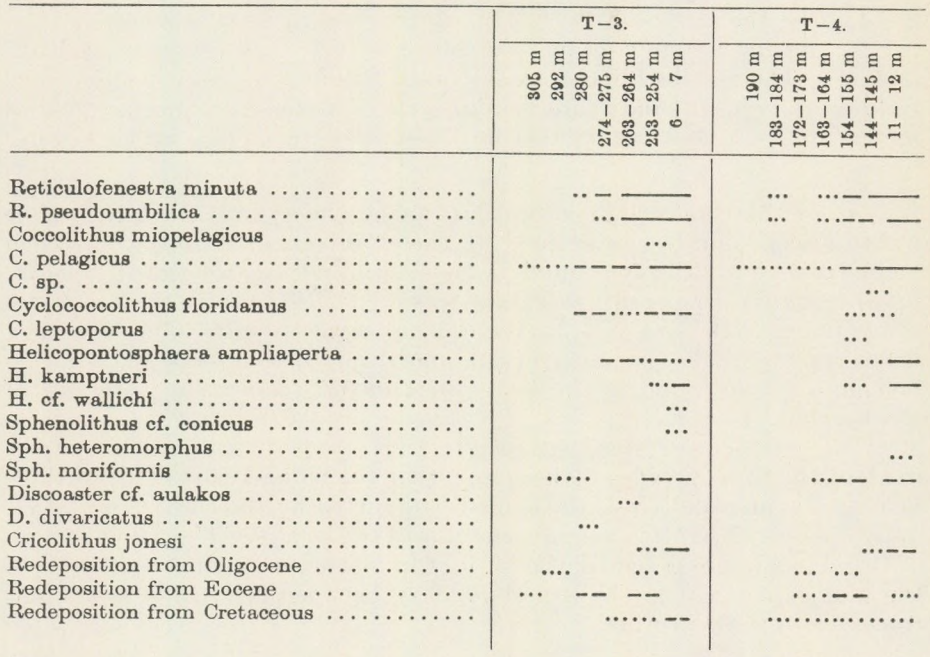

Rare ·····
Some – – –
Common ——
Abundant ——

these into the nannoplankton zonation correctly. The nannofloras are in general less diverse, than the nannofloras of similar facies of Badenian age, but more diverse than those of the Upper Oligocene and Lower Miocene of Hungary. The placoliths (for example *Coccolithus pelagicus, Reticulofenestra pseudoumbilica*, etc.) and *Helicopontosphaeras* are frequent, as well as some other forms (for example *Cricolithus jonesi, Sphenolithus moriformis).* The *Sphenolithus* and *Discoaster* species, characterizing the tropical climate occur only in a restricted number, in contrary to the nannofloras of Badenian age. In our studied material three types of nannoplankton assemblages can be enumerated:

– Samples being practically free of nannofossils or containing only a single redeposited Eocene or Cretaceous species. This represents mainly the 30 meter thick coarse grained clastics covering immediately the brown coal. These sediments are probably of fresh- or brackish water origin (303 280 meters in the T – 3, 190 – 280 meters in the T – 4, 464 – 415 meters in the T – 9 boreholes).

– A probably slightly brackish-water nannoplankton assemblage occurs in the 10 – 20 meter thick transition between the coarse grained

clastics and the Garáb Schlier. The nannofloras are poor, but the first datum indicator species are found in these samples. (280—264 meters in T—4, 164—155 meters in T—9, 415—391 meters in T—3 boreholes.)

— Marine nannoplanton assemblage with a high diversity and abundance. Their embedding rock is Garáb Schlier, its more pelitic parts yield more rich, its sandy interbeddings yield poorer nannofloras. (264—6 meters in T—3, 155—11 meters in T—4, 391—15 meters in T—9 boreholes.)

All of the three borehole-profiles can be placed into the NN 4 zone whose upper boundary is defined by the extinction of *Helicopontosphaera ampliaperta*, and its lower boundary is defined by the extinction of *Sphenolithus belemnos*. In our samples there was no *S. belemnos*, so these samples are younger than zone NN 3. (We did not want to state zone boundary based on a single specimen of an uncertain *Sphenolithus sp.* conicus-belemnos group found in the 405—407 and 357—358 meter intervals of the borehole T—9.)

The presence of *Helicopontosphaera ampliaperta*, in the highest samples in all of the three profiles makes clear, that the highest part of all sections belongs to the zone NN 4; the same is supported by the coexistence of *H. ampliaperta* and *S. heteromorphus* in some of the samples. The whole section of Garáb Schlier exposed by the borings in Mátraalmás can be placed into the nannozone NN 4. The zone boundary between NN 4 and 5 was not traceable in these profiles.

3.2. *The Recsk area*

We do not want to deal with the Karpatian nannofloras of the borings Rm—103 and —109 here. These are very poor not only from point of view of diversity but also of abundance. These nannoplankton assemblages do not yield datum indicator forms at all.

3.3. *Other samples* (Table III.)

The age of a sample from an exposure of the Garáb Schlier in Nagybátony—Szorospatak—Valley, also correponds to the zone NN 4.

In the Middle—Cserhát, in the section of the gravel pit in Papucs Hill — Acsa Village, the Garáb Schlier of Karpatian age covers coarse grained sandy conglomerates (oral communication of T. Báldi). Some samples taken about the boundary of the conglomerate and schlier contain the coexistence of the species *Helicopontospharea ampliaperta* and *Sphenolithus heteromorphus*. Thus, the deposition of the Garáb Schlier had to began here in the time interval of the zone NN 4.

The stratigraphical literature has been considered the age of the Kazár Rzehakia beds conventionally as Ottnangian, because of the presence of the characteristic Rzehakia assemblage. The foraminifera faunas of the so called Rzehakia-beds in North Hungary and South Slowakia are however

Table III.

The nannoplankton from other samples

rare / some / common / abundant	Kazár								Sajóvelezd (Sv–49) 390 m	Schiller Szoros-patak	Acsa-Papucshegy	
	No. 1.	No. 2.	No. 3.	No. 4.	No. 5.	No. 6.	No. 7–13.	No. 14.			Schiller	Conglo-merate
Reticulofenestra minuta	EMPTY	.....		EMPTY	EMPTY		EMPTY	– – –	– – – –	———		
R. pseudoumbilica								.....	– – – –	– – – –	– – – –	
Coccolithus pelagicus		– – –						– – –	.....	———	– – – –	———
Cyclococcolithus floridanus .		– – –										
Cyclolithella sp.		.....										
Discolithina latelliptica		.....										
D. multipora		.....										
Helicopontosphaera ampliaperta		.....						– – –	– – – –	– – – –		– – – –
H. kamptneri		.....	– – –					.....	.....	———		– – – –
Sphenolithus heteromorphus			.....					.....	.....		.....	.....
Sph. moriformis						.....		– – –		– – – –	.....	
Discoaster adamanteus											.....	
D. variabilis											.....	.....
Cricolithus jonesi										.....		
Redeposition from Eocene ..									– – – –	———	.....	
Redeposition from Cretaceous									.....	.....	.....	.....

containing taxa, which refer rather to a Karpatian age (Kantorová, Ondrejičková, Vass in Papp et al. 1973).

The planktonic foraminifera found in the Rzehakia beds of the Salgótarján Basin (Korecz–Laky in Papp et al. 1973), furthermore the Teredos and the shark-teeth in the Kazár outcrop are indicating a not negligible connection between the brackish-water Rzehakia lagoon and the open sea with normal salinity. This connection explains the presence of stenohalyn calcareous nannofossils in the otherwise brackish-water Rzehakia beds. The concurrent occurence of *H. ampliaperta* and *S. heteromorphus* in these impoverished nannoplankton assemblages proves zone NN 4. The age of the marine Schlier, overlying the Rzehakia beds, also belongs to the zone NN 4.

In the berehole Sajóvelezd-(Sv)-42 in the Sajó–Valley (North Hungary) at a level of 390 m, the Rzehakia-bearing beds overlying the brown coal formation contain a similar nannoplankton assemblage. Its age is also NN 4, based on the coexistence of the two above mentioned species.

4. Foraminifera investigations

4.1. *The Mátraalmás area*

The most complete foraminifera faunas were found in the profile T–9. Complete faunas have been investigated, i. e. all specimens in half a kilogram of rock were selected and determined. (Denotations figured in the tables indicate the number of the specimens as follows:

○ = 1–5 specimens, × = 6–10 specimens, ⊗ = 11–20 specimens, ● = = 21–50 specimens, □ = 51–100 specimens.)

The layers covering immediatly the coal beds did not yield any foraminifera fauna, the first faunas occur only 30–50 m higher, than the coal beds. The following foraminifera fauna assemblages have been separated in the Garáb Schilier from the bottom upwards:

– *Ammonia beccarii–Florilus boueanus assemblage* (T–4 and –9 boreholes). These two species are very frequent, accompanied by some agglutinant forms *(Spiroplectammina carinata, Spirosigmoilina tenuis)*, as well as by few specimens of calcareous benthonic forms. The quantity of sponge spicules is significant, in addition few spatangides and ostracodas. The maximum thickness of the stratas yielding this kind of assemblage is 90 m in the borehole T–9. The Ammonia fauna can be correlated with the *Spirosigmoilina tenuis* assemblage in the borehole T–3, which yields *Spiroplectammina carinata, Textularia lanceolata* and *Florilus boueanus* beside the *Spirosigmoilina tenuis.*

– *Uvigerina graciliformis assemblage* is characterized by the abundant occurence of *U. graciliformis.* Also *Spiroplectammina carinata, Lenticulina inornata, Florilus boueanus* are frequent. This assemblage can be detected in the profiles T 3 and –4, the thickness of the stratas yielding such

faunas is 10 – 30 m, it occurs in the T – 9 profile too, as an interbedding in the next assemblage-type described below.

– *Agglutinated assemblage* ("agglutinated level") follows upwards immediatly the *Ammonia – Florilus assemblage* in the profile T – 9, while it follows the *Uvigerina graciliformis assemblage* in the profiles T – 3 and – 4. The mainly agglutinated-fauna-bearing beds are 190 m thick in the T – 9, 180 m thick in the T – 3, 100 m thick in the T – 4 profiles. (The upper part of the latter is supposedly eroded.) The "agglutinated level" is characterized the frequency of the *Textularia lanceolata, Cyclammina karpatica, Reticoluphragmium cf. venezuelanum, Budashevella wilsoni,* etc. The composition of the fauna is not uniform within the whole profile, there is an oscillation both in diversity and abundance. This oscillation can be attributed to ecological changes, to alterations of the intensity of water movement or to the diminishing of the amount of terrigenous material. Such "oscillation" is indicated by the great quantity of plankton in the profile T – 9 between 205 – 204 m, by the great abundance of *Valvulineria complanata* between 200 – 170 m, or by the high frequency of *Heterolepa dutemplei* and *Cibicidoies pseudoungerianus* in the profile T – 3 between 110 – 80 m.

In the profiles T – 3 and – 4 the agglutinated level can be divided into sublevels, based on frequency conditions. The lower part of the agglutinated level can be characterized by a *Textularia lanceolata assemblage* (60 – 70 m thick interval), its upper part can be characterized by a *Cyclammina karpatica assemblage* (180 30 m thick interval).

The "agglutinated level" can be correlated with the Corbula – Arca bearing intervals, further the Ophiuroidea sp. found in T – 3 borehole belongs to this level to.

– A *Globigerina assemblage* occurs in the profiles T – 3 and – 9, with a high frequency of planktonic forms, i. e. *Globigerina praebulloides praebulloides, Gg. ciperoensis ottnangensis. Globigerinoides sicanus* (= G. bisphaericus) however is lacking. In the T – 9 profile a rich *Uvigerina-* and *Bolivina-fauna* was observed within the Globigerina-level, with the great abundance of *Uvigerina graciliformis, U. bononiensis primiformis, Bolivina plicatella, B. plicatella mera, B. scalprata miocenica* and *B. pokornyi pokornyi.* This assemblage represents the deepest water environment.

(The arrangement of assemblages in the profiles and their related position can be seen on Fig. 2.)

4.2. *The Recsk area*

The Garáb Schlier detected in the Recsk area can be characterized by an *Ammonia beccarii – Florilus boueanus assemblage.* The agglutinated forms occur only in single intervals, mainly with frequent *Reticulophragmium* species *(R. venezuelanum, R. carpaticum).*

The malacological investigations of T. B á l d i (1970, 1971) support our statement: these foraminifera faunas do not represent a typical schlier

Table V.

The foraminifera-fauna in the profile of the borehole T – 3.

	6 m	25 m	44 m	85 m	102 m	116 m	135 m	154 m	162 m	177 m	188 m	994 m	203 m	215 m	222 m	232 m	243 m	253 m
Rhabdammina sp.						○								○				
Bathysiphon filiformis					○	○	⊗			○				○				
Ammodiscus miocenicus					○													
Reophax pilulifera							⊗											
Haplophragmoides vasiceki vasiceki															○			
Cribrostomoides columbiensis moravica		○	○															
Cyclamina karpatica	○	○	●		⊗		●		○	○	○			○	○			
C. sp.													○			○		
Alveolophragmium crassum							×								○			
Reticulophragmium carpaticum			●		×		⊗		○									
R. cf. venezuelanum	○	○	●		×			○	○	○	○			○			○	
Spiroplectammina carinata	○	○		○	×		⊗			○					⊗		○	
S. pectinata		○			○												○	
Textularia lanceolata			×		○		×	●	●	●	●	○	○	○				
T. gramen abbreviata	○				○													
Budashevella wilsoni	○				○		×											
Martinottiella communis	○				○													
Spiroloculina tenuissima	×			○	×	○	○											
Sigmoilopsis celata	⊗	×			×												●	○
Spirosigmoilina tenuis					○													
Lagena isabella					○	○												
L. striata							○											
Lenticulina cultrata	●	○				○	×		⊗		○	○						
L. inornata							○											
Marginulina glabra							○											
M. hirsuta					○		○											
Plectofrondicularia digitalis						○	○											
P. inaequalis							○											
P. sp.					○													
Amphimorphina hauerina	○																	
Globulina gibba				○			○											
G. inaequalis							○											

The foraminifera-fauna in the profile of the borehole T – 9.

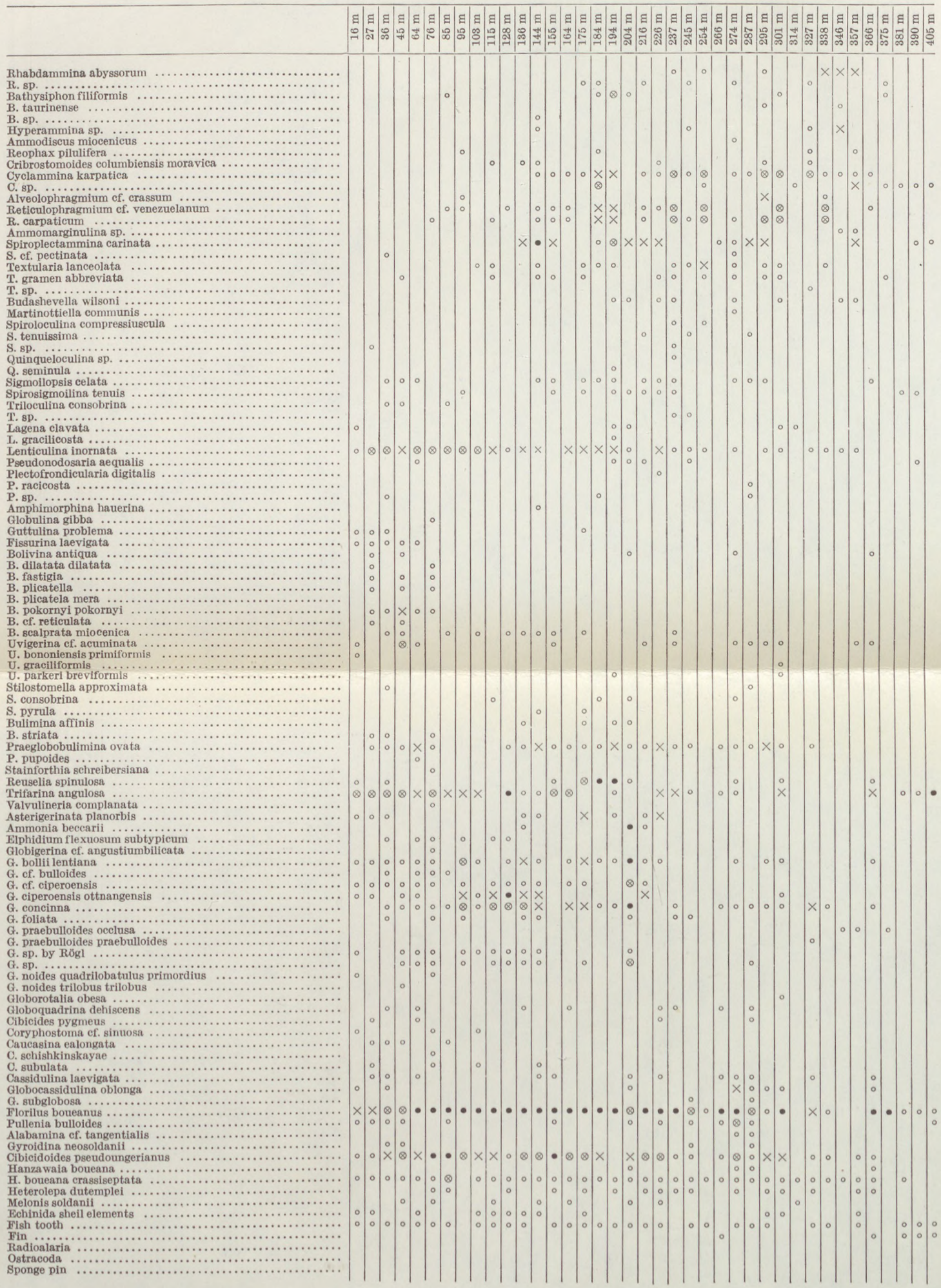

Number of specimens between
1 – 5 ○
6 – 10 ×
11 – 20 ⊗
21 – 50 ●
50 – 100 □

Table V.

	6 m	25 m	44 m	85 m	102 m	116 m	135 m	154 m	162 m	177 m	188 m	994 m	203 m	215 m	222 m	232 m	243 m	253 m
Guttulina problema							○											
Bolivina hebes	○																	
B. scalprata miocenica				○	○													
B. sp.						○												
Uvigerina cf. acuminata					○	○												
U. bononiensis primiformis	○	○		○														
U. graciliformis	○	⊗		○	×			○		⊗	○			○	□			
Stilostomella elegans					○		○											
Bulimina striata			○		○	○												
Stainforthia schreibersiana	×	⊗		○	○	○												
Valvulineria complanata							×										○	
Ammonia beccarii			○					○	○					○	○			○
Elphidium flexuosum subtypicum		○																
Globigerina bollii lentiana	⊗	⊗				○												
G. ciperoensis ottnengensis	●	●		○	○		○							○				
G. obesa	●	●			○													
G. praebulloides occlusa	⊗	×								○								
G. praebulloides praebulloides	⊗	●		○	○													
G. cf. scalena		○																
G. sp.										○		○						
Globigerinoides trilobus trilobus		○																
Globorotalia foliata	⊗	×																
Planulina wuellerstorfi					○													
Cibicides lobatulus ornatus						○							○					
Caucasina elongata	○	×		⊗														
C. subulata				×	○													
Cassidulina laevigata					○								○					
Globocassidulina oblonga				○														
Florilus boueanus	□	□	⊗	●	●	○	○	○	×	×	○	○	○		×	○	○	
Pullenia bulloides			○	○	○	○	×											
Gyroidina soldanii				○	×	○	○											
Cibicidoides ungerianus				○														
Cibicidoides pseudoungerianus	○	○	○	⊗	●		○											
Hanzawaia boueana				○	○			○										
H. boueana crassiseptata									○									○
Heterolepa dutemplei	●	⊗	⊗	□	□	○	⊗			○		○	○		×			
Melonis soldanii							○			○								
Spatangida	○	○	○	○	○	○	○	○	○	○	○	○	○	○	○		○	
Ostracoda	○	○					○		○	○	○	○	○	○	○		○	
Fin					○	○												
Echinida shell elements			○		○	○	○	○										
Sponge pin	○			○	○									○			○	○
Fish tooth							○											

Table VI.

The foraminifera-fauna in the profile of the borehole T — 4.

	11 m	21 m	33 m	44 m	56 m	66 m	75 m	85 m	95 m	107 m	115 m	126 m	134 m	144 m	154 m
Bathysiphon filiformis		○	○			○				○					
Hyperammina sp.		○													
Reophax pilulifera							○								
Cribrostomoides columbiensis moravica		×													○
Cyclammina karpatica	○	⊗	⊗	○	○	○		○		○	○	○			
C. div. sp.													○		
Alveolophragnium cf. crassum		×									○				
Reticulophragmium carpaticum	○	○	×												
R. cf. venezuelanum	○		○				○	○		○	○				
Ammomarginulina sp.		○													
Spiroplectammina carinata											○			○	
S. pectinata											○				
Textularia lanceolata	○	×	⊗		⊗	○	⊗	×	⊗	×		○			
Budashevella wilsoni		○	×												
Sigmoilopsis celata										○					
Spirosigmoilina tenuis													○	○	
Lenticulina inornata	○	×	○	○	○	●		○	○	○	×				
Marginulina hirsuta			○						○						
Pseudonodosaria aequalis		○													
Plectofrondicularia digitalis			○												
Bolivina scalprata miocenica		○	○												
Uvigerina graciliformis		○								⊗	□			○	
Siphogenerina sp.			○												
Stilostomella approximata		○													
S. elegans		○													○
Bulimina striata			○												
Stainforthia schreibersiana	○	○													
Ammonia beccarii							○			×		○		●	●
Globigerina ciperoensis ottnangensis					○					○					
G. sp.	○		○												
Globigerinoides trilobus trilobus												○			
Eponides umbonatus											○				
Caucasina elongata				○											
Florilus boueanus	○	⊗	○	⊗	×	×				○	⊗	○	●	⊗	
Pullenia bulloides		○	○												
Gyroidina soldanii	○	○													
Heterolepa dutemplei	○	⊗	×			○			⊗	×	⊗				○
Melonis soldanii	○		○												
Spatangida	○	○	○	○	○	○		○	○	○	○		○		○
Ostracoda			○	○	○	○	○	○	○	○	○	○	○		○
Fin	○	○	○												
Echinida shell elements	○	○	○	○		○									○
Fish tooth						○									○
Sponge pin														○	○

fauna. They indicate a relatively constant facies. No series of assemblages representing even deeper and deeper facies can be detected here, as it was observed the borehole profiles of Mátraalmás.

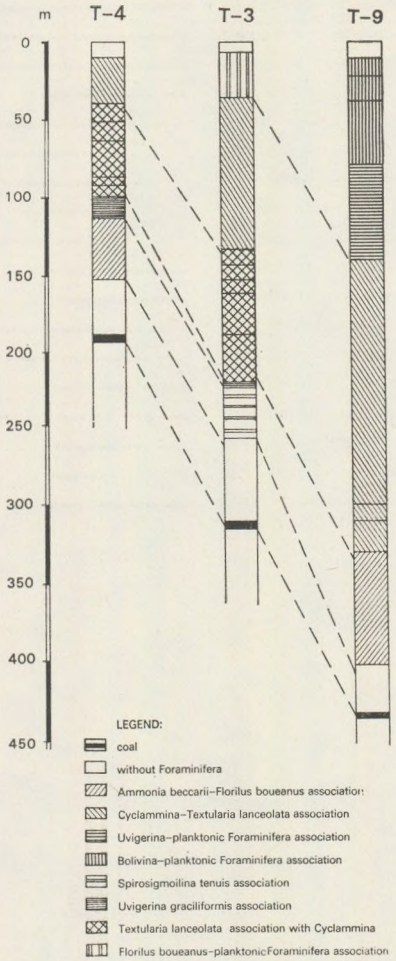

Fig. 2. The position of the foraminiferal assemblages in the Mátraalmás boreholes

4.3. *Ecological characteristics*

The microfauna of the Garáb Schlier in the Mátraalmás area proves the gradual transgression. The shallow-water, littoral *Ammonia – Florilus fauna* turns into *Uvigerina assemblage* upwards. The optimal biotop of the recent Uvigerinas is 100 meters below the sea-level. In our case the presence

Table VII.

The regional stages of the Central Paratethys in correlation with the planktonic foraminifera zones, nannoplankton zones, showing the vertical distribution of the most important foraminifera and nannofossil datum indicatores occuring in the examined profiles

Regional stages of Miocene in the Middle Paratethys	CPN plankton zones	Denomination of the CPN plankton zones	Nannonzones	Denomination of the nannozones
Badenian M_4 (Tortonian)			NN-5	Sphenolithus heteromorphus
Karpatian M_3 („Upper-Helvetian")	5	Globigerinoides bisphericus	NN-4	Helicosphaera ampliaperta
			NN-3	Sphenolithus belemnos
Ottnangian M_2 („Lower Helvetian")	4	Globigerinoides trilobus	NN-2	D. druggi
Eggenburgian M_1 („Burdigalian")	3	G.obigerinoides quadrilobatulus primordius	NN-1	Triquetrorhabdulus carinatus
			NP-25	S. ciperoensis
Egerian OM („Aquitanian, Chatt-Aquitanian Chattian")	2	Globorotalia opima opima — Globigerinoides (ent.)	NP-24	Sphenolithus distentus

of such water depth can not be supposed owing to the monotonous character of the fauna. The *Reticulophragmiums* being frequent in agglutinated faunas indicate a sandy, soft sea bottom in shallow-sublitoral, sublitoral facies, while *Cyclammina karpatica* indicates deeper, neritic biotop. The presence of agglutinated faunas correlated with the malacological investigations proves probably a water-depth about 50 – 60 meters.

The greatest water-depth is indicated by the *Globigerina assemblage*, where *Uvigerinas* and *Bolivinas* proves a 100 m deep sea water with normal salinity.

The foraminifera assemblages of the Recsk area show the stabilized shallow-sublitoral environment. Only the faunas of the profile Sirok – 1 indicate the transgressive and regressive moments of the formation of the Garáb Schlier, though the water-depth could not surpass the 50 m even at the times of maximum transgression.

4.4. *Stratigraphic position of the foraminifera fauna*

The foraminifera faunas of both area investigated are indicating a Karpatian age. There are some species, whose time range is restricted to the Karpatian stage (e. g. *Cyclammina karpatica, Textularia lanceolata):* a lot of species appear in the Ottnangian and reach their maximum frequency in the Karpatian (e. g. *Uvigerina graciliformis):* further those species were also found, which appear in the Karpatian and became characteristic in the agglutinated assemblages of the Karpatian and Badenian *(Cyclammina karpatica, Reticulofenestra carpaticum, R. venezuelanum).*

The time range of the *Globigerina ciperoensis ottnangensis* R ö g l et al. (1975) being frequent in the plankton fauna described here, lasts from the Upper Egerian up to the Middle Karpatian. The *Globigerina praebulloides praebulloides* is one of the Tertiary taxas having the longest time range. The species *Globigerinoides sicanus* was not found in the faunas described above. This taxon appears in the Middle Karpatian and occurs in the Lower Lagenidae Zone too. Its absence can be explained by the erosion of the upper section of the Schlier, or by the biotop of Recsk area, yielding no trace of sea currents.

5. Summary

5.1. We can state, that the Rzehakia (Oncophora) beds and the greatest part of the covering Garáb Schlier belong to the nannozone NN 4.

Though we can not exclude the possibility of the occurence of *Sphenolithus belemnos* in the Central Paraterhys, this species has not been found so far. Therefore in our region it is not suitable to indicate datum level. We join to the opinion of BUKRY (1973), who proposed the redefinition of the upper limit of the *Sphenolithus belemnos zone* by the first appearence of *Sphenolithus heteromorphus*, which coincides approximately with the extinction datum of *Sphenolithus belemnos.*

Sphenolithus heteromorphus occurred in the Hungarian Miocene as early as in zone NN 4.

5.2. The study of the foraminifera fauna of the Garáb Schlier gave the first information about the presence of the "agglutinated level" in addition to the Uvigerina-faunas being known earlier already. Such Uvigerina assemblages were described from the Vienne Basin by Cicha et al. (1967) (Závod — Laksar strata, Laksarská Nova Ves — 1, — 2 boreholes). Also the same authors have mentioned Uvigerina- and Globigerina assemblages from Dolna Pribelce and Ďurkovce (South Slovakia), which area represents the northern continuation of the Hungarian Schlier-series.

5.3. Based on the recently investigated profiles and on the earlier datas of the geological literature we can state, that the brown coal covering brackish-water and marine Karpatian layers of the East (Sajó — Valley and Egercsehi) are substituted in the West (Sirok, Recsk) by a less sandy, pelitic shallow-sublitoral Schlier. The Karpatian Schlier of the borehole Rm — 103 (according to T. Báldi 1975) has deposited in a water with maximum 30 — 40 m water depth. This gives an explanation to the great frequency of the Ammonia-Florilus assemblages and to the low abundance and diversity of the nannoflora.

The Karpatian schlier of Mátraalmás could be deposited in a deeper, more pelagic part of the Karpatian sedimentary basin, than that of the Recsk area — altough it is not represented in the rock-quality, only in the fauna- and flora assemblages.

REFERENCES

Alföldi L. et al., 1975: Miskolc. Explanatory to the geological map series of 1 : 200 000, pp. 1 — 277 (in H-ngarian)

Báldi T., Horváth M., 1970: Report on the study of fauna of the borehole Sirok-1. (Manuscript in Hungarian)

Báldi T., Horváth M., 1971: Preliminary summarizing report on the stratigraphic investigations Recsk. (Manuscript, in Hungarian)

Báldi T., Horváth M., 1975: Report on the macro- and microfauna of the Rm — 103. borehole. (Manuscript, in Hungarian)

Báldi T., Horváth M., Nagymarosy A., 1976: Report on the paleontological study of the boreholes Rm — 109. and Rm — 116. (Manuscript, in Hungarian)

Báldi T., Horváth M., Nagymarosy A., 1977: Report on the general biostratigraphical study of the brown coal field at Mátraalmás. (Manuscript, in Hungarian)

Báldi, Beke M., 1960: The stratigraphic importance of Hungarian Miocene Coccolithophoridas. Föld. Közl., 90., pp. 213 — 223 (in Hungarian)

Balogh K. et. al. Salgótarján. Explanatory to the geological map series of 1 : 200 000, pp. 1 — 155, (in Hungarian)

Bartkó L., 1961 — 62: Geological study of the brown coal area of Nógrád. Candidate's thesis. Manuscript (in Hungarian)

Bukry, D., 1973: Low-latitude Coccolith biostratigraphic zonation. Repr. Edgar et Saunders: Rep. DSDP, vol. XV. Washington, pp. 685 — 703.

Cicha, I., Seneš, J., Tejkal, I., 1963: Chronstratigraphie und Neostratotypen, M_2 — Karpatien, Bratislava.

Cicha, I., Zapletalova, I., 1963: Wichtige Vertreter der Familie Lituolidae Reuss, 1861 (Foraminifera) aus dem Miozän der Westkarpathen. Sborn. Geol. ved, paleont. sv. 1. 75 — 121.

Cicha, I., Zapletalova, I., 1966: Representatives of Bolivina in the Miocene of the Western Carpathians. III-rd Sec. CMNS. pp 103 – 109.
Cicha, I., Zapletalova: I., 1966: Die Familie Textulariidae des Miozäns der Westkarpaten, III-rd. Sec. CMNS, pp. 194 – 196.
Csepreghy, Meznerics, I., 1951: Fauna of the Schlier and pectinate sandstone of the surroundings of Salgótarján. Föld. Közl., 81, pp. 303 – 319.
Csepreghy Meznerics I., 1954: The Tortonian and Helvetian fauna of the Eastern-Cserhát Ann. Hung. Geol. Inst., 41, 4, pp. 1 – 185. (In Hungarian)
Csepreghy Meznerics, I., 1960: Pectinidés du Néogene de la Hongrie et leur importance stratigraphique. Mem. Soc. Geol. France, Tom, 39, Mém. 92, pp. 1 – 56.
Horusitzky F., 1939: Upper Oligocene and Lower Miocene faunas from the Ipoly basin. Annual Report of MÁFI from 1933 – 35, 2, pp. 782 – 788 (in Hungarian).
Martini, E., Müller, C., 1975/b: Calcareous nannoplankton from the Karpatian in Austria (Middle Miocene). Proc. VI – th Congr. RCMNS, Bratislava.
Martini, E., Worsley, T., 1970: Standard Neogene Calcareous Nannoplankton Zonation. Nature, V. 225, num. 5229, pp. 285 – 290.
Martini, E., Müller, C., 1975/a: Calcareous Nannoplankton and Silicoflagellates from the type Ottnangian and equivalent strata in Austria (Lower Miocene). Proc. VI-th Cong. RCMNS, Bratislava.
Mayne, W., 1955: Reticulophragium n. gen., a new name for Alveolophragium Stschedrina, 1936. Journ. paleont., V. 29. pt. 3, pp. 557 – 558.
Noszky, J. Sen., 1930: Oligocene – Miocene strata of the northeastern part of the Hungarian Middle Mountains. II. Miocene. Ann. Hist. Nat, Mus. Nat. Hung., 27, pp. 159 – 236.
Papp, A. et. al., 1973: Ottnangien Chronostratigraphie und Neostratotypen. Bd. III. pp. 1 – 841. Bratislava.
Rögl, F., 1968: Die miozäne Foraminiferenfauna von Laa an der Thaya in der Molassenzone von Niederösterreich. Geol. Ges. 61. S. 63 – 123.
Rögl, F., 1969: Die Foraminiferenfauna aus Phosphoritsanden von Plesching bei Lins (Oberösterreich) – Ottnangien (Untermiozän). Natur. Jahrb. Stadt Sonderb.
Rögl, F., 1975: Die planktonischen Foraminiferen der Zentralen Paratethys. Proc. VI-th Congr., RCMNS, Opp. 113 – 120. Bratislava.
Rögl, F., Steininger, F., Martini, E., 1975: Current Oligocene/Miocene biostratigraphic concept of the Central Paratethys. Newsletters Stratigr., pp. 1 – 48.
Schréter, Z., 1940: Surroundings of Nagybátony, Works of the Hung. Geological Society, 2, pp. 1 – 154.

ACID LEACHING OF SPHALERITE CONCENTRATE

A. ABDEL REHIM

Alexandria University, Cairo /Department of Mineralogy, Eötvös University, Budapest

Received: 6 October 1974

ABSTRACT

The acid leaching of sphalerite with sulphuric acid has been investigated. It was found that the leaching efficiency of zinc increased with temperature and, acid concentration and attains a maximum of 93.6% at 200 °C using dilute acid. This method avoids zinc ferrite and silicate formation provides accomplishment of the process in a single stage, and is economic.

РЕЗЮМЕ

В работе проводилось исследование кислотной обработки сфалерита с помощью серной кислоты. Было найдено, что способность цинка к щелочению увеличивается с повышением температуры и концентрации кислоты и достигает максимума при 93.6% концентрации и при температуре в 200°C. Этот метод не влияет на цинковый феррит и на образование силикатов, а осуществление процесса просто и экономично.

Introduction

Sphalerite is present in economic amounts in many localities of the Eastern Desert of Egypt. Here, zinc deposits include polymetallic sulphide deposits (zinc and copper sulphides, and, to a lesser extent, lead and iron) and lead-zinc mineralization (composed mainly of galena and sphalerite with some pyrite). Oxidation and alteration products of the sulphides include smithsonite, cerussite, hemimorphite, zinc sulphate and limonitic and hematitic ochres. Studies on extraction processes of zinc received little attention (Amin 1955; Barakat – El-Shazly 1956; El-Shazly 1957; El-Shazly – Afia 1958; Hume 1934; Said 1962).

Technological processing methods of sphalerite for extraction of zinc from it includes the following stages: roasting of the concentrate, leaching of the roasted mass with sulphuric acid and then electrolysis. The main disadvantages of roasting of sphalerite concentrate are the formation of zinc ferrite, especially when the concentrate contains high amount of iron, and also the formation of some silicates. The zinc ferrite is insoluble during acid leaching and causes considerable loss of zinc. As a result of silicate formation, the obtained solutions contain considerable amount of silicic acid, which greatly influences their settling and filteration. Also, these

methods include two stages, roasting of the ore and acidic leaching, which is uneconomic in industry (Forward – Veltman 1959; Plaksin 1963; Ralston 1941; Yaroslavtsev – Smirnov 1964).

The direct acid leaching of sphalerite concentrate with sulphuric acid is more suitable. This process is carried out in various ways under oxidizing conditions at atmospheric pressure or in autoclaves (Bjorling 1954; Ellis 1959; Forward 1953; Forward Veltman 1959; Forward – Halpern 1956/57) Forward – Mackiw 1955; Plaksin 1963; Ralston 1941, Snurmikov et. al. 1969; Tronev – Baudin 1939; Yaroslavtsev – Smirnov 1964).

The present work represents a study of a single stage leaching of sphalerite concentrate with sulphuric acid of different concentrations in air current at different temperatures.

Experimental work:

This research was carried out with sphalerite concentrate, having mineralogical and chemical composition as given in Tables I and II respectively.

Table I.

Mineralogical composition of zinc concentrate

Mineral	Content %
Sphalerite	71.6
Galena	6.4
Pyrite	8.3
Chalcopyrite	2.2
Hematite	2.4
Others (carbonates, silicates,)	9.1

Table II.

Chemical composition of zinc concentrate

Chemical component	Percentage, %
Zn	47.64
Pb	5.80
Fe	8.52
Cu	0.81
S	30.45
Al_2O_3	1.12
CaO	1.40
SiO_2	2.83

From table I. the sphalerite content in the concentrate is 71.6%, while the other subordinate minerals are galena, pyrite, chalcopyrite, quartz and some carbonates and other minerals. These mineral impurities are genetically connected with the formation of sphalerite.

Techniques of work:

The initial sphalerite concentrate used is of grain size 98% − 200 mesh. The weight of the concentrate ranges from 5 − 10 gm. The sphalerite was mixed with sulphuric acid of particular amount and concentration and heated in electric furnace to a fixed temperature in dried air current.

The temperature was regulated automatically with accuracy ±3 °C. Leaching experiments were carried out at different temperatures and times. Dissolution of the sulphate mass with water was carried out in a beaker with magnetic stirrer at room temperature. The solution was filtered under vacuum and the obtained cake was washed with water. Filterate and washed water were combined together and analysed for the total zinc content & then the leaching efficiency of zinc was calculated.

Results and Discussion

A series of experiments were carried out to study the essential factors acting upon leaching of sphalerite (amount and concentration of sulphuric acid, tepperature and time) and to determine its optimum conditions of acid leaching.

1 – *Effect of acid concentration:*

Experiments were carried out at amount of sulphuric acid 120% of theoretical amount for dissolution of concentrate and oxidation of hydrogen sulphide, at temperatures 125° − 200 °C, duration of one hour and at different concentrations of acid.

As shown in Fig. 1, at 125° and 150 °C, leaching of sphalerite is rapidly increased, as the acid concentration increases. Maximum leaching of sphalerite (91.5%) at 150 °C reaches only using concentrated acid, while at 125 °C complete leaching of sphalerite does not take place.

At 200 °C, sharp increase of leaching is observed at low acid concentrations, then there is a gradual increase. In general, as the acid concentration and temperature increase, dissolution of sphalerite increases.

The suitable acid concentration was selected, taking into consideration the possibility of using the return zinc electrolyte solution is the leaching process. This may be considered as 20%, the nearest one to free acid content in the return zinc electrolyte and at which nearly complete leaching of sphalerite (~93.6%) is reached at 200 °C.

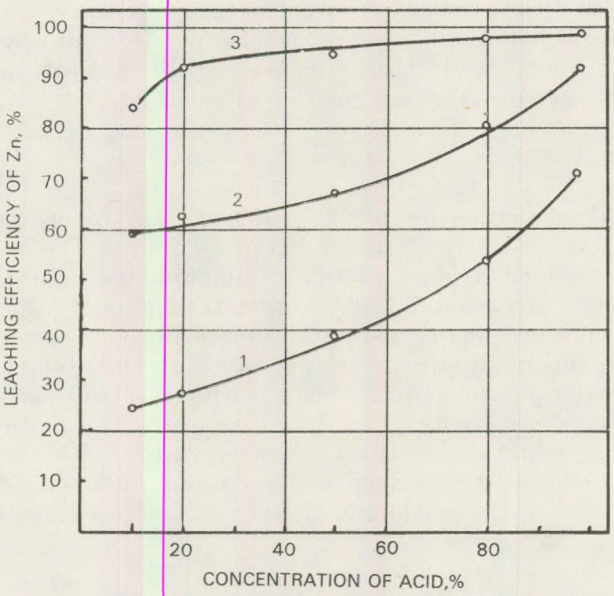

Fig. 1. Relation between the leaching efficiency of sphalerite and concentration of sulphuric acid at different temperatures. 1, 2, & 3 – at 125, 150 & 200 °C respectively.

2 – *Effect of acid amount:*

It is necessary to carry out leaching of sphalerite with some excess of sulphuric acid, as lead sulphide reacts more rapidly than zinc sulphide (Forward – Veltman 1959). Experiments were carried out using different amounts of sulphuric acid, ranging from 100 to 150% of theoretical value and at different acid concentrations and temperatures.

From the obtained results (Fig. 2) it is observed that the conversion of zinc sulphide to zinc sulphate is sharply increased, as the amount of acid increased from 100 to 120%, then it is slightly increased especially at higher temperature. The leaching efficiency of sphalerite is low at temperatures 125–150 °C, even at acid expense 150% of theoretical amount. This may be due to the low velocity of sulphatization at low temperature. On the other hand, at 200 °C, high leaching efficiency of sphalerite was obtained at acid amount 120% which can be considered as suitable amount for leaching. Thus, the extent of dissolution of sphalerite is directly proportional to the amount of sulphuric acid added.

3 – *Effect of temperature and time:*

To study the action of both temperature and time on leaching of sphalerite, experiments were carried out a fixed amount of acid 120% of theoretical amount and its concentration 20,50% of concentrated acid and at different temperatures 125–300 °C, and time from 5 to 75 min.

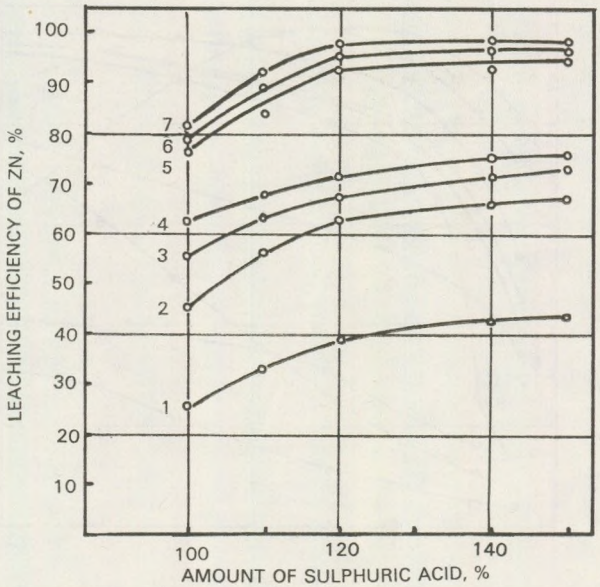

Fig. 2. Relation between leaching efficiency of sphalerite & amount of sulphuric acid at different concentrations & temperatures.
1,3,6 – 50% sulphuric acid at 125,150 & 200 °C
2,5 – 20% sulphuric,acid at 150 & 200 °C
4,7 – concentrated acid at 125 & 200 °C

From the obtained results (Fig. 3), the following conclusions have been drawn:

a) In general, as the temperature increases, the dissolution of sphalerite increases with time, except at 250 – 300 °C, where it decreases after a particular time of leaching.

b) At 125 °C it was found that the conversion of sphalerite to zinc sulphate though rapid initially in the first half hour, after that is slowly increased. At this temperature, complete leaching of sphalerite does not take place even at long time.

c) At 150 °C, sharp increase in dissolution of sphalerite with time was observed, and the higher the acid concentration, the greager would be the leaching efficiency. At this temperature, nearly complete leaching of sphalerite was reached using concentrated sulphuric acid.

d) At 200 °C, leaching efficiency of sphalerite is though very sharp during the first half hour for all acid concentrations, but after that it is gradual. At this temperature, complete leaching of sphalerite (98.7%) was reached during one hour using concentrated acid.

e) At 250 – 300 °C, high conversion of sphalerite to zinc sulphate was observed during the first twenty min. and complete leaching was reached after 30 – 20 min. respectively. At these temperatures, after reaching maximum and after particular time, the leaching efficiency of-

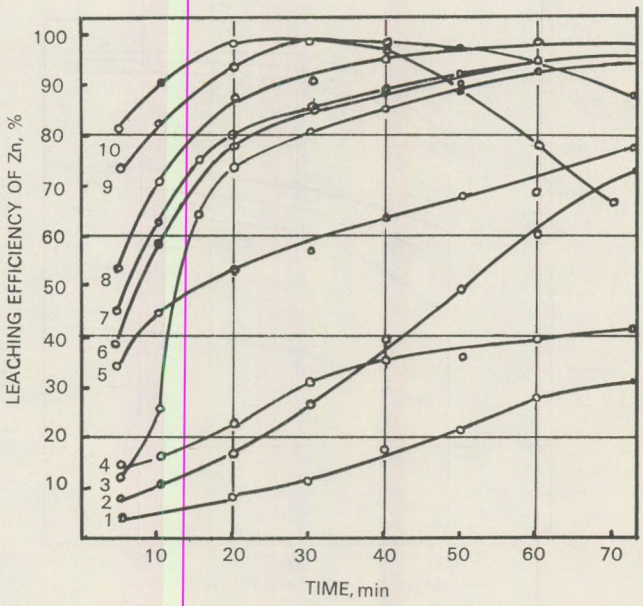

Fig. 3. Relation between leaching efficiency of sphalerite & time at different temperatures.
1,2 & 3 – 20% sulphuric acid, at 125,150 & 200 °C
4,5 & 6 – 50% sulphuric acid, at 125,150 & 200 °C
7,8,9 & 10 – concentrated acid at 150, 200, 250 and 300 °C respectively.

sphalerite decreases with time at different rates, depending upon the temperature of leaching. The higher the temperature, the more decrease of leaching efficiency of zinc will be observed. This decrease may be due to to not only the evaporation of water from reaction pulp, but also due to the increase of volatilization of sulphuric acid.

Conclusions

1 – The possibility of acid leaching of sphalerite with sulphuric acid has been studied, from which it was found that as the acid concentration and temperature increase, the leaching efficiency of sphalerite increases with time. At high temperatures, after reaching complete dissolution and after a particular time of leaching, it decreases at different rates, depending upon the temperature.

2 – Sphalerite can be leached by dilute sulphuric acid solutions of amount 120% of theoretical value, at 200 °C and time 1 hour. At these conditions, nearly complete leaching of sphalerite (93.6%) was reached.

3 – The main advantages of the direct acid leaching of sphalerite are the following:

a – Avoiding of zinc loss due to zinc ferrite formation during roasting of sphalerite concentrate. Also, avoiding of the formation of some silicates and consequent difficulty of settling and filteration of the obtained solutions.

b – Accomplishment of the process in a single stage.

c – High extraction of zinc regardless of the iron content of the concentrate.

d – The process is simple and economic.

REFERENCES

Amin, M. S., 1955: Geological features of some mineral deposits in Egypt. Bull. Inst. Desert Egypt, 5(1), pp. 209 – 239.

Barakat, N., El-Shazly, E. M., 1956: Spectrographic determination of chemical elements in Egyptian minerals from lead, zinc, copper and gold deposits. Bull. Inst. Egypt, 37, pp. 21 – 46.

Bjorling, N. 1954: Leaching of sulphide mineals under pressure. Erzmetall, V. 8, pp. 781 – 784.

Dobrokhotov, G. N., Onutshkina, N. E., 1964: Kinetics of autoclave leaching of sphalerite. IUVZ. Nonferrous Metallurgy, N. 5, pp. 51 – 57.

Ellis, A. J., 1959: Econ. Geol. V. 54, N. 6, pp. 1035.

El-Shazly, E. M., 1957: Classification of Egyptian mineral deposits. Egypt. J. Geol., 1, pp. 1 – 20.

El-Shazly, E. M., Afia, M. S., 1958: Geology of Samiuki deposit, Eastern Desert. Egypt. J. Geol., 2, pp. 25 – 42.

Forward, F. A., 1953: Canadian Mining and Metall. Bull., V. 46, N. 499.

Forward, F. A., Voltman, H., 1959: Direct leaching of zinc sulphide concentrates by Sherrit Gordon plant. Journal of Metals, V. 11, N. 12, pp. 836 – 840.

Forward, F. A. Halpern, J., 1956 – 57: Hydrometallurgical process at high pressure. Trans. Inst. Mining and Metallurgy, V. 66, N. 5.

Forward, F. A. Mackiw, V. K., 1955: Journal of Metals, V. 7., N. 3, pp. 457.

Hume, W. H. 1934: Geology of Egypt. V. II, Part III. Minerals of economic value. Geol. Survey of Egypt.

Plaksin, I. N., 1963: Complex processing of lead-zinc ores. Izdatelstva AN SSSR

Ralston, O. C., 1941: Electrolytic deposition and hydrometallurgy of zinc. Mc Graw – Hill, New York.

Said, R., 1962: Geology of Egypt. Elsevier Publ. Comp. INC, New York.

Snurnikov, A. P., Larin, V. F., Krilov, E. I., 1969: Study of mechanism and kinetics of reaction of nonferrous metal sulphides with sulphuric acid. IUVZ. Nonferrous Metal., N. 5, pp. 26 – 31.

Tronev, V. G., Baudin, S. M., 1939: Oxidation of zinc sulphide and transferenc of zinc into aquaeous or alkali solutions at air pressurec. Comptes Rendus de l'Academie des Sciences de l' URSS, V. 39, N. 6. pp. 541 – 543.

Yaroslavtsev, A. S., Smirnov, V. E., 1964: Research on autoclave leaching of zinc concentrate. Nonferrous Metals, N. 2, pp. 26 – 30.

Yaroslavtsev, A. S., Smirnov, V. E. 1964: Distribution of metals and sulphur in autoclave leaching of zinc concentrate. IUVZ. Nonferr. Metal. N. 5, pp. 58 – 62.

THE FORMATION OF CINNABAR-METACINNABAR AT HIDROTHERMAL CONDITIONS (BETWEEN 25° – 300°C TEMPERATURE) AND ITS GENETICAL INTERPRETATION

J. KISS

Department of Mineralogy, Eötvös University, Budapest

and

A. ABDEL REHIM

Alexandria University

Received: 15 October 1976

Summary

Observations on natural mercury mineralizations provide controversial data about the formation $\alpha - \beta$ mercury sulfides (cinnabar-metacinnabar) as both modifications can exist in same genetical type of mineralization, which is characterised by enantiotropic temperature range. Both cubic (metacinnabar) and trigonal (cinnabar) have been recorded as first precipitations.

During the laboratory experiments sustems $HgCl_2 - H_2S - H_2O$ and $HgNO_3 - H_2S - H_2O$ have been studied in temperature range between 25° – 100 °C. Structural and morphological deformations of cubic modification formed on 25 °C have been investigated in temperatures between 50° – 300 °C.

The role of As, Sb, Tl trace elements in the formation of cinnabar-metacinnabar have also been studied.

These chemical, crystal-chemical investigations provide additional data to the genetic interprtation of mercury deposits.

Introduction

Mercury deposits have generally simple mineralogical compcsition, mainly consisting of $HgS - Hg - Sb_2S_3$ and few other associated elements. The deposits are characterised by the dominance od *S*, *Ca*, *Si* (*Fe*, *Mg*) and *O* elements, *As*, *Sb* and *Cu* chalcophile elements, occasional concentrations of *Au*, *Ag*, *Bi*, *Pb*, *Zn*.

The average concentration of mercury in the Earth's crust is 0, 0X ppm:

Vinogradov	(1949, 1963)	= 0,07 – 0,083 ppm
Taylor	(1964)	= 0,08 ppm

The concentration is not affected by the acidity of igneous rocks (Turekian – Wedepohl, 1961, Vinogradov, 1962 third column: Ehmann – Lovering 1967):

ultrabasites	= 0,01 – 0,0X	ppm (4 ppb)
basic	= 0,09	ppm (7 ppb)
intermediate (syenite)	= 0,0X	ppm (4 ppb)
acid (granite)	= 0,08	ppm (39 ppb)

During the late crystalization phases, the amount of Hg in pegmatites less than 0,0X ppm, increasing in kata-and mesothermalites and reaches its peak at epithermal conditions. Volcanic exhalations generally have significant mercury content.

The *Hg* concentrations is sedimentary environment:

a) shales	0,40 ppm
b) sandstones	0,03 ppm
c) carobnates	0,04 – 0,0X ppm
d) pelites	0,X ppm

Usually high *Hg* concentration is recorded in the air above mercur deposits. This fact isused as exploration tool. Organisms (algae, fishes) show few tenth of γ/kg *Hg* content.

The most important minerals of mercury are the $\alpha - \beta - \gamma - HgS$, cinnabar and metacinnabar and the native mercury. Schwazite (HgS np to 24 per cent Hg), livingstonite ($(HgSb_4S_8)$, montroydite (HgO), guadalcazzarite (HgZn) (S, Se), onophrite Hg(S, Se), coloradcite (HgTe), tiemannite (HgSe), kleinite $Hg_2N(Cl, SO_4) \cdot nH_2O$, mosesite $(Hg_2NCl \cdot H_2O$, terlinguaite $(2HgO \cdot Hg_2Cl_2)$, eglestonite (Hg_6Cl_4O) are rare accessories in mercury deposits. The oxide-chlorides are possible products of the vapor phase.

There are several opinions about the formation of cinnabar-metacinnabar:

- metacinnabar crystallises prior to cinnabar (αHgS)
- metacinnabar and cinnabar are crystallising syngenetically
- formation of metacinnabar follows that of αHgS
- metacinnabar precipitates from solutions and is not an alteration product of cinnabar
- metacinnabar has supergene origin.

In hot brines of Amadee Hot Spring, California, and Bouiking Spring, Idaho, metacinnabar (βHgS) crystallises, subsequent to cinnabar. There are examples for reversed precipitation sequences too. The formation of metacinnabar is probably affected by temperature, and probably, the pH conditions and the chemical assemblage, however the effects of there latter facter has not been experimentally proved yet. Near the month of Amadee Hot Spring precipitations, of cinnabar, metacinnabar, in onter zones drops of native mercury has been observed from the alkaline hot brines. From hot brines at Sulphur Bank California, similar phenomena have been recorded.

At Bouiling Spring (Valley County, Idaho) crystallisation of *Mn*-rich metacinnabar have been described, at 7 – 8 m distance from the mouth of the Spring. Cinnabar has formed near the mouth, associated with calomel, Hg-oxide-chloride, chalcedony, quartz, montmorillonite, alunite.

K r a u s k o p f (1951) has suggested a temperature range 80° – 250 °C at 30 at pressure for the formation of cinnabar. D i c k s o n (1964) has given 100 – 230 °C temperature at 30 at pressure. The solubility of HgS in Na_2S solution had first studued by K n o x (1906), then D i c k s o n (1964), W h i t e et al (1967) at 3·5 – 7·5 pH, 25° – 200 °C temperatures, 4 – 140 at pressures.

Based on conclusions about the $HgS - H_2O - Na_2S$ system, it seems that alkalinity has favourable effect on the formation of HgS. The $(SO_4)^{2-}$ content of alkaline hot brines (Na_2SO_4)indicates that Na_2S has an important role in solubility and transport of HgS. Based on

$$HgS + Na_2S_{(aq)} \rightleftarrows NaHgS_2 \text{ reaction,}$$

$$K \text{ is equal to } \frac{Na_2HgS_2}{(Na_2S)HgS}$$

hence Na_2S increases the solubity of HgS. Whit increasing temperature the solubity of silicates (e. g. quartz) is also increasing. This gives an explanation for the relationship of HgS mineralization and silicecus environment. The coefficients of solibility:

Cinnabar $K = 10^{-3,50}(10^{-3,51})$ (S c h w a r z e n b a c h – Widmer) Metacinnabar $K = 10^{-59}(10^{-3,60})$ (S c h w a r z e n b a c h – Widmer) The solubility of HgS in the $HgS_{(s)} - Na_2S_{(aq)}$ system is increasing from 20 °C to 100 °C, decreasing between 100° – 150 °C, then gradually increasing. At room temperature the solubility of metacinnabar is 30 per cent larger than that of cinnabar. Until the inversion teperature for metacinnabar-cinnabar (344 °C) is not reached 30 per cent of the crystalline phase is cinnabar.

The irreversibility of $HgS_{(s)} + Na_2S_{(aq)} \rightleftarrows Na_2HgS_2$ system is highly influenced by the CO_2 content and oxygene saturation of the solution. This phenomene plays inportant role in the formation of HgS and mercury deposits in carbonate environment (A l g e r i a, N e w I d r i a – USA, R ó k a h e g y – Hungary)

In the $HgS_{(s)} + 2H_2S_{(aq)} \rightleftarrows HgS(H_2S)_{2(aq)}$ system at 20 °C temperature

$K = 10^{-4,25}$ cinnabar
$K = 10^{-4,31}$ metacinnabar

In the $HgS + S^{2-} = Hg_2^{2-}$ system B a r n e s (1976) suggested

$K = 10^{+0,57}$ = metacinnabar
$K = 10^{+0,48}$ = cinnabar

These data indicate that formation of deposits composed of Hg – HgS are associated by alkaline $+ HgS_2^{2-}$ – hydrotermal solutions.

D r e y e r (1940) concluded that most HgS deposits form at near-surface conditions, on normal pressure. D i c k s o n (1964) stated that HgS mineralizations could form at low pressure (1 – 30 at) and temperature

100° — 230 °C from neutral — or slighthy alkaline solutions, because stabiliy ranges of Hg-complexes are determined by the above-mentioned physico-chemical parameters.

5 pH = $Hg(HS)_2$ less important in transport of *Hg*
6 — 8 pH = $Hg(HS)$ }
9 pH = HgS_2^{2-} } most abundant *Hg*-complex

In sulfide-complexes mercury is linked to chains with 2 or 4 coordination, these govern the development of chainstructures of cinnabar or framework structure of metacinnabar (B a r n e s et al. 1967. Fig. 1).

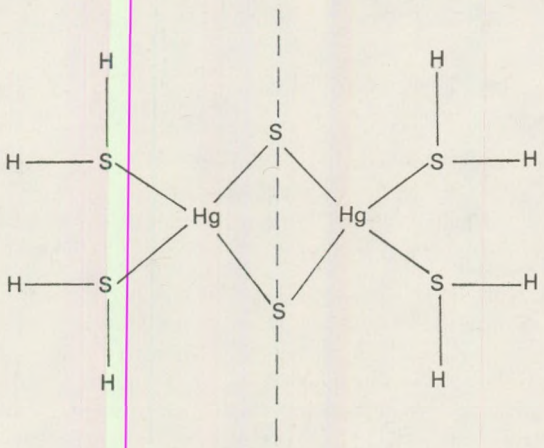

Fig. 1. Co-ordinating ligands of the HgS (B a r n e s et al.)

As indicated by several Hg-chloride minerals, transfer of mercury in chloride-complexes is also a possibility. The stability of Hg-chlorides is strongly temperature dependent, these minerals occur rarely compared to the HgS modifications, (K r a u s k o p f 1951).

The equlibrium constants of Hg-chloride complexes:

$$Hg^{2+} + Cl\ (HgCl)^{+}: K = \sim 10^{7,3}$$
$$Hg^{2+} + 4Cl(HgCl)^{2-}: K = \sim 10^{16,1}$$

Hydrothermal experiments

Laboratory experiments have been carried out in liquid-vapor and solid-liquid phase systems:

a) Synthesis of HgS monophase from solutions containing Hg^{+} and Hg^{2+} ions at 25° — 50° — 75° — 100°C temperatures

1. (0.1 mol $HgNO_{3(aq)} + H_2S_{(g)}$
2. 0.1 mol $HgCl_{2(aq)} + H_2S_{(g)}$

b) Effects of As^{3+}, Sb^{3+}, Tl^{+} on the formation of HgS (by Hg:R ratios of 100:1 and 1000:1):

1. 0,1 mol $HgCl_{2(aq)} + AsCl_3 + H_2S_{(g)}$
2. 0.1 mol $HgCl_{2(aq)} + SbCl_3 + H_2S_{(g)}$
3. 0.1 mol $HgCl_{2(aq)} + TlCl + H_2S_{(g)}$

As, Sb, Tl have been chosen as "impurities", because the stabilities of their sulfide-complexes are similar to that of HgS, atomic radii are near to that of *Hg*, and occur in epithermal ore deposit.

c) HgS ($=\beta$HgS-metacinnabar)$+H_2O$ and $\beta HgS_{(aq)} + Na_2S_{(g)}$ systems between $25_2 - 300$ °C. HgS is synthetised from $HgCl_{2(s)} + H_2S_{(aq)}$ system at 25 °C.

d) Metacinnabar (βHgS) in solutions with composition
Hg:R = 100:1 between $50° - 300$ °C. (R = As^{3+}, Sb^{3+}, Tl^{+}).
Laboratory experiments are calculated with mercury ions migrating in chloride-complexes, from wich HgS phases can be formed irreversibly by the effect of $H_2S - Na_2S$ hydrotermal solutions.
Hg-ions in nitrate complexes have been investigated to study the effect of synchronous or differentiated formation of $\alpha -$ and βHgS.

1) 0.1 *mol* $HgNO_{3(aq)} - H_2S_{(g)}$ *system*

The experiments have been carried out from 0.1 mol mercury (I) nitrate solution with initial pH 2.3. The pH value of the solution have been modified during the reactions:

25 °C	15 min	1.00 pH metacinnabar crystallites
	60 min	0.84 pH metacinnabar crystallites
	8 hours	0,85 pH cinnabar
	20 hours	0.85 pH cinnabar
	30 hours	0.85 pH cinnabar
50 °C	60 min	0.85 pH cinnabar
	8 hours	0.85 pH cinnabar + Hg-drops
65 °C	8 hours	1,19 pH $\beta HgS > \alpha HgS$
75 °C	60 min	1.05 pH βHgS crystallites
	4 hours	1.06 pH βHgS crystallites
	8 hours	1.21 pH $\beta HgS - \alpha HgS$?
	12 hours	1.19 pH βHgS
100 °C	10 min	1.01 pH –
	60 min	1.00 pH βHgS crystallites
	8 hours	(?) 1.0 pH $\beta HgS > \alpha HgS$

* The use of mercury (I)-nitrate is supported by two factors
a) very low solubility of Hg_2Cl_2,
b) anion effects on the formation of HgS modifications.

These data indicate that acidity of solutions formed within the same time-intervals (8 hours) is larger for αHgS (pH 0.85) than for βHgS and $\beta HgS > \alpha HgS$(1.08 — 1.21 pH). Different time intervals (15 min — 30 hours) have been used for observations of transitional and accessorial phases during the experiments. It was found that formation of stabile sulphide phases is preceded by multi-phase precipitation of white or greyish-white *Hg*-compounds: ($HgNO_3 \cdot 2H_2O$; $NHg_2OH \cdot 2H_2O$ and $NHg_2(NO_3)$. The advance of the process is marked by the increasing, appearance of black and brownis-red precipitation of HgS (Table I.)

Table I.

Crystalline phases of the $HgNO_{3(aq)} - H_2S_{(g)}$-system

Temperature	Time	Colour of reaction product	Crystalline phases
25°C	15 min.	dark gray	βHgS crystallites + Hg_3, Hg_4, Hg_6, Hg_7
25°C	60 min.	black	$\beta HgS + Hg_4$
25°C	8 hours	reddish-brown	αHgS + metallic Hg drops
25°C	20 hours	brown	$\alpha HgS + Hg +$,,
25°C	30 hours	reddish-brown	$\alpha HgS +$,,
50°C	60 min.	black and gray	αHgS, Hg_4
50°C	8 hours	brown reddish brown	$\alpha HgS + (-)$
65°C	8 hours	dark-gray	$\beta HgS \gg \alpha HgS + Hg + Hg_3S_2(NO_3)$?
75°C	60 min.	black lamellae, gray	$\beta HgS + Hg_3$, Hg_4
75°C	4 hours	gray	$\beta HgS + Hg_3$, Hg_4, $Hg_3S_2(NO_3)$
75°C	8 hours	gray, grayish white	βHgS, $\alpha - HgS(?) + HgNO_3$, Hg_4
75°C	10 hours	black and gray	$\beta HgS + Hg_3$, Hg_4
75°C	12 hours	black	$\beta HgS \gg \alpha HgS + Hg_4$
100°C	60 min.	gray, black	βHgS crystallites + Hg_3, Hg_4, Hg_7
100°C	8 hours	black, pale gray	$\beta HgS \gg \alpha HgS + Hg_3 + Hg_4 + Hg_7$

$Hg_3 = HgNO_3$
$Hg_4 = Hg(NO_3)_2 \cdot 2\,H_2O$
$Hg_6 = Hg_2S_2(NO_3)$
$Hg_7 = NHg_2(OH) \cdot 2\,H_2O$

In the $Hg(NO_3)_{(aq)} - H_2S$ system the cubic βHgS had been formed first at all temperatures, along whit $HgNO_3$, $HgNO_3 \cdot 2H_2O$, $Hg(NO_3)_2 \cdot 2H_2O$ and possibly $Hg_2S_2(NO_3)$. Following the formation of $Hg_2S_2(NO_3)$ the $HgNO_3$ bonds can split, $Hg(HS)$, $Hg(HS)_2$, HgS_2^{2-} complexes and finally the poorly soluble HgS can form. No other final phases exist beside cinnabar (αHgS). The solution exhibits the greatest acidity (0.85 pH).

Pure HgS phases have been obtained at 25° — 50 °C temperature, 8 hours. At 75 °C in different time intervals (4 — 8 hours) both βHgS and αHgS + ? had been formed, herefore experiments have been repeated at 65 °C (8 hours to obtain more exact data about $\beta HgS \rightleftarrows \alpha HgS$ reaction. These experiments indicated that in the $HgNO_3 + H_2S$ system the temperature interval for contemporaneous formation of βHgS and αHgS is 50° — 65 °C:

$$\beta\ HgS \rightarrow \alpha HgS \rightarrow [\beta\ HgS + \alpha HgS] \gg \alpha\ HgS.$$

The sulphur-content of the crystalline phases in the $HgNO_3 - H_2S$ system is highly variable due to formation of mercury:

25 °C/8 hours = +0.91% Hg and
−5.65% S
25 °C/20 hours = +3,28% Hg(Hg – drops have been separated)
−20.51% S(!)
50 °/8 hours = +3.74% Hg (Hg-drops have been separated)
−30.44% S(!)

Stochiometric ratios of HgS are shown in Table VI. Stochiometric ratios (Hg:S) could not be determined precisely due to formation of metallic *Hg* and different *Hg*-nitrate complexes. (βHgS > αHgS phases formed during reactions at 65° – 75° – 100 °C/8 hours have not been analysed du to inadequate quantities of material obtained).

The c_0/a_0 cell parameters of αHgS formed at 25° – 50 °C = 2.2891 – – 2.2945 Å, at 75° – 100° theses values change to 2.3015 and 2.3064 Å respectively, indicating that the cell become more elongated. The a_0 = = 5.8682 – 5.8752 Å of βHgS crystallites formed at 75 °C/60 min and 100 °C/60 min indicate less packed, while a_0 = 5.8466 – 5.8597 Å parameters obtained from ecperiments of 8 – 12 hours duration show tightly packed cells as compared indicating that the cell become more elongated. The a_0 = 5.8682 – 5.8752 Å of βHgS crystallites formed at 75 °C/60 min and 100 °C/60 min indicate (Table II and Fig. 2)

Table II

Chemical composition of the crystalline phases of the $HgNO_{3(aq)} + H_2S_{(g)}$-system

T°	Hg	S
25°C	73,63 – 79,63%	11,02 – 9,74%
50°C	81,70 – 89,43%	9,77 – 9,60%
75°C	82,80 – 88,75%	5,83 – 7,73%
100°C	71,13 – 78,89%	6,88 – 10,21%

2) $HgCl_{2(aq)} - H_2S_{(gas)}$ *system*

The initial solution was 0.1 mol Hg (II) chloride with 4.1 pH, characterised by the following thermodinamical parameters:

F° = −42.2 Kcal/mol Robert (1971)
F° = −50.53 Kcal/mol Robert (1971)

In every case 500 ml solution have been used, reactions at 25°, 50°, 75°, 100 °C with durations of 8 hours- 45 min have been studied. During the experiments acidity have significantly decreased with time and temperature (pH = 0.70 – 1.90).

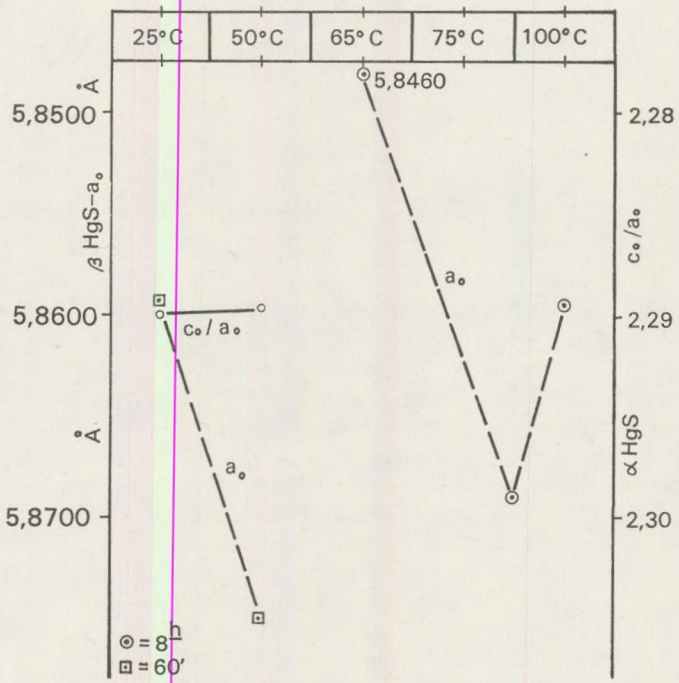

Fig. 2. $c_0/a_0 + a_0$ data of the crystalline phases of the $HgNO_{3(aq)} - H_2S$-system.

25 °C	60 min	2.35 pH	
	95 min	1.75 pH	βHgS crystallites
	8 hours	0.84 pH	βHgS
50 °C	8 hours	0.82 pH	βHgS
75 °C	8 hours	0.80 pH	βHgS$\gg\alpha$ HgS
100 °C	45 min	1.90 pH	
100 °C	8 hours	0,70 pH	βHgS$\gg\alpha$ HgS

During the reaction precipitation of white colour ($\alpha - \gamma HgS_3S_2Cl_2$) have been formed first, followed by greyish and black products. At 25° – 50 °C metacinnabar, at 75° – 100° βHgS + αHgS phases (with βHgS dominance) precipitated, associated by the following accessories:

25 °C	60 min	gray greyish white	$\alpha - \beta Hg_3S_2Cl_2$
25 °C	– 95 min	*a)* greenish-grey βHgS crystallites and *b)* pale-grey *c)* grey	$\alpha - \gamma Hg_3S_2Cl_2$
25 °C	8 hours	black	$\beta HgS + \gamma Hg_3S_2Cl_2$
50 °C	– 8 hours	black	$\beta HgS + \gamma Hg_3S_2Cl_2$
75 °C	– 8 hours	black	$\beta HgS + \alpha HgS + \gamma HgS_3S_2Cl_2$

100 °C – 45 min	*a)* greenish grey	
	b) pale-grey	$\alpha - \gamma\ Hg_3S_2Cl_2$
	c) grey	
100 °C – 8 hours	black	$\beta > \alpha HgS + Hg_3S_2Cl_2$

The initial products of reactions in the $HgCl_{2(aq)} - H_2S_{(g)}$ system are the α- and $\gamma Hg_3S_2Cl_2$. From the two the modification has larger stability, however its presence in products of reactions at 75° – 100 °C was not observed. Unlike in the Hg(I)-nitrate – $H_2S_{(g)}$ -system, βHgS with sphalerite-type structure has been formed at 25° – 50°C temperature. At 57° – 100 °C βHgS was the dominant product, but αHgS has also ben recorded.

This indicates that in solution-vapor system the $\beta HgS \rightleftarrows \alpha HgS$ reaction takes place between 50°-and 65 °C. This has an implied explanation for controversial observations in natural systems, regarding the βHgS and αHgS precipitation sequence, (in several cases the black βHgS, in other cases the purple αHgS was recordedas first precipitation).

The formation of βHgS begin after the saturation of the solution with respect to sulphur has reached 60 per cent. Below this value of sulphur-saturation $\gamma Hg_3S_2Cl_2$ have been produced.

The chemical composition of crystalline phases of the $HgCl_{2(aq)} - HgS_{(g)}$ system (from expriments of 8 hours duration) are "richer" in Hg and S than the the products of Hg (I)-nitrate – $H_2S_{(g)}$ – system (Table III. and Fig. 3).

The data obtained from the analyses indicate that the HgS formed in the Hg(II)-chloride – H_2S system depleted in cations (Hg). but all the S-positions have been filled (?) (Table IV and VI).

Table III.

Chemical composition of the crystalline phases of the $HgCl_{2(aq)} - H_2S_{(g)}$-system

T°	Hg	S	Cl	H_2O
25°C	85,84%	13,98%	0,26%	0,00%
50°C	84,79%	14,00%	0,15%	0,03%
75°C	85,04%	13,96%	0,41%	0,07%
100°C	84,56%	13,10%	2,19%	0,04%

The a_0 structural parameter of βHgS is decreasing with the rising temperature. The c_0/a_0 parameters of the αHgS have not calculated, as only few d/Å data has been obtained.

$$25°/8h : a_0 = 5.8610\ Å$$
$$50°/8h : a_0 = 5.8408\ Å$$
$$75°/8h : a_0 = 5.8011\ Å$$
$$100°/8h : a_0 = 5.7441\ Å$$

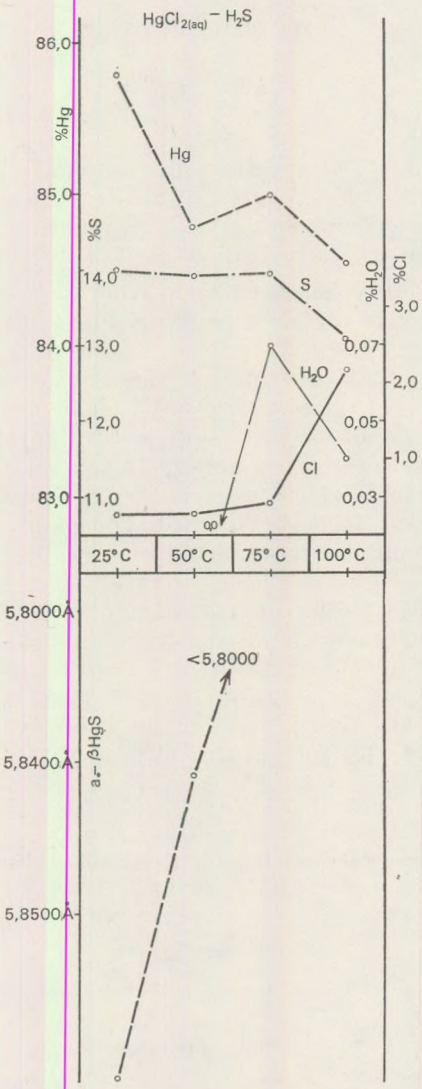

Fig. 3. Chemical composition of the crystalline phases of the $HgCl_{2(s)} - H_2S_{(g)}$ – system.

The decreasing cell-parameters of βHgS at 75° – 100 °C can be related to the initial formation of αHgS structure.

Table IV.

The non stochiometric composition of the $HgS_{(s)} + H_2O$; Na_2S; R-chlorine systems

System	Hg				S			
	25°C	50°C	75°C	100°C	25°C	50°C	75°C	100°C
$HgNO_{3(aq)} - H_2S$	−0,91	−3,74	–	–	−5,65	−30,44	–	–
$HgCl_{2(aq)} - H_2S$	−0,42	−1,90	−1,35	−1,90	−1,30	−5,07	+1,16	−5,07
100:1								
$HgCl_{2(aq)} - AsCl_{3(aq)}\ H_2S$	−4,40	−3,27	−3,41	−1,36	+2,97	+3,55	+5,00	+5,29
$HgCl_{2(aq)} - SbCl_{3(aq)} - H_2S$	−5,22	−4,34	−3,55	−3,47	−0,07	+10,58	+5,00	+10,94
$HgCl_2 - TlCl - H_2S$	−3,93	−3,74	−2,94	−3,25	+2,25	+2,97	+4,86	+2,97
1000:1								
$HgCl_{2(aq)} - AsCl_3 - H_2S$	−0,28	−4,43	−4,47	−3,90	+1,23	+0,87	+1,74	+10,72
$HgCl_{2(aq)} - SbCl_3 - H_2S$	−0,07	−1,76	−1,04	−4,19	+2,68	+0,29	+1,09	−0,29
$HgCl_{2(aq)} - TlCl - H_2S$	−3,45	−4,44	−2,73	−4,30	+2,25	+2,39	+2,17	+3,19

3. *Experiments for recrystallization of βHgS formed at 25 °C in the temperature range between 25 – 350°C*

3.1. $HgS_{(s)} - H_2O$

The structural inversion of βHgS, which was formed in *Hg*-chloride-H_2S system has characteristic features (posthydrothermal effect structural framework diagenesis).

The crystalline product, formed at 25°C/8 hours has the following composition:

Hg	= 85.79%
S	= 14.00%
Cl	= 0.26%
H_2O	= 0,00%
	100,05%

wich is equal to

βHgS	= 97.31%
$Hg_3S_2Cl_2$	= 2.69%
	100.00%

phase-composition. The compositional changes of this product in the 25° – 300°C temperature range are shown in Fig. 4. (30 days at 25°C, 24 hours at 50° – 300°C)

The *Hg* content is decreasing with an average 1.77 per cent, while the *S* content remains practically unchanged (+0.01%). The four *Hg*-"maximum" and three *Hg*-"minimum" varies with the temperature:

Hg-"maximum" = *a)* 25°; *b)* 75°; *c)* 175° – 200°; *d)* 350°C
Hg-"minimum" = *a)* 50°; *b)* 100° – 150°; *c)* 250° – 300°C.

The *Cl* content is reducing with an average of 0,09 per cent, with the largest amount at 125° – 150°C (=0,04%, 85 per cent of *Cl* content) and at 200°C. Approximately 40 per cent of total *Cl* content can be removed without any sign of destruction. The pH factor of the solution have been stabilized at 4.82 – 3.9 between 25° – 75°C, above temperature it has become more acid at an average pH 2.24 (in the range of 2.10 – 2.37).

The inversion of βHgS to cinnabar starts at 25 °C/30 days. Between 25° – 150°C the βHgS is still the dominant phase (βHgS > αHgS), their proportion shows an opposite change between 175° – 250°C, and only mono-phase αHgS have been observed at 300° – 350° C (Fig. 5 and 6).

Using these results in the interpretation of mineral genesis it can be concluded the βHgS (metacinnabar) wich have initially crystalised from the hydrothermal solutions, can be altered to αHgS (cinnabar) at low temperatures by the effect of post-ore solutions. At higher temperatures the rate of inversion in increasing, and from 175°C the αHgS is the dominant crystal-phase. We dont have data about the rate of inversion below 175°C (It is possible that βHgS → αHgS precipitations in eocene Nummulite-limestone at Rókahegy – Budapest can be explained with this processes).

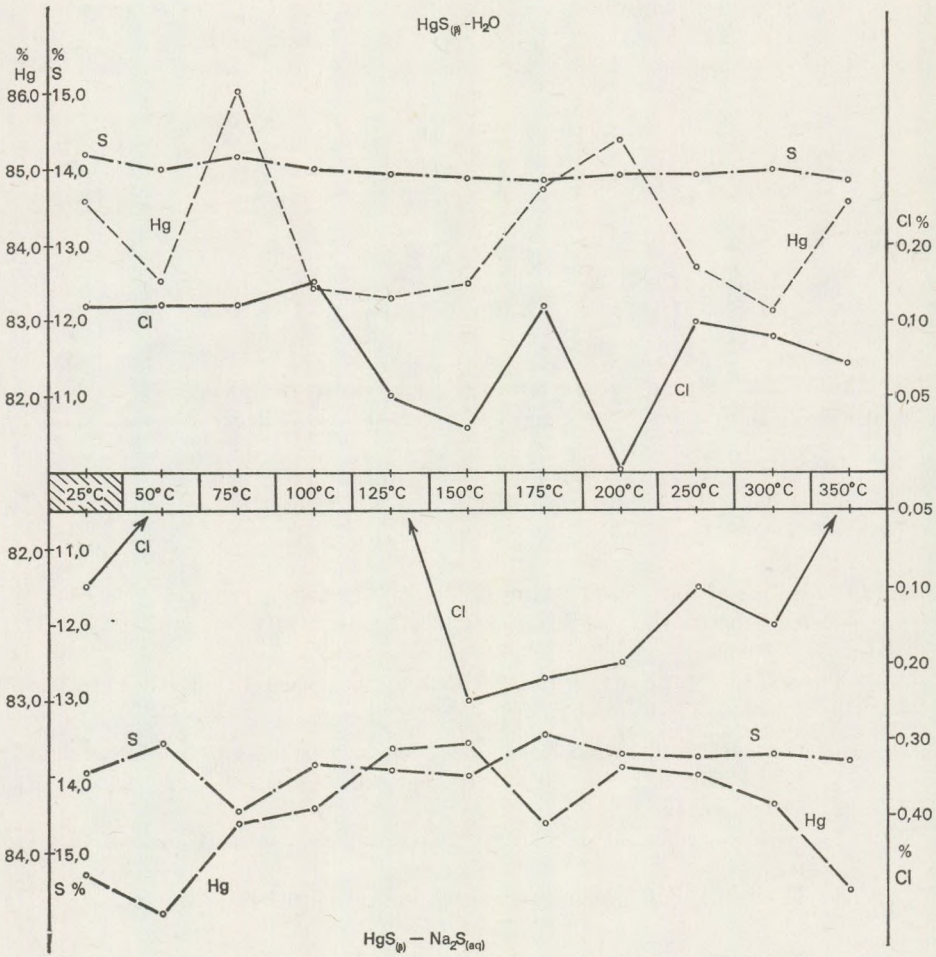

Fig. 4. The composition of $HgS_{(s)} + H_2O$ and $HgS_{(s)} + Na_2S_{(aq)}$ crystal phases as a function of T°

SYSTEM	METACINNABAR (βHgS)–CINNABAR (αHg)										
	25°C	50°C	75°C	100°C	125°C	150°C	175°C	200°C	250°C	300°C	350°C
	β > > α	β > > α	β > > α	β > > α	β > > α	β > > α	α > > β	α > > β	α > < β	α	α
$HgS_{(\beta)} - Na_2S_{(aq)}$	β > > α	β > > α	α > > β	α	α	α	α	α	α	α	α
$HgS_{(\beta)} - AsCl_{3\,(aq)}$	β	β	β	β	β	β	β > > α	α > > β	α > > β(?)	α	α
$HgS_{(\beta)} - SbCl_{3(aq)}$	β	β > α (?)	β > α (?)	β	β ⩾ ⩾ α	β ⩾ ⩾ α	α > > β	α > > β	α	α	α
$HgS_{(\beta)} - TlCl_{(aq)}$	β	β	β	β	β	β > > α	β > > α	β > > α	α > > β	α	α

Fig. 5. Phase relations of HgS + solution systems.
The upper line refers to the $HgS(\beta) - H_2O$ system

In the non-stochiometric compositions of the $\beta HgS > \alpha HgS$ (at 25° – 150°C), the $\alpha HgS > \beta HgS$ (at 175° – 250°C) and αHgS (300° – 360°C) crystalline phases the following relationships have been observed (Table V and VI).

a) $\beta HgS > \alpha HgS$ = −0.15 − 3.33% *Hg*-deficiency and +0.94 + 4.06% *S*
b) $\alpha HgS > \beta$ HgS = −0.89 − 2.88% *Hg*-deficiency and +0.65 + 1.16% *S*
c) αHgS = −1.88 − 3.52% *Hg*-deficiency and +5.58 + 1.52% *S*

Mean values

a) $\beta HgS > \alpha HgS$ = −2.46% *Hg* + 2.02% *S*
b) $\alpha HgS > \beta HgS$ = −2.37% *Hg* +0.84% *S*
c) αHgS = −2.70% *Hg* +1,05% *S*

It seems that αHgS is no the average more deficient in cations than βHgS (However B a r n e s and S c o t t suggested the β HgS as *S*-deficient)

3.2. $HgS_{(s)} - Na_2S_{(aq)}$

Literature data show that the best solvent for HgS is the aqueus solution of Na_2S (D i c k s o n 1964 B a r n e s - R o m b e r g e r - S t e m p r o k − 1967). Solubility is related to the contrentration of Na_2S, at 250°C and 1800 bar has a value of 30 g/l. Phase-alterations has not been mentioned except that at temperatures below 344°C approximately 30% αHgS was formed.

The experiments in the $HgS_{(s)} - Na_2S - H_2O$ system have been initiated by the following problems:

a) the saturation of *S*-deficient position can take place diagenetically
b) if chlorine is removed the transitional reaction predict, $\gamma Hg_3S_2Cl_3$ alters to HgS,
c) what is the alteration temperature of complete inversion of βHgS to αHgS,
d) How the cell-parameters are changing during the $\beta HgS \rightarrow \alpha HgS$ alterations.

0.1 mol Na_2S solution has been used for the expreriments with the $HgS_{(s)} - Na_2S - H_2O$ system. Experiments have been carried out in Pyrex-phials, in closed system. (The duration of experiments was 30 days at 25°C, 24 hours at 50° – 350°C).

The chemical composition of the initial $\beta HgS_{(s)}$ showed the following variations during the phase alterations at 25° – 350°C (average values):

25° – 50° = −1.51% *Hg*, −0.22% *S*
75° – 300° = −2.23% *Hg*, −0.15% *S*
350° = −1.54% *Hg*, −0.21% *S*

The following Cl contents have been analysed:

150° – 200°C = 0.20 − 0.25% *Cl*
25° – 125°C = 0 − 0.10% *Cl*
250° – 350°C = 0 − 0.15% *Cl*

The pH of the solution showed slightly decreasing tendency:

$$25° - 200°C = 9.86 - 10.35$$
$$250° - 300°C = 9.58 - 8.24$$

The βHgS phase alterations in the $HgS - Na_2S - H_2O$ system indicate that $Na_2S + H_2O$ solution (post-ore hydrothermal solution) accelerates the formation of αHgS and at $100° - 350°$ exlusively mono-phase cinnabar structure is formed:

a) $25° - 50°C$ = black, $\beta HgS > \alpha HgS + \gamma Hg_3S_2Cl_2$
b) $75°C$ = brownish-red $\alpha HgS > \beta HgS + \gamma Hg_3S_2Cl_2$
c) $100° - 175°C$ = purple $\alpha HgS + NaHgCl_3 \cdot 2H_2O$
d) $200° - 350°C$ = purple $\alpha HgS + \gamma Hg_3S_2Cl_2$

(Table V., VI. and Fig 4.)
The non-stochiometric compositions of $\beta HgS > \alpha HgS$; $\alpha HgS > \beta HgS$ and αHgS:

$25° - 50°C = \beta HgS > \alpha HgS = -2.09 - 2.35\%\ Hg,\ 1.16 - 1.52\%\ S$
$75°C = \alpha HgS > \beta HgS = -1.53 - 2.23\%\ Hg,\ -0.65 + 4.9\%\ S$
$100° - 350°C = \alpha HgS = -2.26\ \ 3.40\%\ Hg,\ -0{,}07 + 1.52\%\ S$

Mean values:

$25° - 50°C = \beta HgS > \alpha HgS = -2.22\%\ Hg - 0.36\%\ S$
$- 50°C = \beta HgS > \alpha HgS = -2.22\%\ Hg - 0.36\%\ S$
$75°C = \alpha HgS > \beta HgS = 2.18\%\ Hg + 2.56\%\ S^*$
$100° - 350°C = \alpha HgS = -2.98\%\ Hg - 0.80\%\ S$

On the average αHgS shows larger *Hg* and smaller *S* deficiency than βHgS, the *Hg*:*S* ratio of αHgS approximates the ideal 1:1 value better than that of βHgS. The celle parameter for βHgS $a_0 = 5.8521 \pm 0.0007$ Å, is unaffected by temperature changes. The c_0/a_0 value of αHgS differs from literature data (2.30 Å) with -0.01 Å (Fig. 6).

a) The results given by the experiments in the $HgS_{(s)} - Na_2S_{(aq)}$ system indicate that effects of H_2S solutions promote splitting of $[HgS_4]$-tetrahedra of βHgS and their chain like linear rearangement (cinnabar structure). It also causes the alteration of accessorial $\gamma Hg_3S_2Cl_2$ phase to αHgS by removing *Cl*. The non-stochiometric character of αHgS becames smaller despite the number of unfilled *S*-positions being larger than of βHgS.

b) The initially formed less stabile βHgS phase alters to cinnabar quite easily, therefore αHgS is more abundant in nature. Coexisting $\alpha - \beta$ HgS indicates meta-phase transitional stage, which can explain the controversial conclusions in previous studies about the phenomene that both meta-cinnabar adn cinnabar have been observed as first precipitation.

* From data of 8 – 24 – 30 hours experiments.

Table V.

The non stochiometric composition of the HgS

System	±Hg / ±S	25°C	50°C	75°C	100°C	125°C	150°C	175°C	200°C	250°C	300°C	350°C
$HgS_{(\beta)} - H_2O$	±Hg	−1,87	−3,07	−0,15	−3,20	−3,33	−3,14	−3,36	−0,89	−2,88	−3,52	−1,88
	±S	+2,90	+2,03	+4,06	+1,52	−0,72	+0,94	+0,36	+1,16	+1,01	+1,52	+0,58
$HgS_{(\beta)} - Na_2S_{(aq)}$	±Hg	−2,35	−2,09	−2,78	−2,89	−3,32	−3,40	−2,77	−3,20	−3,14	−2,91	−2,26
	±S	+1,16	−1,52	+4,92	+0,14	+0,72	+1,52	−2,54	−0,42	−0,43	−0,97	−0,07
$HgS_{(\beta)} - AsCl_{3(aq)}$	±Hg	−3,91	−2,10	−1,73	−3,27	−1,91	−1,82	−1,47	−2,08	−2,44	−0,82	–
	±S	−3,26	+1,88	+5,00	+5,00	+5,87	+5,43	+2,46	+7,32	+7,97	+3,84	–
$HgS_{(\beta)} - SbCl_{3(aq)}$	±Hg	−0,07	−1,21	−0,38	−0,60	−2,27	−2,95	−0,53	−0,53	−1,87	−0,14	–
	±S	+0,22	+1,09	−0,22	+0,72	+1,09	+0,29	+1,38	+0,87	0,00	−0,71	–
$HgS_{(\beta)} - TlCl_{(aq)}$	±Hg	−2,77	−2,30	−2,89	−1,54	−1,35	−0,15	−1,97	−3,62	−2,97	−2,15	−2,95
	±S	−0,65	−0,22	+2,39	−1,23	−1,88	+0,29	−0,65	+0,72	+0,58	−0,94	+1,23

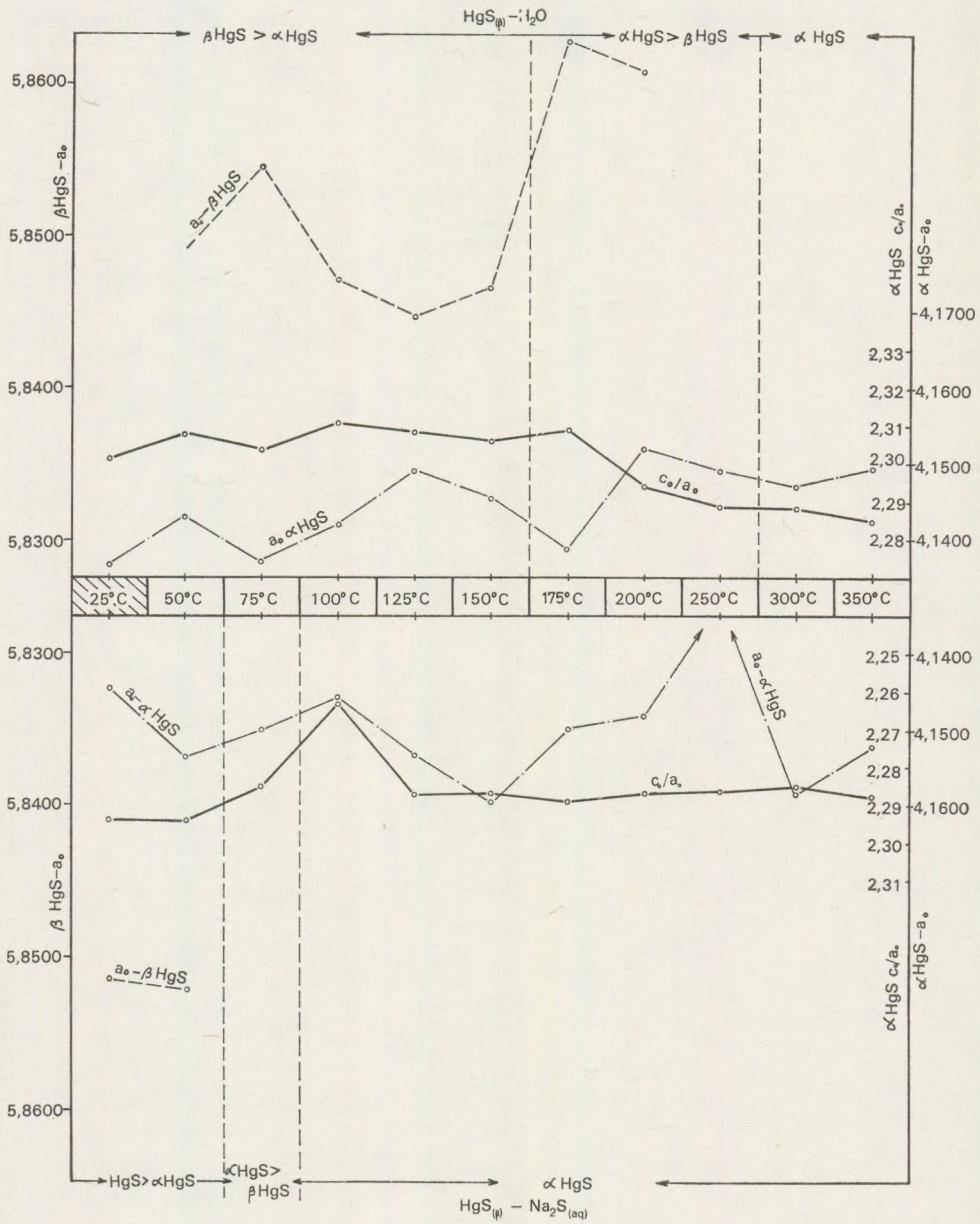

Fig. 6. Structural parameter variations of crystalphases of $HgS_{(s)} - H_2O$ and $HgS_{(s)} - Na_2S_{(aq)}$

4. *Experiments with the formation of (Hg, R) S from* $HgCl_{2(aq)}$ *+ R-chloride +* H_2S *and* $HgS_{(s)}$ *+ R-chloride system* (R = *As, Sb, Tl*)

4.1. $HgCl_{2(aq)} - AsCl_3 - H_2S_{(s)}$ (25°, 50°, 75°, 100°C)

a) Hg : As = 100 : 1
b) Hg : As = 1000 : 1

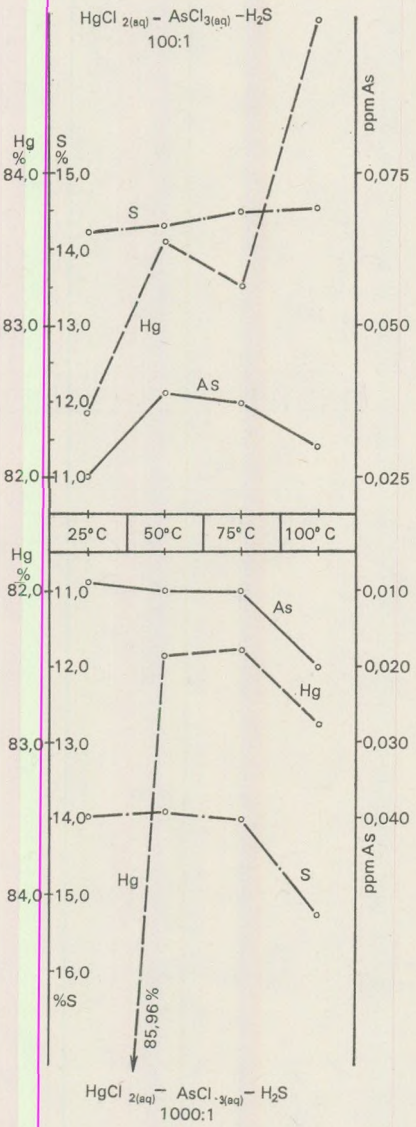

Fig. 7. Analysis data of $HgCl_{2(aq)} - AsCl_{3(aq)} - H_2S$ system

The crystalline product both systems (100:1, 1000:1) is powder-like black. The crystalline phase is βHgS, wich contained about 2 – 3 per cent $\gamma Hg_3S_2Cl_2$ impurities. It seems that with rising temperature the *Hg*, *As* and *S* exhibit little of any variation. Data of analyses are summarised in Fig. 7. The largest differences were recorded in *Hg*-content in the experiments at 25°C and 100°C. The closest correlation of *Hg-As-S* have been observed in the 1000 : 1 = Hg:As system (Fig. 7).

The average values of the analysis:

100 : 1 83.56% *Hg*; 14.38% *S*, 0.032% *As*
1000 : 1 83.38% *Hg*; 14.30% *S*; 0.012% *As*
(pH of the solution: 0.64 – 0.61)

The non-stochiometric distribution of Hg – S in crystalline phase is almost unaffected by the *As* content (Table IV., and VI).

100 : 1 *Hg* = –3.11% *S* = +4.20% *As* = 0.03%
1000 : 1 *Hg* = –3.27% *S* = +3.64% *As* = 0.01%

The largest *Hg* deficiency is in the 100:1 system at 100°C and in the 1000 : 1 system at 25°C, in βHgS phases. The βHgS cell-parameters are the smallest in this system, (average values)

100 : 1 = 327,5 ppm *As*, a_0 = 5.8396 Å
1000 : 1 = 122,5 ppm *As*, a_0 = 5.8415 Å

The difference between Hg° = 1.51 Å and As° = 1.48 Å is small, hence substition does not necessarily cause change in the cell parameters. However, the larger difference between Hg^{+} = 1.10 Å and As^{3+} = 0.58 Å caused cell contraction at 100 – 300 ppm *As* content.

The 100 : 1 system contains 327.5 ppm *As*, this explains the small average a_0 values in βHgS. Fig 8. shows that a_0 values are smaller than literature data and among the experimental data the smallest values have been obtained by no means in this system.

4.2 $HgS_{(s)} + AsCl_{3(aq)} - 100 : 1$

The crystalised products of the $HgS_{(s)} - AsCl_{3(aq)}$ system can be grouped in distinct temperature intervals. The mean values of analysis are arranged according the increasing temperature (Fig. 9).

a) 25 – 150°C = βHgS
b) 175°C = βHgS > αHgS
c) 200 – 250°C = αHgS > βHgS
d) 300°C = αHgS

a) 25° – 150°C = 84.08% *Hg*, 14.08% *S*, 20 ppm *As*
(pH = 1.56 – 1.67)
b) 175°C = 84.93% *Hg*, 14.14% *S*, 15 ppm *As*
(pH = 1.36)

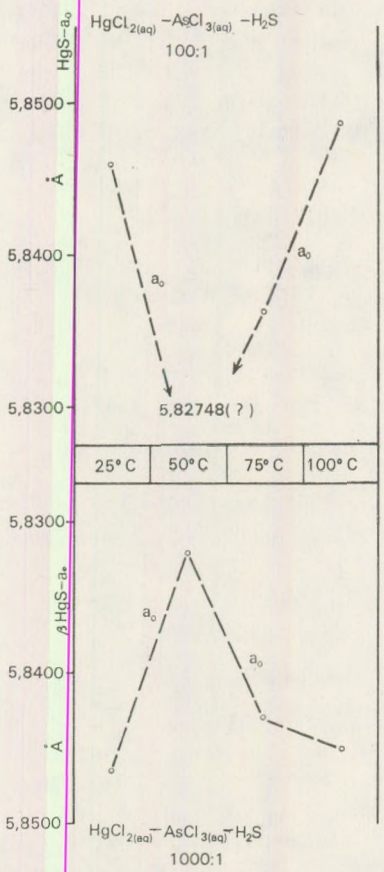

Fig. 8. Cell-parameters in $HgCl_{2(aq)} - AsCl_{3(aq)}$ – system

c) 200 – 250°C = 84.26% *Hg*, 14.86% *S*, 12,5 ppm *As* (pH = 1.36)
d) 300°C = 85.49% *Hg*, 14.33% *S*, 10.0 ppm *As* (pH = 1.45)

With increasing temperature the crystalline phases which contain 97 – 98% HgS show relative increase of HgS content and decreasing of *As*. The *Hg*-deficiency is decreasing the *S*-surplus is increasing contemporaneously, with the following average values in αHgS – βHgS phases:

a) 25° – 150°C = −2.46% *Hg*, +4.61% *S* 20 ppm *As*,
b) 175°C = −1.47% *Hg*, +2.96% *S* 15 ppm *As*,
c) 200° – 250°C = −2.26% *Hg*, +7.64% *S* 12.5 ppm *As*,
d) 300°C = −0.82% *Hg*, +3.84% *S* 10.0 ppm *As*,
(from Table V).

Table VI.

The non-stochiometric composition of the HgS

System	βHgS		αHgS		βHgS> αHgS		αHgS> βHgS	
	±Hg	±S	±Hg	±S	±Hg	±S	±Hg	±S
$Hg(NO_3)_{(aq)} - H_2S$	–	–	+3,97	−23,05(!)	–	–	–	–
$HgCl_{2(aq)} - H_2S$	−1,33	+1,38	–	–	−1,65	−3,91	–	–
$HgCl_{2(aq)} - AsCl_{3(aq)} - H_2S$	−3,19	+3,80	–	–	–	–	–	–
$HgCl_{2(aq)} - SbCl_{3(aq)} - H_2S$	−5,22	−4,34	–	–	–	+8,50	–	–
$HgCl_{2(aq)}TlCl_{(aq)} - H_2S$	−3,71	+2,79	–	–	−3,51	+2,68	–	–
$HgS_{(\beta)} - H_2O$	–	–	−2,70	+1,05	−2,46	+2,03	−2,38	+0,84
$HgS_{(\beta)} - Na_2S$	–	–	−2,98	+1,09	−2,22	+0,18	−2,51	+2,14
$HgS_{(\beta)} - AsCl_3 - H_2O$	−2,29	+4,24	−1,63	+5,91	−1,47	+2,46	−2,08	+7,32
$HgS_{(\beta)} - SbCl_3 - H_2O$	−0,68	+0,60	−1,01	−0,71	−2,61	+0,69	−0,53	+1,13
$HgS_{(\beta)} - TlCl - H_2O$	−2,17	+0,40	−2,54	+1,09	−1,91	+0,36	−2,97	+0,58

Fig. 9. Analysis of $HgS_{(s)} - AsCl_{3(aq)}$ as a function of T°

The crystalline product of reactions at 25° – 150°C is dominantly βHgS, with 1 – 2 per cent of $\gamma Hg_3S_2Cl_2$ impurities. $\beta HgS > \alpha HgS$ has been formed at 175°C, $\alpha HgS > \beta HgS$ between 200°C and 250°C, pure αHgS at 300°C. From the pure phases, βHgS is an average more deficient in $Hg - S$ than αHgS (Table VI).

The cell-dimensions of βHgS are probably effected by the *As* content. The a_0 value of βHgS formed from solutions is smaller than those published in literature. After recrystalisation of the $HgS_{(s)} - AsCl_{3(aq)}$ system fall closer to these data. The values are increasing on higher temperatures:

$$\begin{aligned} 100:1\ (25° - 100°C) &= a_0 = 5.8396\ \text{Å} \\ 1000:1\ (25° - 100°C) &= a_0 = 5.8415\ \text{Å} \\ (175°C) &= a_0 = 5.8545\ \text{Å} \end{aligned}$$

The cell of αHgS formed along with βHgS is more elongated than the c_0/a_0 of that one formed as mono-phase.

$$\begin{aligned} \beta HgS > \alpha HgS &= c_0/a_0 = 2.2918\ \text{Å} \\ \alpha HgS > \beta HgS &= c_0/a_0 = 2.2909\ \text{Å} \\ \alpha HgS &= 2.2885\ \text{Å} \end{aligned}$$

Results are summarized in Fig. 10.

4.3. *$HgCl_{2(aq)} - SbCl_{3(aq)} - H_2S$ (25° – 50° – 75° – 100°C)*

a) $Hg : Sb = 100 : 1$
b) $Hg : Sb = 1000 : 1$

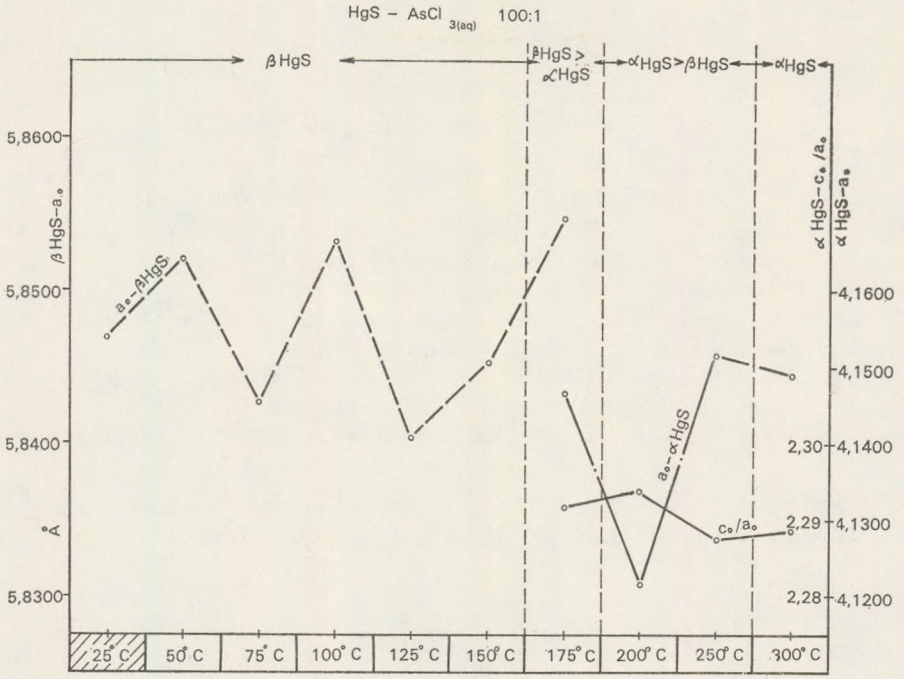

Fig. 10. Cell-parameters of crystalline-phases of $HgS_{(s)} - AsCl_{3(aq)}$ system

The antimony is the most abundant element associated with mercury mineralizations. Thus it seems reasonable to study the relationships of *Hg*-sulphides and antimony. The differences of atomic and ionic radii of the two elements:

$$\Delta = 0.15 \text{ Å (atomic radii)}$$
$$\Delta = 0.34 \text{ Å (ionic radii)}^*$$

The metallic bonds of the two element might not cause considerable change in the structural framework while with ionic linkage structural distortions possibly arise.

Black, isometric, nearly square- or diamond shaped crystallites have been formed in the systems 100 : 1 and 1000 : 1 = Hg : Sb

100 : 1

25°C	black	βHgS	pH = 0.2
50°C	black	βHgS	pH = 0.2
75°C	black	βHgS	pH = 0.2
100°C	black	β > αHgS	pH = 0.2

* = 0,22 Å at Whittaker – Muntus (1970)

1000 : 1

25°C	black	βHgS	pH = 0.2
50'C	black	βHgS	pH = 0.2
75°C	black	$\beta > \alpha$HgS	pH = 0.2
100°C	black	$\beta > \alpha$HgS	pH = 0.2

The monophase character of βHgS formed at 25° – 50°C is typical to the $HgCl_{2(aq)} - SbCl_{3(aq)} - H_2S$ system (Similar to the $HgCl_2 - H_2S$ system). From 75°C αHgS has also appeared, unlike with *As*. The amount of $\gamma Hg_3S_2Cl_2$ phase was ordes smaller than in the $HgCl_{2(aq)} - AsCl_{3(aq)} - H_2S$ system. The analysis of crystalline phases are shown in Fig. 11. This indicates that there is close relationship between *Sb* – *S* in both system and among *Hg* – *Sb* – *S* in the 1000 : 1 = Hg : Sb system.

The *Hg*-deficiency of the crystalline phase is larger in the 100 : 1 system than in the 1000 : 1 system. Significant variation in *S* content has been observed (Fig. 11., Table IV). The average non-stochiometric compositions.

100 : 1	= 82.62% *Hg*;	14.71% *S*;	0,77% *Sb*
1000 : 1	= 84.67% *Hg*;	13.93% *S*;	0.05% *Sb*

with differences of

100 : 1	= −4.15% *Hg*;	+6.66% *S*
1000 : 1	= −1.47% *Hg*;	+1.06% *S*

The greatest *Hg*-deficiency has been resulted in 100 : 1 system at 25°C and in 1000 : 1 system at 100°C. The *S* content in the 100 : 1 system has varied lin the range of −0.07, +10,94 (Table IV., and VI).

The βHgS formed at 25° – 100°C show cell dimensions nearly similar to literature data (being smaller, differs only in the third decimal):

100 : 1	= βHgS	= a_0 = 5.8472 Å	= 7700 ppm *Sb*
1000 : 1	= βHgS	= a_0 = 5.8483 Å	= 500 ppm *Sb*

The deformational effect of antimony can not be proved here. The distributions of cell parameters of βHgS follow similar trends both in system (100 : 1 and 1000 : 1), and show minimum at 100°C. (Fig. 12.)

4.4 $HgS_{(s)} - SbCl_{3(aq)} - 100 : 1$

Mono-phase βHgS has formed at 25° – 100°C, αHgS between 250° – 300°C, and mixed phases in 100°C – 250°C temperature range.

a) 25 – 100°C = βHgS*
b) 125 – 150°C = βHgS > αHgS
c) 175 – 200°C = αHgS > βHgS
d) 250 – 300°C = αHgS

* Formation of αHgS in form of crystal nuclei has probably started at 50 °C, but its presence is still uncertain at 75 °C.

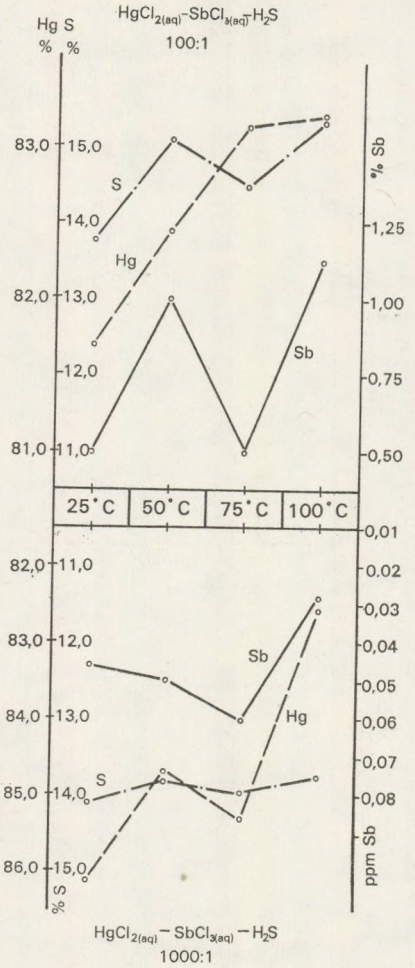

Fig. 11. Analysis data of $HgCl_{2(aq)} - SbCl_{3(aq)} - H_2S$ systems

$1-2\%$ $Hg_3S_2Cl_2$ is permanently present. From 75°C Sb_2S_3 was observed.

The *Hg* : *Sb* ratio in the composition of crystallized material showed inverse relationships, antimony crystallises dominantly as separate phase (Sb_2S_3), and its incorporation to the HgS structure is restricted.

The average of analysis results based in the distubution of β- and αHgS phases:

a) 25°−100°C = 85.74% *Hg*, 13.86% *S*, 2800 ppm *Sb*
b) 125°−150°C = 83.95% *Hg*, 13.89% *S*, 300 ppm *Sb*
c) 175°−200°C = 85.74% *Hg*, 13.83% *S*, 30 ppm *Sb*
d) 250°−300°C = 85.28% *Hg*, 13.85% *S*, 10 ppm *Sb* (Fig. 13.)

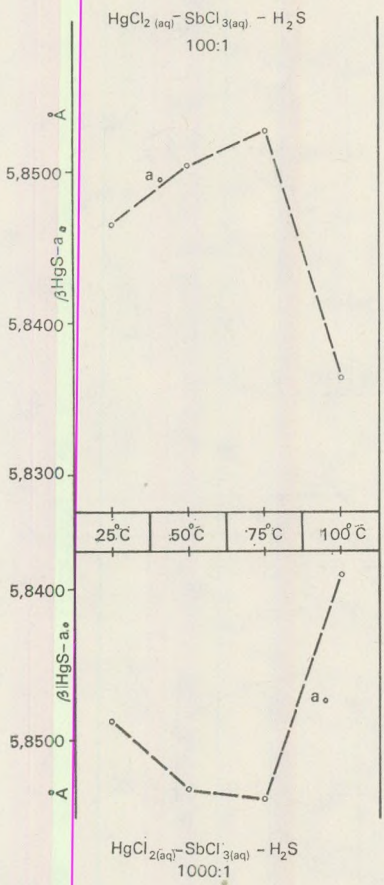

Fig. 12. HgS cell-parameters in the $HgCl_{2(aq)} - SbCl_{3(aq)} - H_2S$ systems

The $HgS_{(s)} - SbCl_3$ system shows the smallest *Hg*- and *S* deficiency. The Hg : S ratio exhibits close relationship with stochiometric values (based on data from Table V and VII).

$$\begin{aligned} a)\ & 25° + 100° = 0{,}76\ Hg, \quad +0.60\ S \\ b)\ & 125° + 150° = -2.61\ Hg, +0{,}64\ S \\ c)\ & 175° + 200° = -0.53\ Hg, +1.13\ S \\ d)\ & 200° + 300° = -1.00\ Hg, -0.35\ S \end{aligned}$$

Above 200°C the $HgS_{(s)} + SbCl_{3(aq)}$ system is characterised by α HgS phases having a special crystal-morphology. The average size of crystal grains is 0.2 — 0.5 mm with maximum of 1.0 mm. The antimony catalyses the inversion of βHgS to cinnabar signyficantly. At 300°C the rate of *Sb* impurity is only 10 ppm.

The a_0 parameter: of the metacinnabar (βHgS) phases form $HgS_{(s)} - SbCl_{3(aq)}$ system averaging the following values:

a) 25°C – 100°C = a_0 = 5.8457 Å, 2800 ppm *Sb*
b) 125°C – 150°C = a_0 = 5.8542 Å, 200 ppm *Sb*
c) 175°C – 200°C = a_0 = 5.8563 Å, 30 ppm *Sb*

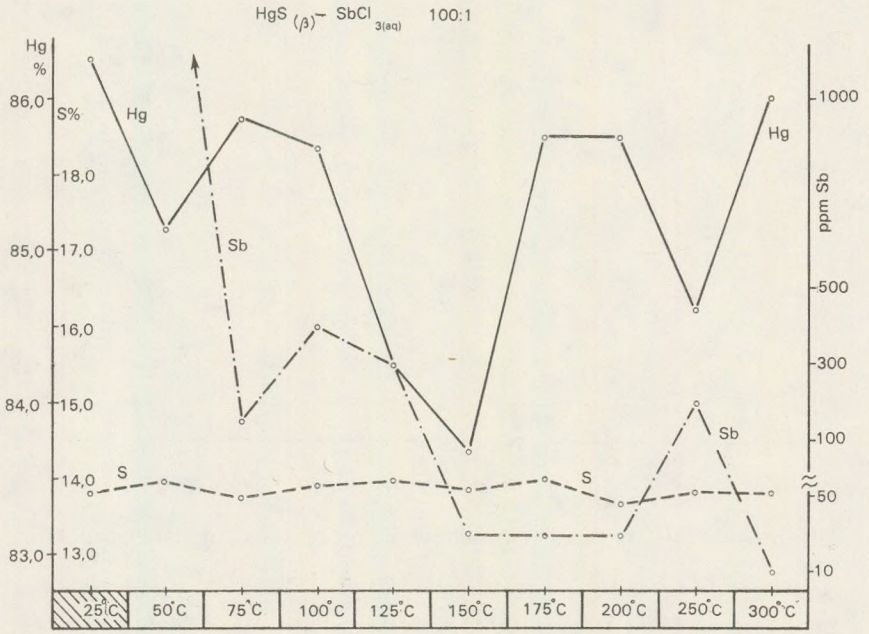

Fig. 13. Analysis data of crystalline phases of $HgS - SbCl_{3(aq)}$ as a function of T°

It seems that αHgS contains less *As* and *Sb* than βHgS with sphalerite-structure. The distributions of structural parameters of βHgS and αHgS are summarized in Fig. 14.

4.5. $HgCl_{2(aq)} - TlCl_{(aq)} - H_2S$ *(25° – 50° – 75° – 100°C)*

a) *Hg* : *Tl* = 100 : 1
b) *Hg* : *Tl* = 1000 : 1

Both mercury and thallium tends to cancentrate in epithermal deposits but only few data had been published about their genetical, geo-chemical relationship. For crystal-chemical reasons thallium has favourable characteristics to be in close assotiation with mercury. There is only minute difference between the atomic radii:

$$Hg^{\circ} = 1.51 \text{ Å}, \quad Tl^{\circ} = 1.60 \text{ Å} \quad \Delta = 0.09$$

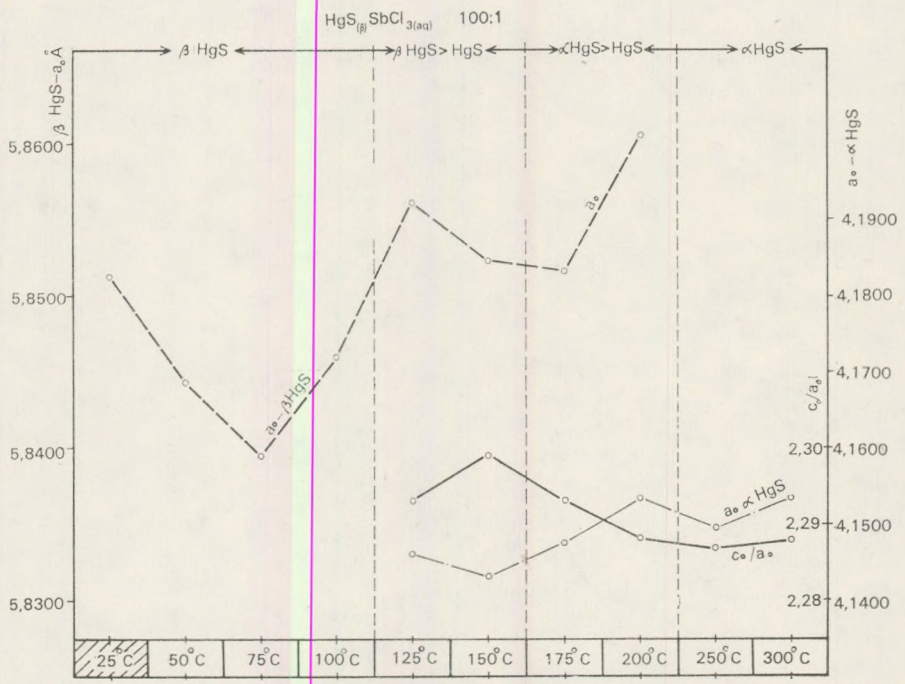

Fig. 14. Structural parameters of phases in $HgS_{(s)} - SbCl_{3(aq)}$ systems

The differences of ionic radii still permit isomorphous substitution:

$$Hg^{2+} = 1.10 \text{ Å}, \quad Tl^{+} = 1.47 \text{ Å} \quad \Delta = 0.37 \text{ Å}^*$$

The products of 100 : 1 and 1000 : 1 systems are black isometric, nearly square-sphaped grains and lamellae. At larger *Tl*-content (100:1) only βHgS has been formed. In 1000 : 1 = Hg : Tl system at 75° – 100°C αHgS has also appeared, similarly to the $HgCl_2 - H_2S$ system:

100 : 1

25°C =	black	βHgS	pH = 1.30
50°C =	black	βHgS	pH = 1.31
75°C =	black	βHgS	pH = 1.35
100°C =	black	βHgS	pH = 1.25

1000 : 1

25°C =	black	βHgS	pH = 1.30
50°C =	black	βHgS	pH = 1.30
75°C =	black	β>αHgS	pH = 1.29
100°C =	black	β>αHgS	pH = 1.20

$\gamma Hg_3S_2Cl_2$ as associated phase has appeared only at 100°C in the 1000 : 1 system. In other cases only HgS has been crystallised. The chlorine content

* Δ = 0.48 Å at Whittaker – Muntus (1970)

of the crystalline phases is averaging at 0.11%, in few cases 0.05% or less has been analysed. From all Hg-solution-vapor systems studied the HgS phases of the $HgCl_{2(aq)} - TlCl_{(aq)}$ system showed the highest deficiency in *Hg* and *S*, though Hg : S ratio is more permanent in this system than in ohters.

Maximum *Hg*-content has been recorded in sulphide phases at 75°C. in both systems (100 : 1 and 1000 : 1).
The Hg : S ratio is the closest to stochiometric ratios in this case. Analyses are summerised in Fig. 15.

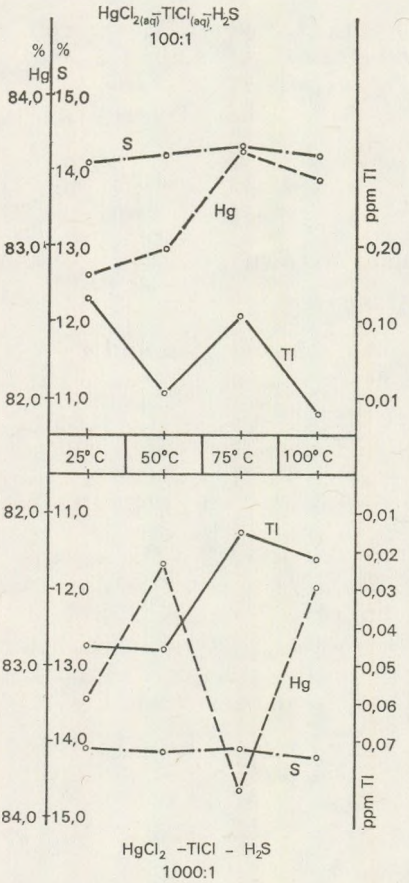

Fig. 15. Analysis data of the phases from $HgCl_{2(aq)} - TlCl_{(aq)} - H_2S$ systems

The crystalline phases show *Hg* deficiency and *S* surplus with permanent difference. (Table IV).

The average of analysis data:

100 : 1 = 83.24% *Hg*, 14.25% *S* 800 ppm *Tl*
1000 : 1 = 25° — 50° = 82.80% *Hg*, 14.12% *S*, 460 ppm *Tl*
= 75° — 1000° = 83.17% *Hg*, 14.51% *S*, 180 ppm *Tl*

wich is equal to:

100 : 1 = — 3.47% *Hg*, +3.34% *S*
1000 : 1 = 25° — 50°C = —3.99% *Hg* + 2.32% *S*
75 — 1000°C = —3.02% *Hg* + 2.68% *S*

deficiency and surplus.

The cell-parameter of βHgS phase is averagely larger than the literature data in the second decimal. As smallest a_0 values have been obtained with *As*, the largest ones with *Tl*, it is suggested that cell-deformation effect of ionic radii $Tl > Sb > As$, have been responsible for theses differences in case of ionic bonds:

100 : 1 = βHgS = a_0 = 5.8627 Å —800 ppm *Tl*
1000 : 1 = βHgS = a_0 = 5.8506 Å —460 ppm *Tl*

The variation of a_0 values is shown in Fig. 16.

4.6 $HgS_{(aq)} - TlCl_{(aq)} - 100 : 1$

During the experiments mixed $\beta > \alpha$ and $\alpha > \beta$ HgS phases have been formed in wide temperature interval (150° — 250°C):

a) 25° — 125°C = βHgS pH = 4.56 — 2.56 (black)
b) 150° — 200°C = βHgS > α HgS pH = 2.65 — 2.52 (black)
c) 250°C = αHgS > β HgS pH = 2.50 (brownish-red)
d) 300° — 350°C = βHgS pH = 2.57 — 2.60 (purple).

With rising temperature the acidity of the solution is increasing, βHgS is converting to αHgS. The *Hg*-content of sulfide phases shows maximum 100° — 150°C and minimum at 200°C. (Fig. 17).

The *Tl* content is gradually decreasing with temperature, while the amount of *S* remains practically unchanged. (Table V and VI).
The average values of analysis data shown in Fig. 17.

a) 25° — 125°C = 84.33% *Hg*, 13.76% *S* 400 ppm *Tl*
b) 150° — 200°C = 84.55% *Hg*, 13.81% *S* 200 ppm *Tl*
c) 250°C = 83.64% *Hg*, 13.88% *S* 70 ppm *Tl*
d) 300° — 350°C = 84.01% *Hg*, 13.95% *S* 100 ppm *Tl*

wich are equal to:

a) 25° — 125°C = —2.16% *Hg* —0.53% *S*
b) 150° — 200°C = —1.91% *Hg* +0.04% *S* (*)
c) 200°C = —1.91% *Hg* +0,04% *S* (*)
d) 300° — 350°C = —2.55% *Hg* +1.08% *S*

* based on one analysis only

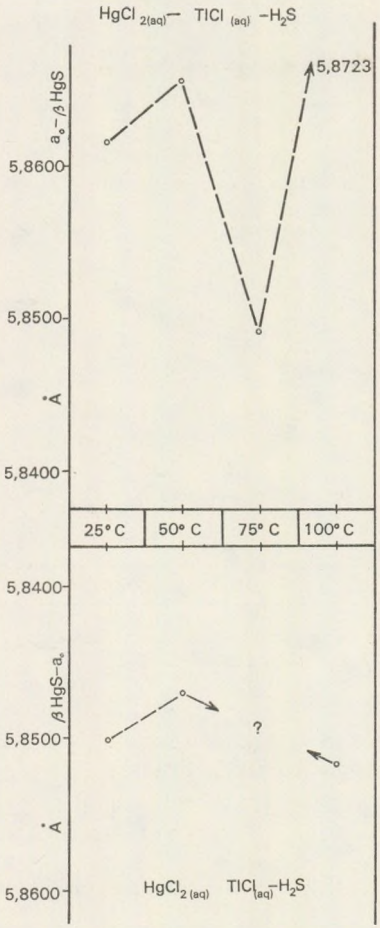

Fig. 16. Variation of cell-parameters in $HgCl_{2(aq)} - TlCl_{(aq)} - H_2S$

These data indicated as temperature was increasing (150° – 200°), the difference in *Hg* : *S* becoming smaller, then after αHgS became dominant, the difference was again larger (Table V.).

The cell-parameters of βHgS has been the largest among the systems studied:

a) 25° – 125°C = a_0 = 5.8646 Å – 400 ppm *Tl*
b) 150° – 200°C = a_0 = 5.8614 Å – 200 ppm *Tl*
c) 250°C = a_0 = 5.8613 Å – 70 ppm *Tl*

With rising temperature the a_0 values are decreasing along with the *Tl* content.

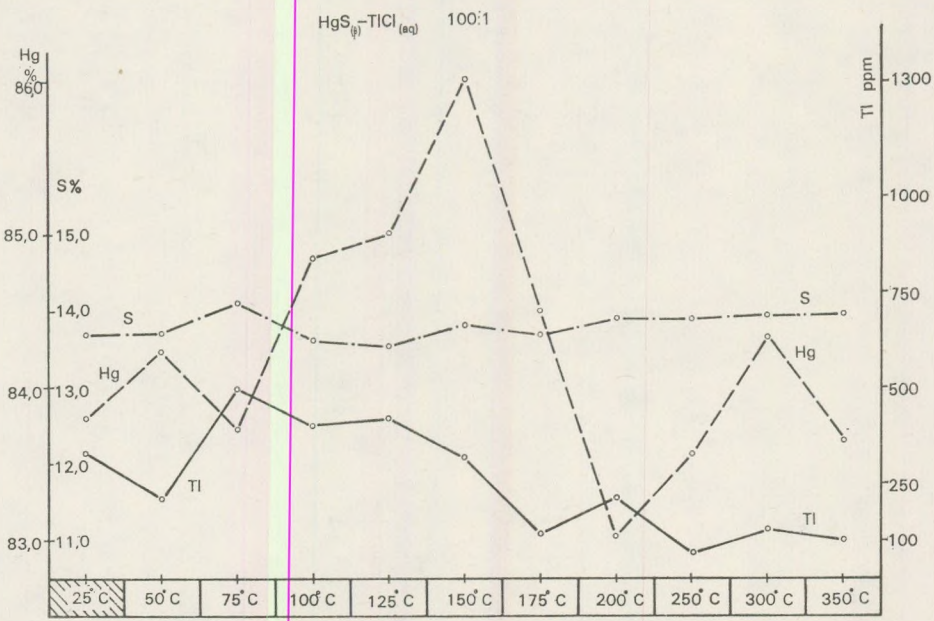

Fig. 17. Analysis data of crystalline phases of the $HgS_{(s)} - TlCl_{(aq)}$ system as a function of T°

The a_0 and c_0 parameters of αHgS are larger then literature data (= 2.91 Å), and indicate sligt elongation in c_0 direction:

150°C – HgS, c_0/a_0 = *2.305*; 175°C = *2.298*; 200°C = *2.295* Å
250°C – HgS, c_0/a_0 = *2.292*; 300°C = *2.287*; *350*°C = *2.286* Å

The variations of βHgS and αHgS cell parameters are shown in Fig. 18.

5. Conclusions

The experiments have provided new explanations for the conditions of formation of βHgS and αHgS and the crystal-chemical mechanism of their conversion. The following problems had to be answered.

1. Why both modifications were usually formed in one paragenetical sequence, and which is the primarily precipitated mercury-sulfide, βHgS or αHgS.
2. Is the βHgS of shalerite-type structure the more metastabile variety ?
3. Is there any possibility for conversion of cinnabar to metacinnabar below the temperature of the inversion point (344°C).
4. Which of the crystal-chemical data are caracteristic for βHgS and αHgS phases.

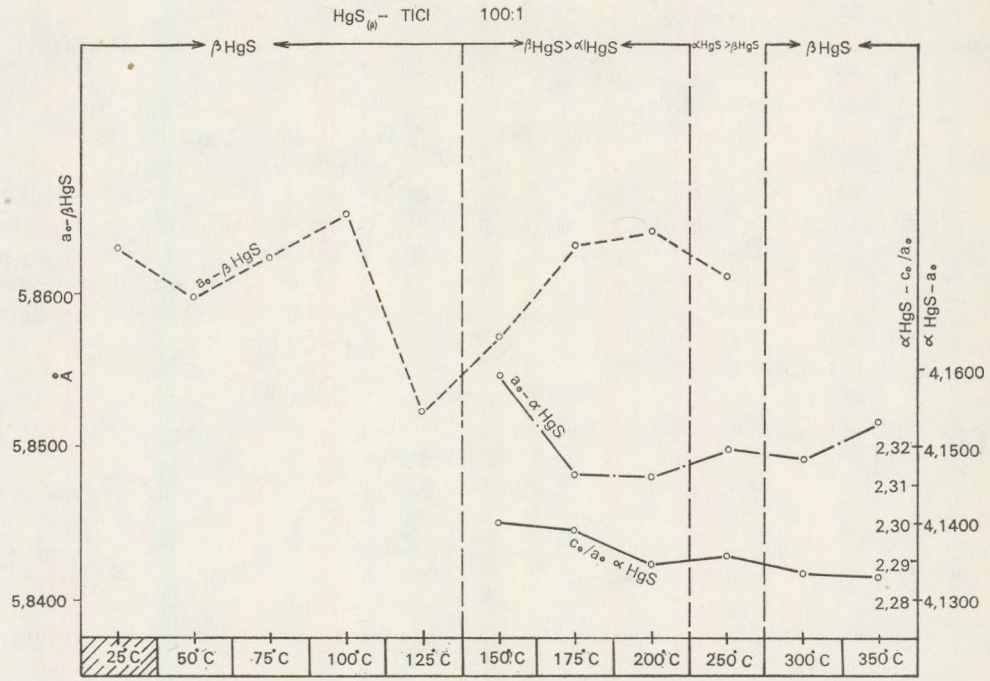

Fig. 18. Metacinnabar and cinnabar cell-parameters in the $HgS_{(s)} - TlCl_{(aq)}$-system as a function of T°

5. Is there any role of the *As, Sb, Tl* impurities applied in the experiments on the formation of βHgS and αHgS. Do they have any effect on the cell-parameters ?

6. What are the preconditions of alteration of βHgS to αHgS at room temperature. The aqueons media or the Na_2S solution in wich βHgS has higher solubility is the more favourable solvent for this alteration ?

This questions have been remained in most part unanswered in the previons literature of Hg-sulphide mineralization.

a) Between 25° – 75°C. The mercury, mobilized in form of complexes by chloride the most abundant anion of hydrothermal solutions crystallises as βHgS of sphalerite-type structure. The coexistent crystallistion of βHgS and αHgS in the temperature range of 75° – 100°C indicates that the formation of the more stable cinnabar-structure dies not begin at room temperatures. In the 75° – 100°C experiments only βHgS had been produced in the first short intervals, i.e. 15 – 60 min. Only initial crystallites of αHgS has developed in the 8-hours experiments, as evidencenced by the presence of the most intense 3.59 d/Å line and 1.735 d/Å doublet close to the 1.764 d/Å line of metacinnabar on the X-ray diffractograms.

From mercury (I)-nitrate solutions however αHgS, cinnabar has been formed at 25° – 50°C, suggesting that the orbital character of the Hg/I/-nitrate complex has governing effect on the development of structural type of mercury-sulfide.

In the experiments with $HgNO_{3(aq)} - H_2S$ at 75° – 100°C abrupt changes have been recorded in the proportion of mercury-sulfide polymorphs (= βHgS > αHgS). The test had been repeated at 65°C and similar βHgS > αHgS ratio has been obtained. In nitrate-containing solution vapor systems the inversion point can be positioned in 50 – 65°C temperature range, in which mixed phases, βHgS > αHgS are crystallising, after αHgS was formed betwen 25° – 50°C. In the case of nitrate-containing hydrothermal solutions the cinnabar and not the metacinnabar crystallises primarily below 50°C.

b) The As^{3+} ions in solution-vapor hydrothermal systems (at 25° – 100°C) prevent formation of αHgS, while in cases of presence of Sb^{3+} and Tl^{+} mono-phase βHgS has formed betwen 25° – 50°C, and βHgS > > αHgS polyphases at 75° – 100°C, similarly to the $HgCl_2 - H_2S$ system.

c) The experiments showed that the first crystallites, formed from solution-vapor systems, have always, βHgS structure initially, then in presence of nitrate ions, these rapidly (5 – 6 hours) alter to αHgS, wich is stabile below 60°C. In case of excess chloride-content, metacinnabar is formed below 50°C, above this temperature coexisting αHgS is also present. βHgS : αHgS ratio is 4 : 1.

d) Hg-depleted sulfide-phases are formed from solution-gas system, which become structurally ordered in solid-liquid (HgS + metal-containing solutions) systems. The *Hg*-deficiency is larger in phases of metacinnabar structure, the *Hg* : *S* ratios show greater differences then in phases of cinnabarstructure. In solid-phase – solution systems the *Hg* : *S* values are closer to the theoretical 1 : 1 ratio. This is most apparent for the cinnabar.

e) The recrystallisation of metacinnabar in solutions starts at room-temperature (30 days), through transitional mixed phases (αHgS > βHgS) with cinnabar dominance at 175°C and to final mono-phase system at 300°C.

f) In the $HgS_{(s)}$-$Na_2S_{(s)}$ system at 100°C mono-phase αHgS is produced. Its formation begins at room temperature.

g) The metacinnabar to cinnabar alterations in Na_2S are stimulated by the presence of antimony (Sb^{3+}) ions. The alteration begins at 125°C.

h) In $HgS_{(s)} - SbCl_{3(aq)}$ systems large (few millimeters in size) crystals have formed.

i) At our experimental conditions alteration of cinnabar to metacinnabar has *not* been recorded. In close system this alteration takes place at 344°C. At present there are no observations for alteration of cinnabar to metacinnabar during termometamorphosis.

j) In natural environment for the primary formation of metacinnabar chloridic hydrothermal solutions bave been proved to be the most favorable with As^{3+} content below 100°C, Tl^{+} content below 25°C, Sb^{3+} content below 50°C. The metacinnabar to cinnabar alteration may take place by

post-ore hydrothermal effects depending on temperature and ion-concentration of the solution, and possibly follows one of these schematic processes:

I. $HgS + H_2O$

a) 25°–150°C = βHgS > αHgS
b) 175°–250°C = αHgS > βHgS
c) 300°C = αHgS

II. $HgS + Na_2S + H_2O$

a) 25°– 50°C = βHgS > αHgS
b) 75°C = αHgS > βHgS
c) 100°–350°C = αHgS

III. $HgS + AsCl_3 + H_2O$

a) 25°–150°C = βHgS,
b) 175°C = βHgS > αHgS
c) 200°–250°C = αHgS > βHgS,
d) 300°C = αHgS

IV. $HgS + SbCl_3 + H_2O$

a) 25°–100°C = βHgS
b) 125°–150°C = βHgS > αHgS,
c) 175°–200°C = αHgS > βHgS
d) 250°–300°C = αHgS

V. $HgS + TlCl + H_2O$

a) 25°–125°C = βHgS,
b) 150°–200°C = βHgS > αHgS,
c) 250°C = αHgS > βHgS,
d) 300°–350°C = αHgS.

PLATE 1

1

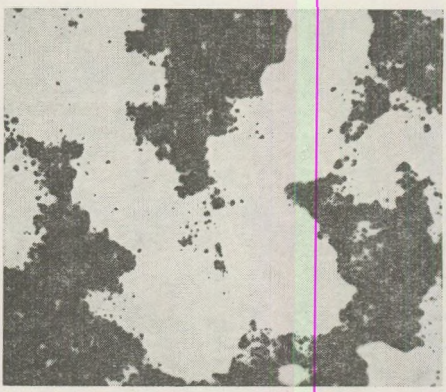

2

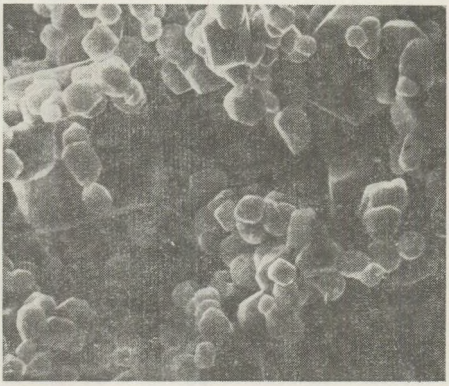

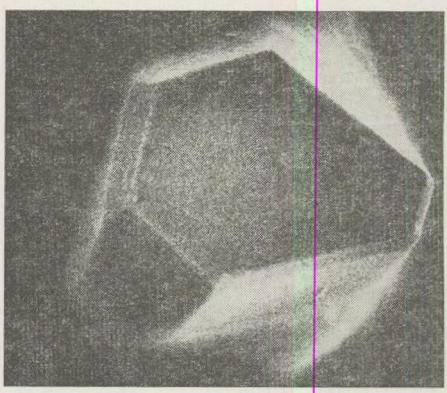

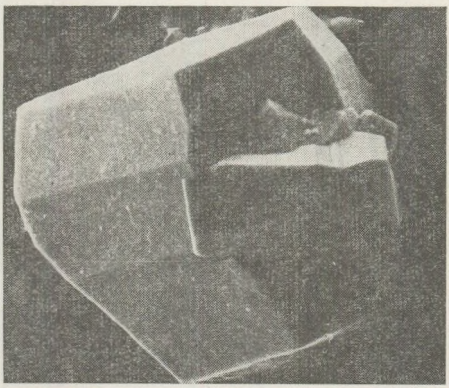

3

4

1 = $HgCl_2 + H_2O + H_2S - 50°C$
Aggregates of square-like crystal grains of Metacinnabar 120×.

2 = $Metacinnabar + Na_2S + H_2O - 300°C$
Sub hexaedric, isometric grains of cinnabar with (0001) base plaines; 10,000x, electronicrograph.

3 = $Metacinnabar + As(III)Cl + H_2O - 250°C$.
Idiomorphic cinnabar with (0001), (h0kl), (0hkl), and (1010) forms; 20 000x, electronmicrograph.

4 = $Metacinnabar + As(III)Cl + H_2O - 300°C$
Idiomorphic cinnabar with different proto- and deutero rombohedra and base-planes; Twin-intergrowth. 3000 x; electronmicrograph.

PLATE 2

5

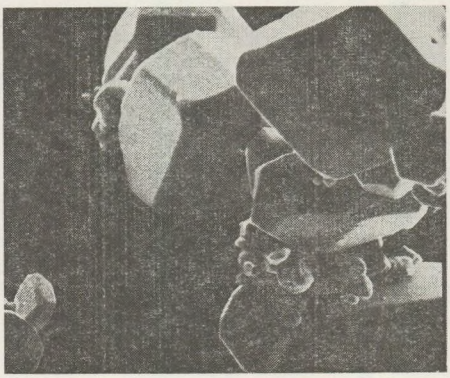

6

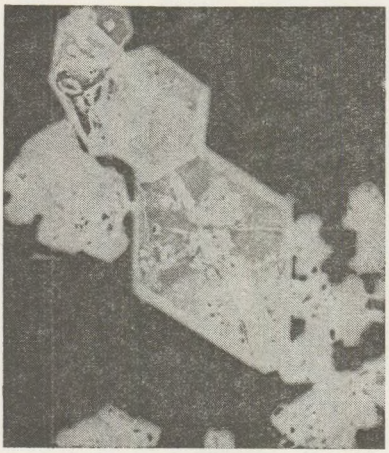

7

5 = *Metacinnabar + Sb(III)Cl + H_2O – 300°C.*
Idiomorphic cinnabar (0001), (1010) planes. 3000x; electronmicrograph.

6 = *Metacinnabar + Sb(III)Cl + H_2O – 250°C.*
Powder-preparatum. cinnabar crystals (=0,5 mm) with crystal-growth characteristics; 80 x.

7 = *Metacinnabar + Sb(III)Cl + H_2O – 300°C.*
Powder-praparatum. cinnabar crystals (=0,5 mm) with crystal-growth characteristics; 80 x.

REFERENCES

Barnes, H. L. et al. 1967: Ore solution chemistry II. etc. Econ. Geol. Vol. 62. p. 957 – 982.

Cruceanu, E. et al. 1969: Crystal growth of HgS from Hg-rich solutions. Journ. Cryst. Growth (5); p. 206.

Dickson, F. W., 1964: Solubility of cinnabar in Na_2S solutions at 50 – 250 °C and 1 – 1800 bars etc. Econ. Geol. Vol. 59. p. 625 – 635.

Dickson, F. W. – Tunnel, G. 1958: Equilibra of red HgS and black HgS etc. Am. Journ. Sci. (256), p. 654.

Dickson, F. W. 1959: The solubility relations of cinnabar and metacinnabar. The Am. Min. (44); p. 475.

Dreyer, R. M. 1940: The geochemistry of quecksilber mineralization. Econ. Geol. Vol. 35; p. 17 – 48.

Garner, R. W. et al. 1970: Growth of cinnabar from sodium sulfide. Journ. Cryst. Growth (7); p. 343 – 347.

Krauskopf, K. B. 1951: Physical chemistry of quecksilber transportation in vein fluids. Econ. Geol. Vol. 46; p. 498 – 522.

Ozerova, N. A. et al. 1969: Mercury mineralization at the Mendelyev Volcano. Dokl. Ak. Sci. USSR. Earth Sci. Sect. – 187); p. 652.

Pajachovska, A. 1970: Hydrothermal crystallization of cinnabar Journ. Cryst. Growth (7); p. 93 – 96.

Piotrovskii, G. L. 1961: One problem of genesis of cinnabar and metacinnabar. Int. Geo. Review (3); p. 652 – 657.

Protodiakonova, Z. M. et al. 1971: O nekotorich modifikaciah sulfida ruti etc. Zap. Vsesoyuzn. Min. Obsc. C. 100; Vol. 6. p. 731 – 738.

Saukov, A. A. 1973: Geochemie. VEB Verlag, Berlin.

Schwarzenbach, S. – Widmer, M. 1963: Die Löslichkeit von Metasulfiden I. etc. Helv. Chim. Acta. Vol. 46; p. 2613 – 2628.

Thompson, G. A. 1954: Transportation and deposition quicksilver ores in the Terlingua, Texas. Econ. Geol. Vol. 49; p. 175 – 197.

Tunell, G. 1964: Chemical processes in the formation of mercury ores etc. Geochem. et Cosm. Acta. Vol. 28; p. 1019 – 1037.

Vasilyev, V. I. et al. 1969: A new mercury-bearing species of sphalerite. Dokl. Acad. Sci. USSR. Earth Sci. Sect. (137); p. 137 – 139.

White, D. S. 1967: Mercury and base metal deposits etc. Geochem. Hydr. Ore Dep. (H. L. Barnes), New York, p. 575 – 631.

Kiss, J. 1975: Crystallochemical and metallogenetic investigation and evaluation of hydrothermal crystal phase model experiments (25° to 300 °C). Acta Geol. Ac. Scient. Hung. Tomus 19 (3 – 4), pp. 265 – 274.

INVESTIGATION OF HUNGARIAN SULFIDE ORES OF VARIOUS ORIGIN BY MEANS OF ACTIVATION ANALYSIS

J. BÉRCZI and J. KISS

Department of Mineralogy, Eötvös University, Budapest

Received: 15 May 1977

SUMMARY

It can be stated on the whole that the standard deviation of the results of measurements around the average varies according to samples and elements. The accuracy of activation measurements equals in general that of the traditional analytical methods or even surpasses it in certain cases. In case of some elements of ore minerals we can state that the demands (concerning sensitivity, accuracy, serial feasibility, economy etc.) determining the choice of analytical methods and the value of the obtainable informations *underline the advantages of the neutron activation method*, e. g. in case of Se, Ag, As, Sb, Co, La.

Part of the traditional methods requires in the case of the above mentioned elements more intricate sample preparatory, wet chemical (eventually separational) processes and assures the same or even less reproducibility (wet chemical analysis, spectrophotometry, atomic absorption), or *provides not so many informations* (e. g. spectroscopy, mass – spectrometry, *X*-ray fluorescence analysis). We may note that our analyses concerning the elements mentioned above are comparable with earlier analyses and in some a good conformity can be found.

We hope for further possibilites in extending the number of measurable elements especially concerning elements furnishing isotopes of shorter half-life (e. g. Ga, In, Mo, Re, Mn, Cl) as well as lanthanides (these latter as obtained from skarnic concentrates).

Applying epithermic activation the determination of e. g. Ni, Th and U becomes possible, further on the sensitivity and accuracy of Cd determination can be significantly increased.

Studies of this kind are going on, their results as well as interpretation of data will be dealt with in a later paper.

Introduction

Neutron activation analysis enables a sensitive and precise determination of many elements in geological samples too. Analysis of many siliceous rocks [Modern trends ..., 1969; Allen – Haskin – Anderson – Müller, 1970; Brunfelt – Steinnes (Eds), 1971), meteorites, lunar samples (Brunfelt – Steinnes, 1971; Levinson, 1970; Brunfelt – Steinnes – Sundroll, 1977] have been carried out, and as a result earlier Clark-distributions of some elements had to be corrected.

The extension of irradiations to the epithermic domain increased the number of determinable elements and in some cases also the sensitivity and accuracy of the determinations too (Steinnes, 1971; Randa, 1976).

The activation analysis turned to be a useful method of investigation of standard reference-materials, so of the study of minerals and rocks, first of all in the domain of trace concentrations, (Gordon – Randle – Goles – Corliss – Beeson – Oxley, 1968; Cojocaru – Ispas, 1971; Brätter – Lausch – Rösick, 1975).

Relatively few attention has been paid so far to a nondestructive multicomponent analysis of sulfide ores. At first Lamb et al. (1966) carried out such measurements by means of a Ge(Li) semiconductor detector, in the course of which determinations of elements furnishing isotopes of small and medium half-life have been made. Later on, Steinnes et al. (1973) and Randa (1976) carried out instrumental analyses of sulfides and ore concentrates.

The paper presents the results of nondestructive analyses carried out by means of neutron activation on "averaged" ores, monomineral fractions from the mineralization of Recsk serving for standardization purposes as well as on a few other ores of diffent composition, genesis and place of occurrence. The investigations have included first of all trace and secondary elements being important geochemically and practically, such as: Cu, Zn, Se, Ag, As, Cd, Sb, Co, Au, Sc, La.

Samples and standards

Samples under investigation can be grouped as follows:

I. Polimetallic and monomineral fractions of the mineralization of Recsk used as reference material (according to the numbering of Table II.):

1. Dispersed pyrite ore
2. Dispersed chalcopyrite-pyrite ore
3. Chalcopyrite-pyrite skarne-ore
4. Sphalerite-pyrite skarne-ore
5. Sphalerite-pyrite "metasomatic" ore
6. Polimetallic "metasomatic" ore
7. Sphalerite
8. Pyrite
9. Galenite, sphalerite, chalcopyrite
10. Chalcopyrite, pyrite

II. Other samples coming from the mineralization of Recsk:

11. Chalcopyrite, pyrite from skarn
12. Chalcopyrite, pyrite from skarn
18. Pyrite from skarn
20. Enargite
21. Luzonite
24. Skarnic vein
25. Skarnic vein
26. Skarnic vein

III. Monomineralic fractions from various Hungarian finding places:

13. Chalcopyrite, pyrite, Gyöngyösoroszi
14. Chalcopyrite, pyrite, Rudabánya
15. Chalcopyrite, pyrite, Nagylápafő
19. Sphalerite, Nagylápafő
22. Galenite, Gyöngyösoroszi (flotationed ore)
23. Galenite, Nagybörzsöny.

IV. Samples from foreign finding places:

16. Chalcopyrite, pyrite, Texas Gulf, Canada
17. Chalcopyrite, pyrite, Vrly Brjag, Bulgaria.

For the quantitative determination solutions of p. a. or spectroscopic purity of the components were used.

Pretreatment of samples and standards for the irradiation

Quantities of the samples of about 100 mg (measured with analitical precision) were packed into small polyethylene boxes. In order to assure uniform measuring geometry, 100 μl quantities of the standard solution (measured by means of micropipette) were taken separately into similar boxes, then dropped into silica gel and dryed out using an infra lamp.

According to earlier observations the boxes contained the elements sought for under the limit of detectability, so that before the measurements a repacking became unnecessary.

Irradiation, measurements

Irradiation of the samples took place in the Training Reactor of the Technical University Budapest.

For Cu-determinations the pneumatic irradiation system of the reactor ($\varphi_{\text{term}} = 2{,}8 \times 10^{11} n\ \text{cm}^{-2}s^{-1}$), for the production of isotopes of longer half-life one of the vertical irradiation channels) $\varphi_{\text{term}} = 2{,}4 \times 10^{11} n\ \text{cm}^{-2}s^{-1}$) were used.

In case of irradiation by the pneumatic system times of 20 min, for channel irradiation times of 24 hours were applied.

Simultaneously with the samples and standards also copper flux-monitors were irradiated.

Measurements have taken place in case of the short time irradiations after 2 – 3 hours, while for the long time irradiations delays of 5 days and 3 months were applied.

For the measurements a semiconductor detector "Princeton Gamma Technique Ge (Li) and joint KFKI made 4096 channel analyser was used. The resolution of the detector was 2.2 keV related to the 1332 keV peak of ^{60}Co.

Table I.

Nuclear parameters of the elements investigated and conditions of measurements

Element	Isotope used for the determination	Abundance (%) *	Cross section (barn)*	Nuclear reaction	Gamma-energy of the „analytic peak" (keV)**	Half-life*	Irradiation time (hours)	Cooling time (days)	Measuring time (sec)
Sc	^{45}Sc	100	13	^{45}Sc (n, γ) ^{46}Sc	889,4; 1120,3	83,9 days	24	90	2000
Co	^{59}Co	100	17	^{59}Co (n, γ) ^{60}Co	1173,1; 1332,4	5,24 years	24	90	2000
Cu	^{63}Cu	69,1	4,5	^{63}Cu (n, γ) ^{64}Cu	511 ; 1345,5	12,8 hours	20	0,1	200
Zn	^{64}Zn	48,49	0,82	^{64}Zn (n, γ) ^{65}Zn	1115,4	234 days	24	90	2000
As	^{75}As	100	4,30	^{75}As (n, γ) ^{76}As	559,2	26,3 hours	24	5	2000
Se	^{74}Se	0,87	30	^{74}Se (n, γ) ^{75}Se	264,6; 279,6	121 days	24	90	2000
Ag	^{109}Ag	48,65	4,2	^{109}Ag (n, γ) ^{110m}Ag	675,8; 937,2	253 days	24	90	2000
Cd	^{114}Cd	28,86	0,30	^{114}Cd (n, γ) ^{115}Cd	492,5; 527,7	2,3 days	24	5	200
Sb	^{121}Sb	57,25	6,2	^{121}Sb (n, γ) ^{122}Sb	564,0	2,75 days	24	5	2000
	^{123}Sb	42,75	3,4	^{123}Sb (n, γ) ^{124}Sb	62,6; 1690,7	60,9 days		90	
La	^{139}La	99,911	8,8	^{139}La (n, γ) ^{140}La	159,954	40,27 hours	24	5	2000
Au	^{197}Au	100	98,8	^{197}Au (n, γ) ^{198}Au	411,8	2,70 days	24	5	2000

* *E. Bujdosó, I. Fehér, G. Kardos:* Activation and Decay Tables of Radioisotopes. Akadémiai Kiadó, 1973.

** *F. Adams, R. Dams:* A compilation of precisely determined gamma-transition energies of radionuclides produced by reactor irradiation. J Radioanal. Chem. 3 (1969) 99—125.

For both samples and for both positions two parallel irradiations have been carried out, so we obtained for the elements furnishing radioisotopes of short half-life at least 2, for those with longer half-life 2 or 4 parallel data. (Several usable peaks, – e. g. in case of La, Cu, or several radioisotopes of various halflives such as ^{122}Sb, ^{124}Sb – even accordingly more). Irradiational, cooling and measurement parameters as well as the most important physical constants of the radioisotopes used are contained in Table I.

Computation of the results of measurements

Spectra recorded on punch tape have been analysed by the computer RAZDAN – 3 of the Computer Center of the University. Besides the complete list of spectra the programm used contains the following data of higher importance:

- the place of the peak (the serial number of the channel),
- the value of gamma-energy belonging to the given channel number,
- the area of the peak,
- the statistical error of the area of the peak,
- the statistical error in percent of the peak area.

In addition the programm determines in parts of the spectrum chosen in advance the volume of peak area still usable – in the given domain (in case of a given background) – for quantitative measurements or for detection of an isotope (Currie-levels, C u r r i e, 1968). So we were able to give the lower concentration limit of the determinability also in cases, when the method was not sufficiently sensitive for a quantitative evaluation.

Given the knowledge of peak areas we computed corrections for uniform irradiation – cooling – and measuring time intervals, for uniform neutron flux, geometric measuring positions as well as for standards and for the samples investigated. Calculations were carried out on the desktop calculator, type: Hewlett – Packard 9810 of the Institute of Mineralogy of the University.

Gamma-spectra of some mineral fractions (pyrite, chalcopyrite, sphalerite, galenite) are shown on Figs. 1, 2, 3 and 4.

Summary of the results of measurements

Results of measurements are assembled in Table 2. Mean concentrations are shown as well as single standard deviations computed on the basis of parallel measurements are given expressed in the same units as the mean concentrations. When needed also detection limits computed on the base of Currie levels are given.

Copper. Measuring accuracy – besides simplicity and quickness – is comparable to that of conventional (electrogravimetric, photometric) methods, depending on concentration and

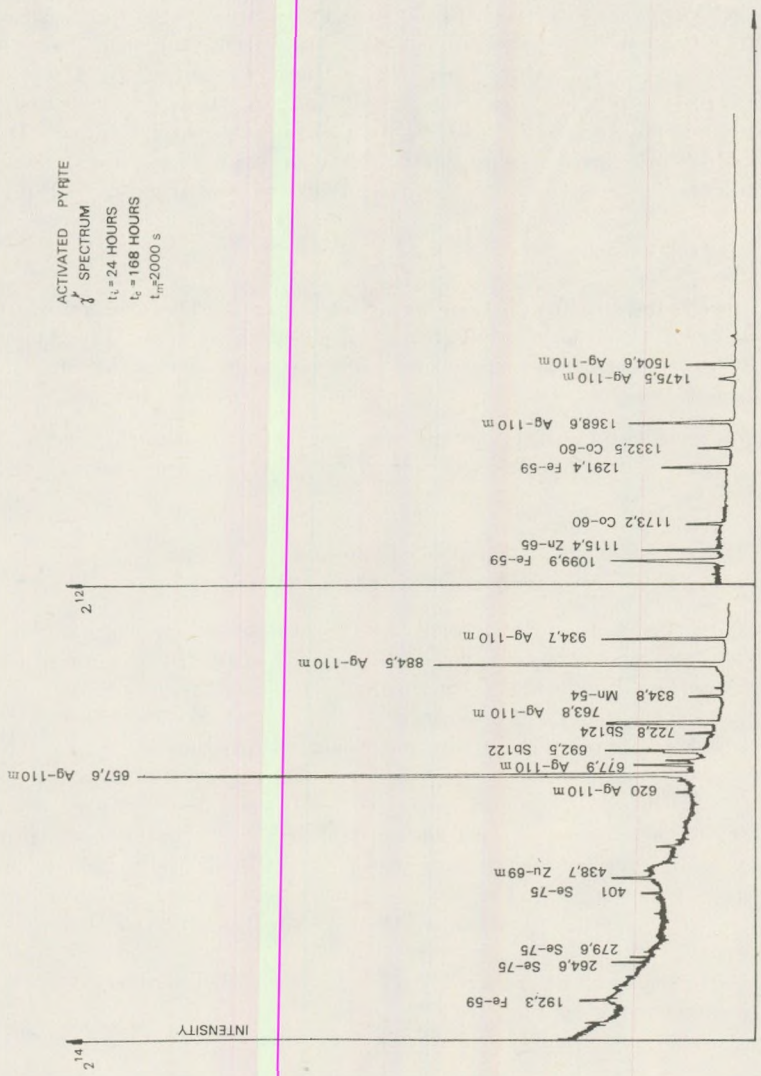

Fig. 1. Gamma-spectrum of activated pyrite (irradiation time: 24 hours, cooling time: 168 hours, measuring time: 2000 sec)

matrix material: 0.2% (relative) (29.28% Cu) – 15% (0.02% Cu). In case of multicomponent serial measurements the method can be proposed as a method for the determination of macro respectively accesoric component.

Zinc: Lower limit of quantitative evaluability (for the measuring parameters) is about 0.008%. Measuring accuracy: 0.7% (65.03% Zn) – 17% (0.123% Zn). As regards applicability of the method the conditions are the same as given above with copper.

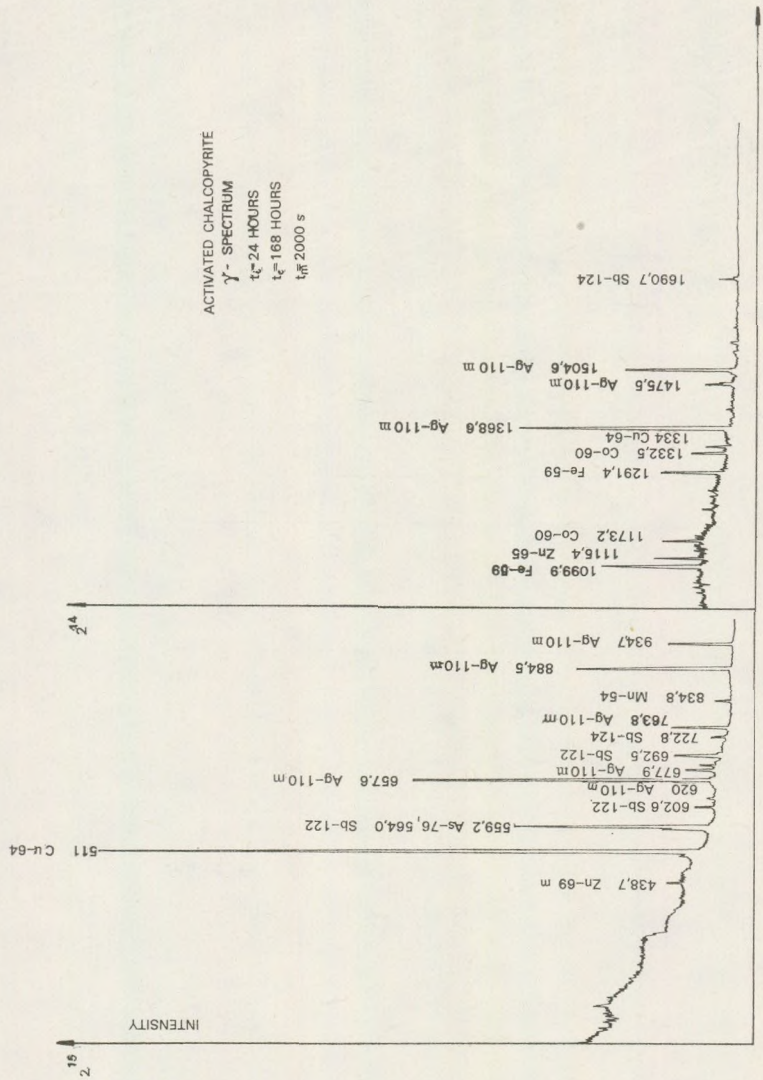

Fig. 2. Gamma-spectrum of activated chalcopyrite (irradiation time: 24 hours, ccooling time: 168 hours, measuring time: 2000 sec)

Selenium: Measuring accuracy: 2% (3397 ppm Se) −21% (14 ppm Se). Selenium is one of the elements measurable with high sensitivity and accuracy (when needed the parameter can be significantly increased by changing of measuring conditions). It is recommended for quick and nondestructive trace analyses.

Silver: Lower limit of quantitative measureability is 4 ppm. By means of increase of irradiation, measuring and cooling

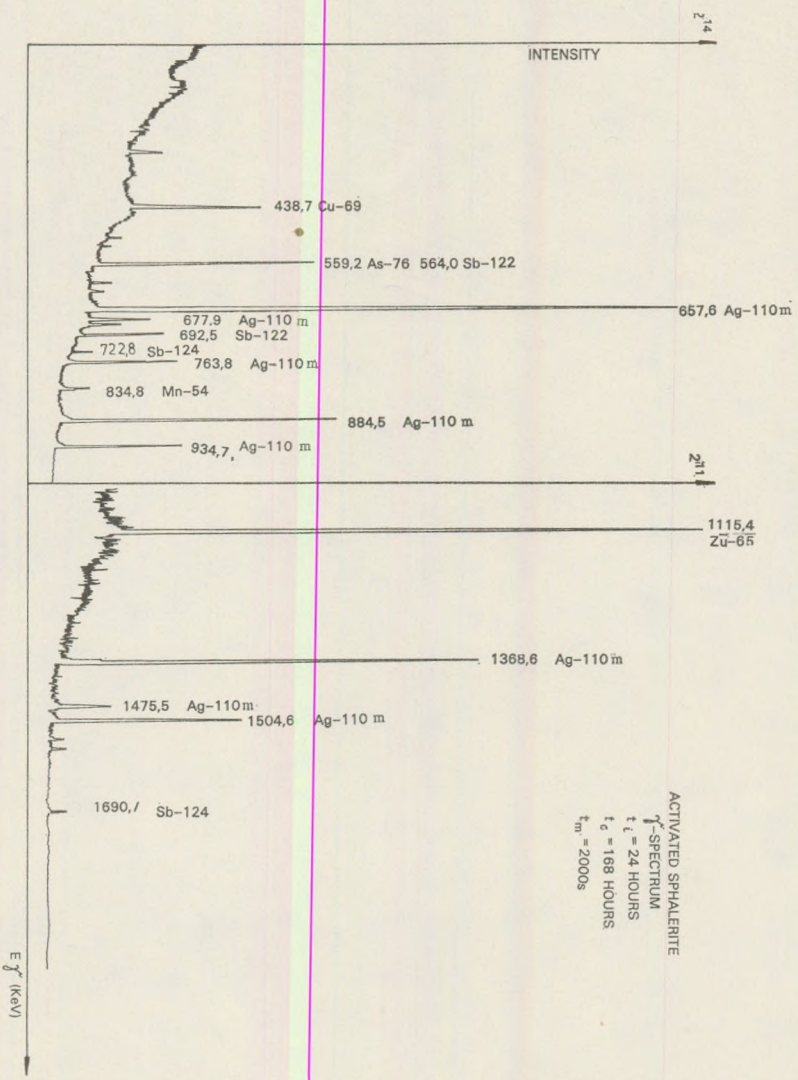

Fig. 3. Gamma spectrum of activated sphalerite (irradiation time: 24 hours, cooling time: 168 hours, measuring time: 2000 sec)

times, sensitivity and accuracy can be increased. Measuring accuracy: 6.5% (368 ppm Ag) —40% (4.4 ppm Ag).

Arsenic. It is an element with precise determinability. In case of nondestructive measurement with the presence of antimony of higher quantity application of correction is needed. Measuring accuracy: 0.6% (3616 ppm As) —11,8% (17 ppm As).

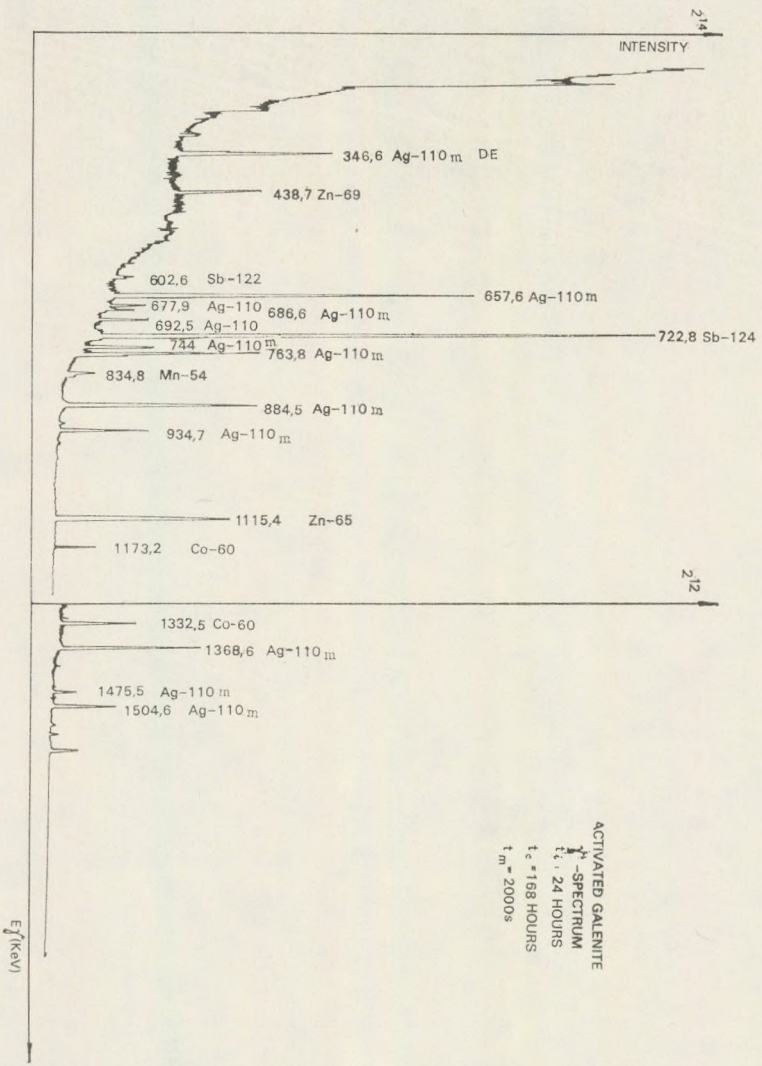

Fig. 4. Gamma-spectrum of activated galenite (irradiation time: 24 hours, cooling time: 168 hours, measuring time: 2000 sec)

Cadmium: On account of significant background interference it can be measured only with moderate accuracy and sensitivity. Lower limit of valuability is about 15 ppm.
Measuring accuracy: 0.9% (6363 ppm Cd) −48% (23 ppm Cd).

Antimony: It can be measured without destruction sensitively and precisely. In case of the parameters applied the measuring accuracy is: 0.8% (5857 ppm Sb) −25% (0,8 ppm Sb).

Cobalt: It can be measured simply, precisely and sensitively from any matrix material.
Measuring accuracy: 3.3% (264 ppm Co) —45% (3 ppm Co), limit of detectability about 1 ppm.

Gold: It can be measured with extremely high sensitivity and accuracy. Its determination is not influenced by other elements. Measuring accuracy: 8.6% (837 ppm Au) —20% (0.1 ppm Au).

Scandium: Owing to its favourable nuclear parameters its determination can be made from any mineral or rock sensitively and precisely Limit of detectability is about 2 ppm Sc.
Measuring accuracy: 5% (21 ppm Sc) —20% (5.5 ppm Sc).

Lanthanum. Remarks made for scandium are valid here too. Lanthanides are — with a few exceptions — well measurable by

Summary of results

		Cu %	Zn %	Se ppm	Ag ppm
1 1739/71	Disseminated pyrite ore	0,59 ± 0,09	< 0,008	23 ± 6	< 5
2 1742/71	Disserminated chalcopyrite-pyrite ore	1,35 ± 0,19	0,09 ± 0,01	26 ± 10	5 ± 2
3 1740/71	Chalcopyrite-pyrite skarne-ore	3,19 ± 0,26	0,023 ± 0,004	155 ± 21	∅ 5
4 1741/71	Sphalerite-pyrite skarne-ore	0,26 ± 0,01	6,94 ± 0,08	742 ± 37	36 ± 8
5 1743/71	Sphalerite-pyrite „metasomatic" ore	0,45 ± 0,01	6,11 ± 0,12	55 ± 11	< 5
6 1744/71	Polymetallic „metasomatic" ore	6,60 ± 0,11	9,86 ± 0,20	271 ± 31	38 ± 12
7 2634/1	ZnS	0,43 ± 0,03	65,03 ± 0,40	127 ± g2	84 ± 22
8 2634/3	FeS_2	0,26 ± 0,02	0,46 ± 0,03	325 ± 29	< 5
9 2634/6	PbS < ZnS < $CuFeS_2$	4,32 ± 0,12	9,98 ± 0,12	3397 ± 68	368 ± 24
10 2634/22	$CuFeS_2$ < FeS_2	29,28 ± 0,04	0,25 ± 0,02	981 ± 40	34 ± 6
11	Recsk RM — 35, $CuFeS_2$ < FeS_2	11,85 ± 0,03	0,001	575 ± 131	25 η ± 3
12	Recsk RM — 32, $CuFeS_2$ < FeS_2	11,34 ± 0,30	0,001	899 ± 115	69 ± 5

means of neutron activation method. Measurability limit: about 4 ppm.
Measuring accuracy: 6% (245 ppm La) −20% (5 ppm La).

In case of samples 20. and 21. (enargite, respectively luzonite) the background activity of As and Sb – being present as main components – is so high that determination of Cu and Cd is not possible, while the quantity of As is not comparable with the As content of the standard. Thus, their place has been left blank in the table.

Acknowledgements

We are indebted to Dr. T. Zelenka (National Ore-and Mineral Mines for having made available part of the samples.

Table II.

of measurements

As ppm	Cd ppm	Sb ppm	Co ppm	Au ppm	Sc ppm	La ppm
626±10	<15	4±1	14±3	0,2±0,02	14±1	17±5
97±4 97±4	23±11	9±2	30±4	0,3±0,05	12±0,6	99±6
3616±21	20±8	8±2	23±5	0,6±0,1	8,5±0,5	245±15
868±26	<15	26±3	20±3	1,1±0,1	5,5±1,1	43±3
273±18	533±18	7±2,5	42±2	<0,1	21±1	95±4
1784±15	583±67	17±5	264±12	<0,1	<2	23±1
331±29	6363±61	245±11	3±1	0,1±0,02	<2	<4
1184±32	<15	8±2	16±2	0,6±0,06	<2	<4
39±3	915±36	24±4	10±2	<0,1	<2	<4
598±55	182±26	36±3	42±4	2,0±0,1	<2	5±1
17±2	57±6	0,8±0,2	70±7	4,7±0,1	<2	<4
90±3	144±13	3,9±0,2	116±1	1,7±0,1	<2	<4

(conti

		Cu %	Zn %	Se ppm	Ag ppm
13	Gyöngyösoroszi $CuFeS_2 < FeS_2$	16,06 ± 0,06	0,03 ± 0,001	1669 ± 53	394 ± 21
14	Rudabánya, $CuFeS_2 < FeS_2$	13,56 ± 0,05	0,001	14 ± 3	35 ± 3
15	Nagylápafő, $CuFeS_2 < FeS_2$	5,07 ± 0,03	0,30 ± 0,01	81 ± 5	63 ± 5
16	Texas Gulf, Canada $CuFeS_2 < FeS_2$	12,19 ± 0,05	0,56 ± 0,02	845 ± 12	71 ± 8
17	Vrly Brjag-Burgas, Bulgaria $CuFeS_2 < FeS_2$	7,86 ± 0,04	0,002 ± 0,001	77 ± 8	9 ± 1
18	Recsk RM – 35, FeS_2	0,53 ± 0,01	0,001	336	74 ± 12
19	Nagylápafő, ZnS	0,14 ± 0,02	62,33 ± 0,53	185 ± 14	251 ± 24
20	Recsk, enargite		0,10 ± 0,01	231 ± 8	586 ± 15
21	Recsk, luzonite		0,08 ± 0,01	1469 ± 70	42 ± 6
22	Gyöngyösoroszi PbS(flotated ore)	0,12 ± 0,01	0,16 ± 0,01	32 ± 4	9 ± 1
23	Nagybörzsöny, PbS	0,22 ± 0,02	0,04 ± 0,01	16 ± 2	227 ± 8
24	Recsk, RM – 35	0,02 ± 0,003	0,45 ± 0,08	< 10	< 5
25	Recsk, RM – 27 952 – 953 m	0,20 ± 0,01	0,28 ± 0,05	115 ± 10	28 ± 10
26	Recsk, RM – 30 649 – 649,5 m	0,02 ± 0,003	1,21 ± 0,06	< 10	93 ± 18

Table II.

nued)

As ppm	Cd ppm	Sb ppm	Co ppm	Au ppm	Sc ppm	La ppm
119±4	365±32	103±2	9±2	0,5±0,1	<2	<4
355±13	171±22	18±1	68±3	0,5±0,1	<2	<4
103±9	144±21	6,3±0,5	68±3	0,3±0,1	<2	<4
21±2	204±23	4,5±0,3	14±2	0,2±0,05	<2	<4
69±2	15	2,5±0,2	192±8	0,3±0,03	<2	<4
47±4	2466±370	156±5	1	0,1±0,025	<2	<4
		4670±40	12±1	540±43	<2	<4
		5857±45	12±1	837±72	<2	<4
246±29	138±12	2±0,5	8±1	0,4±0,1	<2	<4
3±0,3	233±34	1,7±0,2	39±6	0,2±0,05	<2	±4
4,4±1,8	59±6	5±0,5	8±4	0,05±0,02	10,8±1,4	28±2
5±2	48±5	5±0,4	18±5	0,4±0,04	13,2±1,4	17±1
139±4	173±13	6,3±0,4	8±3	0,03±0,04	32±1	771±8

REFERENCES

Allen, R. O., Haskin, L. A. Anderson, M. R., Müller, O., 1970: Neutron activation analysis for 39 elements in small or precious samples, Journal Radioanal. Chem. 6. pp. 115–137.

Brätter, P., Lausch, J., Rösick, U., 1975: Neutronenaktivierungsanalytische Multielementbestimmung in Carrara–Marmor und Kalksteinstandard KH, Z. Anal. Chem. 275., pp. 359–363.

Brunfelt, A. O., Steinnes E. (Eds.) 1971: Activation Analysis in Geochemistry and Cosmochemistry, Universitetsforlaget, Oslo.

Brunfelt, A. O. Steinnes, E., Sundroll, B., 1977: Application of a multi-element neutron activation scheme to the determination of 38 elements in the Allende meteorite, Radiochem. Radioanal. Letters 28. (2), pp. 181–189.

Cojocaru, V., Ispas, M. 1971: Instrumental neutron activation analysis of some new standard rocks /See in Ref. 3

Currie, L. A. 1968: Limits for qualitative detection and quantitative determination. Application to radiochemistry. Anal. Chem. 40. (33) pp. 586–593.

Gordon, G. E., Randle, K., Goles, G. G., Corliss, J. B., Beeson, M. H., Oxley, S. S. 1968: Instrumental activation analysis of standard rocks with high-resolution gamma-ray detectors, Geochim. Cosmochim. Acta 32. pp. 369–396.

Lamb, J. F., Prussin, S. G., Harris, J. A., Hollander, J. M., 1966: Application of lithium-drifted germanium gamma-ray detectors to NAA nondestructive analysis of a sulfide ore, Anal. Chem. 38. (7), pp. 813–818.

Levinson, A. A. (Ed.), 1970: Proceedings of the Apollo 11 Lunar Science Conference, Pergamon Press, London.

Modern Trends in Activation Analysis 1969: U. S. Government Printing Office, Washington D. C.

Randa, Z., 1976: Analytical possibilities of epithermal neutron activation in routine INAA of mineral materials, Radiochem. Radioanal. Letters 24. (3), pp. 157–168.

Steinnes, E., 1971: Epithermal neutron activation analysis of geological material (in Brunfel steinnes, 1971).

Steinnes, E., Mukherjee, A. D., 1973: Instrumental activation analysis of a sulfide ore and some ore benefication products, 7. Radioanal. Chem. 14., pp. 129–138.

Zelenka, T., 1973: Experiences of the investigations of ore standards II. National Rare Metal Conference, Pécs, V 1. 2., pp. 184–199.) (in Hungarian.)

TWIN LAW OF "BÖRZSÖNY" WITH MEASURABLE TWINNING — AND COMPOSITION — PLANE FROM HUNGARIAN ANDESITE

H. VINCZE SZEBERÉNYI

Mineralogical Department, Museum of Natural History, Budapest

Received: 22. December 1976

SUMMARY

Normal twin-laws according to (110) and (130) respectively according to the left forms of these could be established for the first time for plagioclase twin-crystal groups figuring as andesite porphyric phenocrysts (1974). Although these twin-laws could be established from the measured optical data by means of vectorgeometrical computations, no composition — respectively twinning — planes could be determined with them. The plagioclase twin crystal dealt with in what follows occurred in one of the andesite samples collected in the Visegrád mountains. With this twin complex the composition — and twinning — plane of the Börzsöny-twin-law, $(1\bar{1}0)$, between two twinned parts being in immediate contact could well be detected and measured. Values obtained with the measures are in good agreement with those obtained from computations, proving that normal twin laws according to (110) and (130), respectively according to their left forms can be present with plagioclases found in nature.

The andesite sample comes from the Dömörkapu quarry (Visegrád mountains). The rock is a medium- or dark -grey, fresh pyroxene andesite. Microscopically it contains microcavities the internal walls of which are lined at places by green nontronite. The texture of the pyroxene andesite is microhemicrystallic-porphyric. Its mineral components are: *plagioclase, ortho-and clino-pyroxene and opaque mineral.* The amount and crystallization degree of the matrix proves that it is an effusion rock and not a subvolcanic one. The porphyric components are: plagioclase, pyroxene; their dimension is: $150-1700\ \mu$. Between plagioclase and pyroxene many oriented intergrowths can be seen, and they appear sometimes as inclusions within each other.

The rock is containing so called "cognate inclusions" also, i.e. inclusions from the depth (gabbro, diabase).

On the evidence of the texture crystallization might have occurred in two magma chambers, but the solidification of the rock took place on the surface. Owing to the idiomorphic development of the porphyric phenocrysts it is probable that the formation had been stagnant in a magma-chamber of high temperature and the outflow took place afterwards.

In the crystallization process of plagioclases two generations can be observed. The bulk of plagioclase crystals is of zonal structure, but zoneless sections can also be encountered. The anorthite content of zonal plagioclases varies between 70 and 86%.

The plagioclases are of bladed, tabular habit according to the face (010). Twinned formations are very frequent, twin plates are rather wide. Among the crystal faces types (110) and ($1\bar{1}0$) can frequently be encountered. Besides cleavages (001) and (010) also cleavages according to (110) and ($1\bar{1}0$) are well measurable. Predomimant composition faces are: the most frequent plane is (010) and some irregular composition planes among the multi-composed twin formations are also relatively frequent.

Many crystal groups consisting of a number of twin complexes are present and their ratio as compared with that of "common" twins is high. The complicate complexes consisting of several twin members show sometimes a well observable matrix inclusion structure, which seems to be uniform as if it surrounded a common core.

This rock was the source of the plagioclase twin crystal on the thin section of which one can measure the left form of the "Börzsöny-twin-law", the ($1\bar{1}0$) face as composition and twin plane. The method of vector-geometrical computation for the interpretation of observed data of plagioclase twin crystals was discussed in an article of mine published in common with Mrs Örkényi – Bondor L. (1974).

Observed and computed data of the plagioclase twin crystal figuring in sample Sz. 2. are as follows:

Denotations used in the course of computation:

M_{I_0} = unit vector of the (010) face normal in the first complex,
M_{II_0} = unit vector of the (010) face normal in the second complex,
Z_{I-II_0} = unit vector of the [001] zone axis in the first and second complex,
$K_0 = \frac{\perp [001]}{(010)}$ = unit vector of the "roc-tourné" twin axis,
T_0 = unit vector of the ($1\bar{1}0$) face normal,
a_0 = unit vector of the direction of highest optical elasticity,
b_0 = unit vector of the direction of medium optical elasticity,
c_0 = unit vector of the direction of lowest optical elasticity.

The upper case letter figuring as index in the right lower corner of the letter denoting the vector represents the corresponding twin member. The apostrophe in the right upper corner denotes the transformed value of the vector. The marking (with letters) of the morphological directions agrees with the Goldschmidt marking system.

The measured data of the twin crystals shown in Fig. 1. are as follows:

I. = first complex containing the members A, B, C.

Its cleavage and twinning face is:

M_I = n = 113.5°, h = 17 7°.

II. = second complex containing the members D and E.

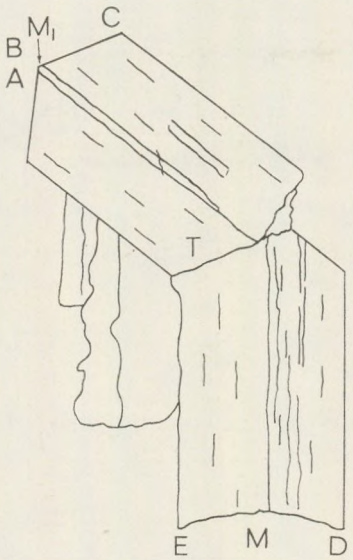

Fig. 1. Plagioclase twin crystal in andesite of Dömörkapu.

Its cleavage and twinning face according to (010) is:

$$M_{II} = \mathrm{n} = 237°,\ \mathrm{h} = 4.5°.$$

The $(1\bar{1}0)$ twinning and composition plane appearing between the two complexes is as follows:

$$T = \mathrm{n} = 177.5°,\ \mathrm{h} = 26°.$$

The $(1\bar{1}0)$ direction appears in either twin members in the form of growth lines, crystal faces and parting too.

The $(1\bar{1}0)$ direction of the two complexes is alternatively parallel to the (010) direction of the other complex.

$$M_{I_0} = -0.87340\,i - 0.37976\,j + 0.30486\,k$$

$$M_{II_0} = +0.83608\,i - 0.54295\,j + 0.37460\,k$$

$$T_0 = -0.04043\,i - 0.92629\,j + 0.37460\,k.$$

A twin-member:

$$\mathrm{n}_b = 234° \qquad \mathrm{h}_b = 3.5°$$

$$b_{A_0} = +0.80750\,i - 0.58668\,j + 0.06104\,k$$

$$\mathrm{n}_a = 326° \qquad \mathrm{h}_a = 30.5°$$

$$a_{A_0} = +0.48181\,i + 0.71431\,j + 0.50753\,k$$

$$c_{A_0} = [b_{A_0} \times a_{A_0}] = -0.34136\,i - 0.38042\,j + 0.85947\,k.$$

B twin-member:

$$n_b = 236.5^\circ \qquad h_b = 8.5^\circ$$
$$b_{B_0} = +0.82471\,i - 0.54586\,j + 0.14780\,k$$
$$n_c = 328^\circ \qquad h_c = 12^\circ$$
$$c_{B_0} = +0.51833\,i + 0.82950\,j + 0.20791\,k$$
$$a_{B_0} = [b_{B_0} \times c_{B_0}] = -0.23608\,i - 0.09485\,j + 0.96703\,k.$$

C twin-member:

$$n_b = 180.5^\circ \qquad h_b = 20^\circ$$
$$b_{C_0} = +0.00819\,i - 0.93965\,j + 0.34202\,k$$
$$n_c = 280^\circ \qquad h_c = 25^\circ$$
$$c_{C_0} = +0.89252\,i + 0.15737\,j + 0.42261\,k$$
$$a_{C_0} = [b_{C_0} \times c_{C_0}] = -0.45093\,i + 0.30180\,j + 0.83994\,k.$$

D twin-member:

$$n_b = 175^\circ \qquad n_b = 24.5^\circ$$
$$b_{D_0} = -0.07930\,i - 0.90649\,j + 0.41469\,k$$
$$n_c = 277^\circ \qquad n_c = 24.5^\circ$$
$$c_{D_0} = +0.90317\,i + 0.11089\,j + 0.41469\,k$$
$$a_{D_0} = [b_{D_0} \times c_{D_0}] = -0.42189\,i + 0.40742\,j + 0.80992\,k.$$

E twin-member:

$$n_c = 18^\circ \qquad h_c = 18^\circ$$
$$c_{E_0} = -0.29388\,i + 0.90450\,j + 0.30901\,k$$
$$n_b = 115^\circ \qquad h_b = 20.5^\circ$$
$$b_{E_0} = -0.84890\,i - 0.39585\,j + 0.35020\,k$$
$$a_{E_0} = [c_{E_0} \times b_{E_0}] = +0.43908\,i - 0.15940\,j + 0.88416\,k.$$

A and B : Z_I of Carlsbad; D and E : Albite M_{II}.
B and C : K_I of Roc-Tourné.
A and C : Albite M_I.

A and E : twin T of Börzsöny.

In every twin-member, the orthogonality of the two optical symmetry-axes must be examined. If the angle subtended by them is really 90°, then the product of their unit vectors is zero. This is, of course, impossible owing to the measurement errors. Up to a deviation of 0.5° the numerical data should not be changed, but in case of an error surpassing 0.5° one has to apply an adjusting procedure. Concerning the data published above no such deviations occurred, so that no use of adjusting was necessary.

Computing of the twin axes is carried out on the basis of bisector vectors of the optical directions. The computation of bisector vector takes place by means of addition, respectively subtraction of unit vectors of the corresponding directions. The obtained vector must be reduced to unit vector form.

The bisectors of optical symmetry-axes of A and B are:

$$\begin{aligned} Z_{Ia_0} &= +0.15186\, i + 0.38281\, j + 0.91126\, k \\ Z_{Ib_0} &= +0.17650\, i + 0.41870\, j + 0.88993\, k \\ Z_{Ic_0} &= +0.15107\, i + 0.38335\, j + 0.91116\, k. \end{aligned}$$

Owing to the closeness of the two $[n_\beta]$-s the mean value of the bisector of the directions $[n_\alpha]$ and $[n_\gamma]$ is computed and used in what follows:

$$Z_{I_0} = +0.15147\, i + 0.38308\, j + 0\ 91121\, k.$$

The bisectors of optical directions of A and C twin-members are:

$$\begin{aligned} M_{Ia_0} &= -0.86953\, i - 0.38456\, j + 0.30988\, k \\ M_{Ib_0} &= -0.87086\, i - 0.38457\, j + 0.30613\, k \\ M_{Ic_0} &= -0.87193\, i - 0.38003\, j + 0.30871\, k. \end{aligned}$$

The unit vector computed on the basis of the measurements is:

$$M_{I_0} = -0.87340\, i - 0.37976\, j + 0.30486\, k.$$

For the subsequent computations the measured M_I value will be used, because it is subtending an angle of 90° with the unit vector of Z_I. From these two directions the unit vector of the twin-axis of Roc-Tourné will be computed by means of vectorial multiplication:

$$K_{I_0} = [Z_{I_0} \times M_{I_0}] = +0.46283\, i - 0.84203\, j + 0.27706\, k.$$

The twin axis of Roc-Tourné results from the optical data of B and C as follows:

$$\begin{aligned} K_{Ia_0} &= +0.45843\, i - 0.84635\, j + 0.27118\, k \\ K_{Ib_0} &= +0.47000\, i - 0.83827\, j + 0.27640\, k \\ K_{Ic_0} &= +0.46852\, i - 0.84156\, j + 0.26882\, k. \end{aligned}$$

Because the value obtained by means of vectorial multiplication is the more accurate one, we will use it instead of the measured values, but we see that the deviation is insignificant.

The bisectors of the optical directions of twin-members D and E are:

$$M_{IIa_0} = +0.83308\, i - 0.54846\, j + 0.07183\, k$$
$$M_{IIb_0} = +0.83124\, i - 0.55154\, j + 0.06965\, k$$
$$M_{IIc_0} = +0.83122\, i - 0.55108\, j + 0.07338\, k.$$

The average value is:

$$M_{II_0} = +0.83185\, i - 0.55036\, j + 0.07162\, k.$$

The unit vector computed from the measured direction is:

$$M_{II_0} = +0.83608\, i - 0.54295\, j + 0.07845\, k.$$

This latter value subtends the angle 89° 30′, with the twin axis of Carlsbad and so it is just to be accepted.

The optical bisectors between twin-members A and E are:

$$T_{a_0} = -0.04487\, i - 0.91739\, j + 0.39546\, k$$
$$T_{b_0} = -0.03884\, i - 0.92176\, j + 0.38580\, k$$
$$T_{c_0} = -0.03395\, i - 0.91867\, j + 0.39356\, k.$$

The unit vector computed from the mean value is:

$$T_0 = -0.03922\, i - 0.91928\, j + 0.39162\, k.$$

The angle subtended by this with the twin-axis of Carslbad is 89° 56', i.e. it is more accurate, than the T_0 vector computed from the measurement.

The bisector of the (010) directions of the two complexes is:

$$T_{M_0} = -0.03732\, i - 0.92284\, j + 0.38336.k.$$

Let us transform the vector T_0 into the coordinate system XYZ (X-axis: twin-axis of Roc-Tourné, Y-axis: Albite twin axis, Z-axis: twin-axis of Carlsbad). We obtain:

$$X = -K_{I_0} = -0.46283\, i + 0.84203\, j - 0.27706\, k,$$
$$Y = +M_{I_0} = -0.87340\, i - 0.37976\, j + 0.30486\, k,$$
$$Z = +Z_{I_0} = +0.15147\, i + 0.38308\, j + 0.91121\, k.$$

The sign of the axes of the coordinate system XYZ has been fixed basing on the Euler angles of first kind.

The transformed value of the T − twin-axis in system I. is:

$$T_0' = +0.86441\, i' - 0.50275\, j' + 0.00225\, k'.$$

The Goldschmidt values are:

$$\varphi' = 120.5° \qquad \varrho' = 89.9°.$$

Thus, between the twin-members A and E twin-law according to $(1\bar{1}0)$ can be observed, i.e. the left form of the "Börzsöny" twin-law.

The observed data are shown in the annexed stereogram (Fig. 2.)

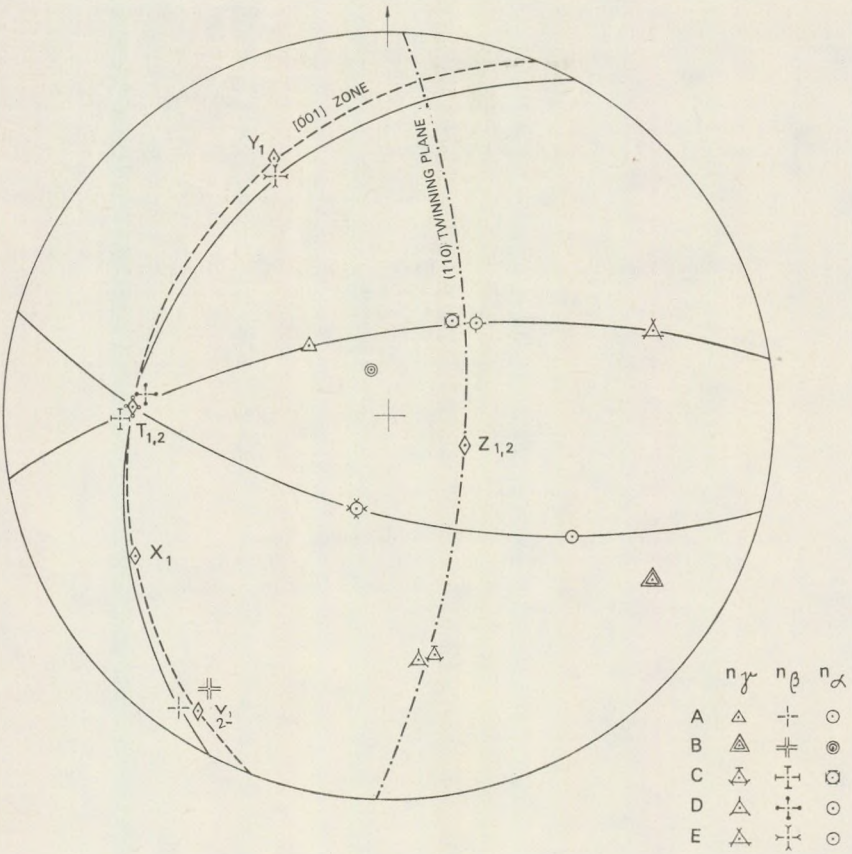

Fig. 2. Stereogram of a plagioclase twin crystal observed in andesite of Dömörkapu.

The interpolated values for the case of an anorthite content of 85% are for $(1\bar{1}0)$ as follows:

$$\varphi = 119.5°, \qquad \varrho = 90°.$$

The anorthite content of the twin crystal corresponds on the migration curve to 83 – 84%, the observation points are lying along the HT curve within a distance of 1 mm.

REFERENCES

Barth, T. W., 1969: Feldspars, London (1 – 261)

Burri, C. 1950: Anwendung der Vektorrechnung auf einige häufig auftretende kristalloptische Probleme. S. M. P. M. 30. (258 – 300).

Burri, C., 1956: Charakterisierung der Plagioklasoptik durch drei Winkel... S. M. P. M. 36. (539 – 592).

Burri, C., 1968: Die optische Orientierung von HT-labradorit aus Andesit von Kuchiré (Iran). S. M. P. M. 48. (781 – 801).

Burri, C., 1972: Zur Definition und Berechnung der optischen Orientierung von Plagioklasen. S.M. P. M. 52. (497 – 514).

Burri, C., 1974: Chemismus und optische Orientierung zweier Bytownits aus islandischem Olivinbasalt. S. M. P. M. 54. (1 – 17).

Burri, C., Parker, R., Wenk, Ed., 1967: Die optische Orientierung der Plagioklase. Basel. (1 – 334).

Burri, C., Örkényi-Bondor, L., Vincze-Szeberényi, H., 1976: Rechnerische Auswertung von U-Tischoperationen durch elementare Vektormethoden. S. M. P. M. 56. (1 – 38).

Hajós, Gy., 1966: Introduction to the geometry. Budapest (in Hungarian 1 – 594).

Koch, S., Sztróka y, K. I., 1967: Mineralogie (Budapest, in Hungarian, 1 – 936).

Köhler, A., 1950: Bemerkungen über Plagioklaszwillinge. Min. Petr. Mitt. Tscherm. 3. Serie 1. (347 – 352).

Köhler, A, Raaz, F., 1945 – 47: Gedanken über die Bildung von Feldspatzwillingen in Gesteinen. Verh. Geol. Bund. Wien (163 – 171)

Lengyel, E., 1925: Petrogenetische Beobachtungen an den Andesiten von der Umgebung von Pilisszentlászló. Földt. Közl. 55 (1q8 – 127, in Hungarian).

Örkényi – Bondor, L., Vincze – Szeberényi, H., 1974: (110), ($1\bar{1}0$), (130) and ($1\bar{3}0$) Plagioclase Twinning in Andesite from Hungary, Acta Geol. Ac. Sc. Hung. 18., (99 – 135).

Reinhard, M., 1931: Universale Drehtischmethoden. Basel.

Wenk, Ed, Glauser, A. Schwander, H., Trommsdorf, V., 1972: Twin laws, optic orientation and composition of plagioclases from rocks 12 051, 14 053 and 14 310. Geoch. Cosmoch. Acta 1. (581 – 589).

NUMERICAL MODELLING OF INDUCED CONVECTION ABOVE SUBDUCTING SLABS

L. BODRI and B. BODRI

Department of Geophysics, Eötvös University,
Budapest

Received: 1 March 1978

РЕЗЮМЕ

В работе проведено численное исследование потока вещества, вызванного движением опускающейся литосферной плиты. Математическое моделирование этого потока проводится в остром углу между горизонтальной литосферной плитой и опускающейся литосферой. Расчеты вынужденного потока двумерные, зависящие от времени, с вязкостью, зависящей от температуры. Расчеты очень чувствительны к реологическим свойствам материала в районе схождения двух литосферных плит. Моделирование вулканизма островных дуг, скорее всего, не может быть осуществлено без учета нелинейной реологии материала, а именно, прочности, пластичности и т. д. Вынужденный поток, исследованный в данной работе, является возможным объяснением вулканизма островных дуг, а также высокого теплового потока окраинных бассейнов.

Introduction

It is now well established in plate tectonics that the oceanic plates, continuously created at midoceanic ridges, descend into the mantle at ocean trenches as sketched in Figure 1. However, some of the processes occuring beneath such trenches and associated island arc – marginal basin systems have not yet been understood in all details. The observed large gravity anomalies (see in Fig. 2) near the trench systems are often attributed to the higher density of the relatively cold descending oceanic plates, however, it seems to be more probable that the regional positive anomalies extending from the island arc to, at least, the adjacent continental margin are produced by active upward emplacement of mantle material behind the subducting oceanic plates. The sometimes very detailed heat flow data of island arc areas show a very characteristic behaviour as presented in Figure 2. The heatflux from the oceanic plate as it entrers the subduction zone is sub-normal, there is a small decrease in the trench and the arc-trench gap but when the volcanic arc is reached the heat flow increases rapidly and relatively high values conserve for long distances behind the arc. At present there are two different approaches to the heat generation problem. Turcotte and Oxburgh (1968, 1970) and others (e.g. Minear and Toksöz, 1970) have attributed the high surface heat flow to heat generation by viscous dissipation along a thin slip zone

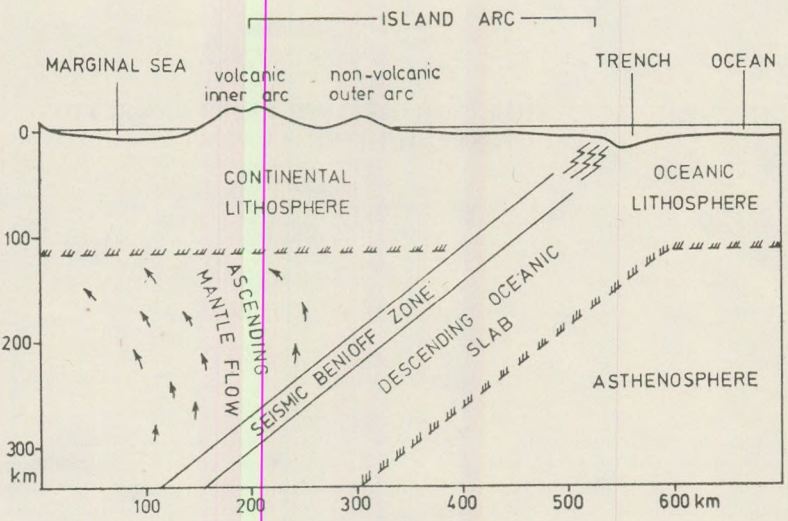

Fig. 1. Schematic cross-section of an island arc area.

Рис. 1. Схематический профиль района островной дуги

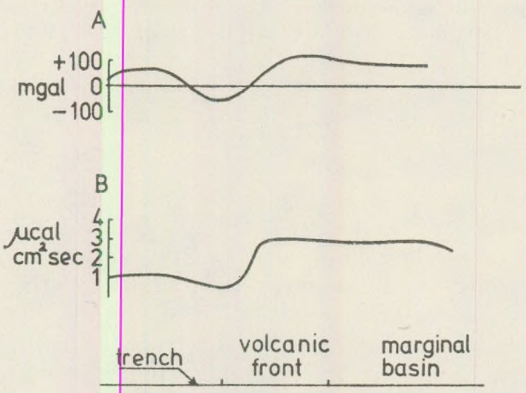

Fig. 2. Typical gravity anomaly distribution (A) and heat flow profile (B) in island arc-marginal basin systems.

Рис. 2. Типичный профиль гравитационных аномалий (A) и теплового потока (B) в системе островная дуга- окраинный бассейн

between the descending slab and the overriding mantle. McKenzie and Sclater (1968) pointed out that that stress or frictional heating in the Benioff zone alone would require unrealistic temperatures (7000°C) and a long time for heat transfer to the surface (300 m. y.) for producing the observed heat flow behind the arcs. According to Andrews and Sleep (1974) in the case of the mechanism of frictional heating the region above the slab must be fluid enough to convect termally, and at the same

time yet so viscous that the descending slab can give rise to stress of about 2 kilobars. An other approach to the problem is the idea of Andrews and Sleep (1974) and others (e. g. Isacks, Oliver and Sykes, 1968; McKenzie, 1969), which suggests that high heat flow in marginal seas and island arc volcanism may be explained by a mechanically induced circulation of material within the wedge between the two lithospheric plates. In this paper we investigate this later process with numerical calculations.

Geophysical model and numerical results

The hydrodynamic modelling of material flow in the wedge region between the slab and the adjacent continental lithospheric plate is described below. Our model is in general similar to that of Andrews and Sleep (1974), however, there are also some significant differences.
Figure 3, a schematic diagram of the area of the convergent plate margins, shows the fixed landward plate, the moving slab, a thin slip zone between the two lithospheric plates and two wedge-shaped regions separated by

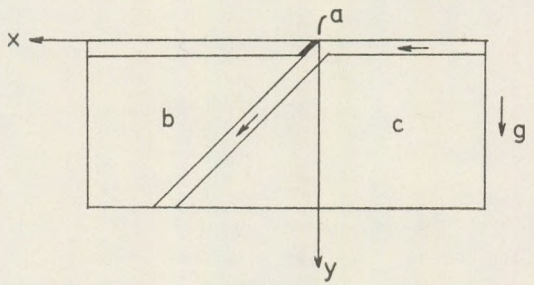

Fig. 3. Geometry of the model.

Рис. 3. Геометрия математической модели

the slab. It is obvious that only some particular regions of this complex system may be considered as viscous fluid. Observations of different types suggest that the independent lithospheric plates should be considered as rigid bodies affected by deformations only in thin zones near to their boundaries. This conclusion significantly determines the choosing of probable rheological models of the lithosphere and is against considering it as viscous fluid. According to hydrodynamical considerations, in case of typical fluids the hydrodynamic equations may be applied to processes the periods of which are much greater than molecular times. When a very viscous fluid is considered the situation is quite different; these equations are not more valid even in case of much greater periods of motion. According to Landau and Lifshitz (1953) if the period of any force $\frac{1}{\omega}$ is large in comparison with the τ relaxation time, i. e. $\omega\tau \ll 1$, then the considered fluid

manifests itself as a typical viscous one. The τ relaxation time for such fluids may be obtained from the following relation

$$\eta \sim \tau \mu , \tag{1}$$

where η is viscosity and μ is shear modulus. Taking $\mu = 0.5 \cdot 10^{12}$ CGS, we find that in our case (the time step in the numerical procedure is 10^6 y) the hydrodynamic equations may be valid up to viscosities $\eta = 10^{24} - 10^{25}$ poise. Therefore, as the calculation proceeded in time, the top of the fluid region might not lie above the actual isoline of viscosity of 10^{24} poise.

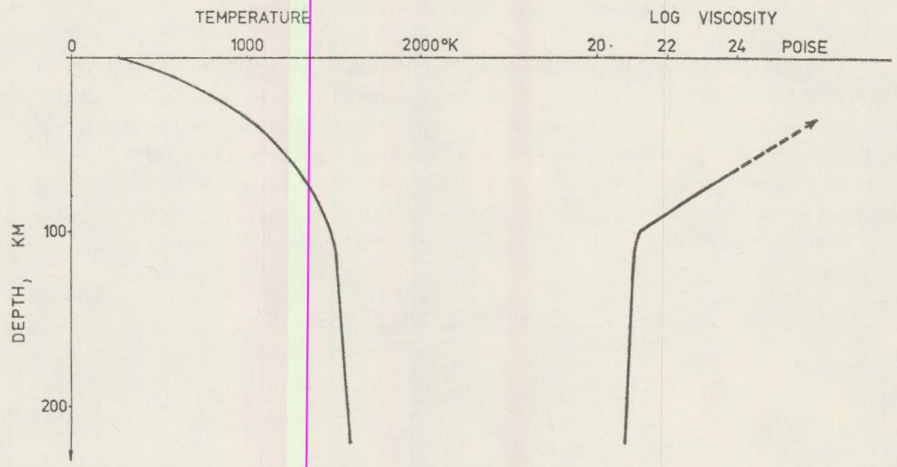

Fig. 4. Temperature and viscosity distribution in the initial, laterally uniform state.

Рис. 4. Распределение температуры и вязкости в первоначальной горизонтально однородной стадии

Assuming an initial, laterally uniform temperature distribution as shown in Figure 4, the corresponding viscosity profile can be calculated by the simple relation (Z h a r k o v et al., 1971)

$$\eta = \eta_0 \exp \frac{E}{RT} , \tag{2}$$

where T is temperature in deg K, $\eta_0 = 1.104 \cdot 10^8$ poise and $\frac{E}{R} = 4.758 \cdot 10^4$ deg. So, in the initial state region b with an upper boundary depth of 60 km is fluid enough to convect thermally, while the overriding layer should be considered as a solid. Since the thermal conductivity of the down-going slab is assumed to be negligibly small, the zero heat flux boundary condition should be used on its surface. It means that the moving slab will retain its originally low temperature even after it has sunk to considerable depths. Since the maximal temperatures within the slab are not more than

700 – 800°C (McKenzie, 1969), it can be considered as a solid during the whole period of calculation. So, the problem is the modelling of induced convection within a fluid wedge region bounded by two solid plates. The solution of the task, however, is rather problematic, since it was recognized in hydrodynamics long ago that sharp changes in the form of a surface boundaring any fluid region (in our case it is the corner of the wedge) give rise to large, even to infinite local stresses. The infinite increasae of stresses at such places is due to the more complicated (non-linear) rheological properties of material, i.e. the linear Hooke's law used for the determination of stesses is not more valid here. The discussion of causes of concentration of stresses is out of the scope of the present paper, we note only that in similar to this models it should be always taken into account that the lithospheric plates are characterized by τ_s finite yield stresses and while the stresses arising during any process do not exceed τ_s the plates remain elastic, or (in the first approximation) rigid bodies. An elementary calculation shows, however, that in our case the above mentioned non-linear rheological behaviour of material will take place in a zone of quite small extent, away from the corner the stresses will decrease rapidly. In the present study we assumed that in the region where the stresses exceed the critical value the lithosphere will transform to plastic state with properties similar to those of a viscous fluid of some η_e effective viscosity. This is equivalent to changing the lower boundary of the solid landward plate during the process of calculation. The critical stresses will, of course, exercise an influence also on the slab but because of the motion always new and new parts of the sinking slab will be affected by a certain level of stresses. Therefore its boundary was considered as unchanged during the whole period of calculation. A thin slip zone (denoted by *a* in Fig. 3) filled with oceanic crust is included between the two plates. The rocks of the oceanic crust are characterized by significantly less yield stresses than those of the lithosphere, therefore entered the zone of friction of the two plates it must entirely transform to plastic state with rheology similar to that of a viscous fluid included between the surface of two solids moving relatively to each other. The thermal and mechanical state of this zone has been investigated in details by a number of authors (e. g. Turcotte and Oxburgh, 1968; Turcotte and Schubert, 1973; Jischke, 1975). The horizontal extent of the slip zone, however, is much less than that of our calculational region, therefore it appeared in our model as a thermal boundary condition on the solid landward plate. The induced tectonic flow in wedge *b* has been calculated on the basis of equations of viscous motion and of thermal conduction. The two-dimensional equation of motion was taken in the following form:

$$\frac{\partial^2}{\partial x\,\partial y}\left[4\eta\frac{\partial^2 S}{\partial x\,\partial y}\right]+\left(\frac{\partial^2}{\partial y^2}-\frac{\partial^2}{\partial x^2}\right)\left[\eta\left(\frac{\partial^2}{\partial y^2}-\frac{\partial^2}{\partial x^2}\right)S\right]+$$

$$+\varrho_0 g_0 \alpha\frac{\partial T}{\partial x}=0\,, \qquad (3)$$

where S is stream function, T is temperature, η is viscosity, α is thermal expansivity, ϱ_0 is density and g_0 is gravity acceleration. The equation above is in Boussinesq approximation which means that only the variation of density with temperature need be considered, and only in the body-force term. The equation of heat conduction is

$$\frac{\partial T}{\partial t} - = \left(\frac{\partial S}{\partial y}\frac{\partial T}{\partial x} - \frac{\partial S}{\partial x}\frac{\partial T}{\partial y}\right) + \frac{1}{\varrho_0 c_p}\left[\frac{\partial}{\partial x}\left(K\frac{\partial T}{\partial x}\right) + \frac{\partial}{\partial y}\left(K\frac{\partial T}{\partial y}\right) + \right.$$

$$\left. + 4\eta\left(\frac{\partial^2 S}{\partial x\,\partial y}\right)^2 + \eta\left(\frac{\partial^2 S}{\partial y^2} - \frac{\partial^2 S}{\partial x^2}\right)^2 + H\right], \qquad (4)$$

where K is thermal conductivity and H is the rate of heat generation per unit volume. The adiabatic temperature changes have not been taken into acccunt in equation (4).

The question of boundary conditions arises well known difficulties. Equation (3) has been solved in the wedge bounded by the slab and the landward plate. As already mentioned above, the lower boundary of the island arc plate was determined by isoline of $\eta = 10^{24}$ poise. The boundary conditions on the top of the wedge are

$$S = 0$$

$$\text{and } \vec{v} = 0,$$

$$\text{where } \vec{v} = \left\{\frac{\partial S}{\partial y};\ -\frac{\partial S}{\partial x};\ 0\right\}. \qquad (5)$$

On the slab boundary we have

$$S = 0$$

$$\text{and } \vec{v} = \vec{v_0}, \qquad (6)$$

where $\vec{v}_0$ is the slab velocity, parallel to the surface of the slab which is dipped in our case at 45°. There are no lower and left-hand side boundaries to the wedge in our model. In order to be able to obtain solution a re-zoning procedure was needed as it has been applied by Andrews and Sleep (1974). The calculation was started with a grid extending horizontally 800 km from the corner and extending to a depth of 400 km with zones of 20×20 km. The values of stream function on the critical boundaries of this grid were available from the analytic solution of Batchelor (1967). After having obtained the solution on the coarse grid, a finer grid extending to 600×300 km with zones 10 by 10 km was used. Boundary values for the stream function were taken from solution related to the coarse grid. The equation of the heat conduction has been solved in the whole region behind the slab. The thermal boundary conditions are

$$T(y = 0) = 273°\text{K} \qquad (7)$$

throughout the free surface of the landward plate and

$$\frac{\partial T}{\partial n} = 0 \tag{8}$$

at all points of the astenosphere-slab boundary. Here $\frac{\partial}{\partial n}$ denotes differentiation in the direction of the outward normal to the surface of the slab. The temperature at each point on the surface of the slab was assumed to be equal to that of the fluid astenosphere, obtained from equation (4) with the boundary consition given above. The zero heat flux boundary condition however, is not more valid along the line of contact of the two lithospheric plates, since a thin slip zone of considerable conductivity is located between them. It was already mentioned above that because of the small horizontal extent of this zone, its presence has only been taken into account as a temperature boundary condition on the landward plate. The temperature on the right boundary of the solid landward plate was assumed to be constant and equal to 800°C.

Besides the stream function the stress components also have been computed during the iterative procedure. A yield condition was introduced according to which the stress components at the boundaries should not exceed some $s_{\max}$ given value equal to 1 kb in our case. This condition can be formulated as

$$|s_{xx}| \leq s_{\max}, \quad |s_{yy}| \leq s_{\max}. \tag{9}$$

If inequalities (9) are not satisfied, then the values of viscosity found from the constitutive relation are replaced by some effective viscosity and the boundary is changed correspondingly. The temperatures are computed only if equality holds in expressions (9) after convergence is achieved in the iterative procedure for equation (3). If the yield condition is not satisfied at any point of the grid, then some effective temperature corresponding to effective viscosity η_e is introduced there.

The calculated streamlines and isotherms are shown in Figures 5, 6 and 7 at 1.0, 4.0 and 7.0 My from start of subduction respectively The following numerical values of parameters are used throughout these calculations:

$$\varrho_0 = 3.4 \text{ g cm}^{-3}$$

$$g_0 = 990 \text{ cm sec}^{-2}$$

$$\alpha = 4 \cdot 10^{-5} \text{deg}^{-1}$$

$$c_p = 0.311 \text{ cal g}^{-1} \text{deg}^{-1}$$

$$\eta_e = 1 \cdot 10^{24} \text{ poise.}$$

The assumed dependence of thermal conductivity on temperature is

$$\lambda = a + b\, T^3,$$

where $a = 6 \cdot 10^{-3}$ cal cm^{-1} sec^{-1} deg^{-1} and

$b = 5 \cdot 10^{-12}$ cal cm^{-1} sec^{-1} deg^{-1}.

The viscosity was calculated by formula (2), the slab dipped at 45° and was given a constant velocity of 10 cm yr^{-1}. The temperature and the corresponding viscosity distribution in the initial state are laterally uniform. At 1.0 My from start of calculation the solution for the stream function does not deviate significantly from Batchelor's wedge solution. Near to the slab boundary, however, a hot zone appears with low viscosity. Stresses arising at the corner, begin to exceed the critical value already at the first steps of calculation. The horizontal stress near the corner is compressive, the region of large stresses extends approximately to 40 km both along

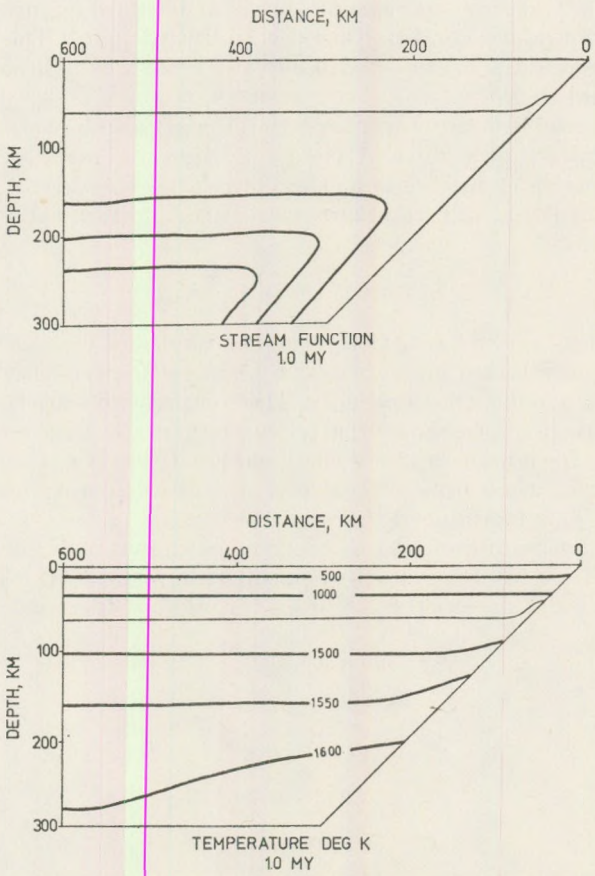

Fig. 5. Streamlines and isotherms at 1.0 My from the beginning of subduction.

Рис. 5. Линии тока и изотермы через 1.0 млн. лет после начала субдукции

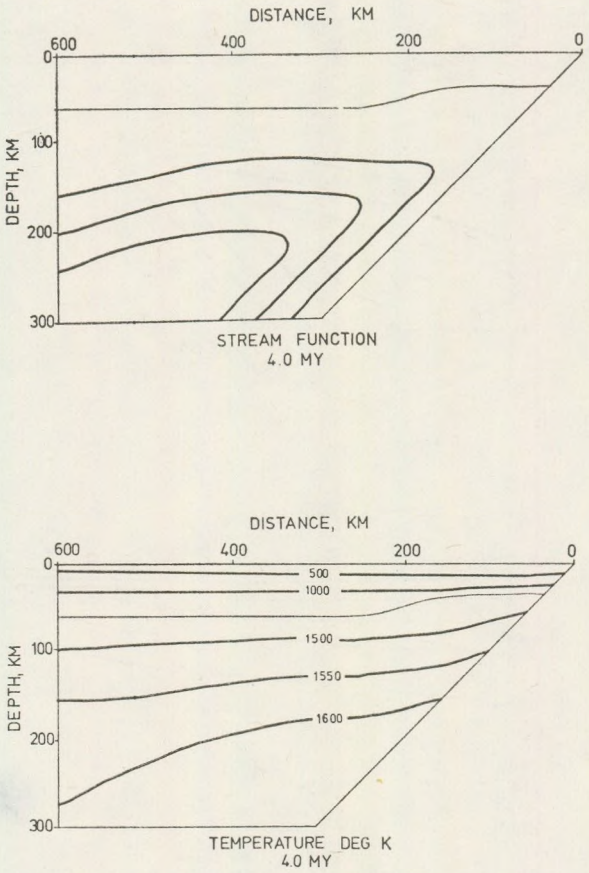

Fig. 6. Streamlines and isotherms at 4.0 My.

Рис. 6. Линии тока и изотермы в 4.0 млн. лет

the horizontal plate and the slab boundary. The lithosphere somewhat thinned at 1.0 My only in the zone of immediate contact of the two plates. As time progresses this zone spreads, so that at 7.0 My the region of thinned lithosphere extends up to 100 km. This result is quite realistic, since all of the stress components may be expressed as biharmonic functions and according to a fundamental property of these functions, the maximal values of stress components are reached at the boundaries of the considered region. As it expected, the streamlines dublicate the shape of the boundaring surfaces. As time proceeds, the temperature within the convecting region increases continuously, isotherms become nonhorizontal while within the plate they remain horizontal and there are not significant changes of temperature. The calculated heat flow profile above the region at 7.0 My is shown in Fig. 8. There is a high heat flow in the zone of the thinned lithosphere and it decreases away from this zone in both directions.

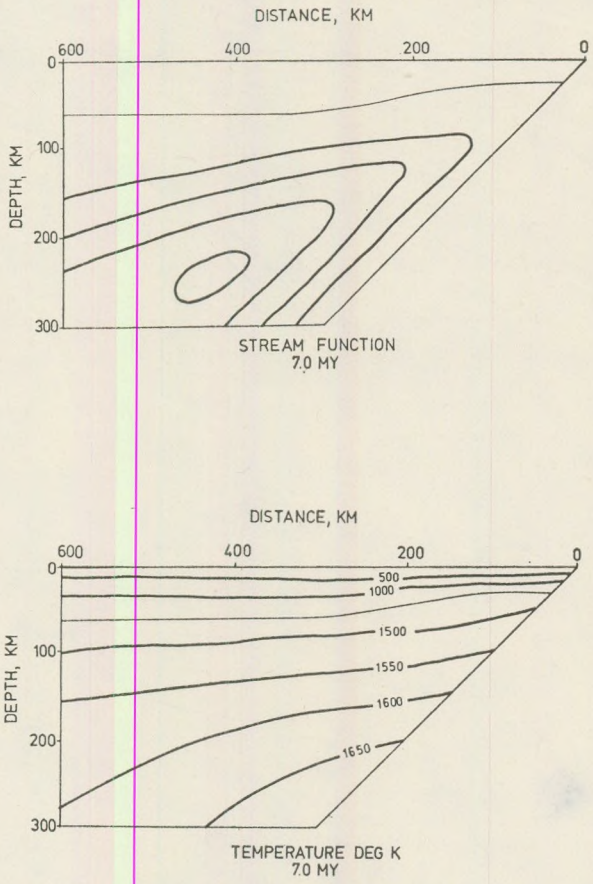

Fig. 7. Streamlines and isotherms at 7,0 My.

Рис. 7. Линии тока и изотермы в 7.0 млн. лет.

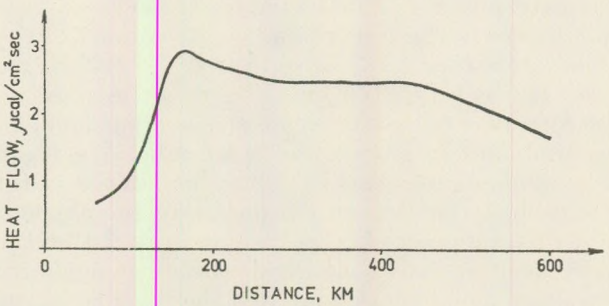

Fig. 8. The calculated heat flow profile at 7.0 My from start of subduction.

Рис. 8. Расчитанный профиль теплового потока через 7.0 млн. лет после начала субдукции

Remarkable similarity exists between this calculated profile and the measured one (see Fig. 2).
The following model of island arc volcanism is supported by these calculations. The volcanic arc might occur closely above the corner of the slab with the horizontal lithosphere. Due to changes in rheology of material part of the lithosphere can become thinned, a certain portion of material of the landward plate is given the possibility to take part in the general convective motion that takes place in the wedge, so the portion of the plate adjacent to the slab is slowly subducted with the slab. As time progresses, the zone of thinned lithosphere expands so, that new volcanic arc may also occure at relatively larger distances away from the corner. The zone where the lithosphere continuously gets thicker is characterized by decreasing of the heat flow from high to normal values. Upwelling flow in this zone may in principle, induce spreading, somewhat similar to that at a mid-ocean ridge but it is non symmetrical here.

Conclusions

The wedge between the horizontal lithosphere plate and the subducting slab is fluid enough that induced convection can take place there for time of order of magnitude of My. The lithosphere plates should be considered as solids and at the zones of critical stresses non-linear rheology is to be applied.
Critical stresses arise near sharp changes of shapes boundaring the convecting fluid region. As time progresses, these zones will be extending and stresses certainly exceed in this region the yield stress of lithosphere.
The whole island arc area extends horizontally to some hundered kms, i. e. it almost entirely located in the zone of large stresses so it seems probable that models of island arcs can not be constructed without taking into account non-linear processes, like plasticity, yielding etc. The modelling of these later processes, however, is an extremely difficult task, the way suggested here for including them into the model is probably a crude approximation, however, it leads to realistic results in the greater, part of the investigated area.
However, even by this idealized modelling of the effects of lithisphere-astenosphere interactions some of processes occuring beneath island arcs may be explained satisfactorily. It seems to be probable that elasto-plastic behaviour of lithosphere may be responsible for processes arising asymmetrically on both sides of the subduction zone, since stresses and consequently the effects of non-linear rheology arising on the corner of an obtuse-angled wedge probably significantly less then those on the other side of the slab.

REFERENCES

Andrews, D. J. and Sleep, N. H., 1974. Numerical modelling of tectonic flow behind island arcs. Geophys. J. R. Astron. Soc., 38: 237 – 251.

Batchelor, G. K., 1967. An introduction to fluid dynamics. Cambrige University Press, Cambrige, 224 pp.

Isacks, B., Oliver, J. and Sykes, L., 1968. Seismology and the new global tecnics. J. Geophys. Res., 73: 5855 – 5899.

Jischke, M. C., 1975. On the dynamics of descending lithospheric plates and slip zones J. Geophys. Res., 80: 5876 – 5886.

Landau, L. D. and Lifshitz, E. M., 1953. Mechanika sploshnih sred. GITTL., Moscow, 788 pp. (in Russian).

Minear, J. W. and Toksöz, M. N., 1970. Thermal regime of a downgoing slab and new global tectonics. J. Gephys. Res., 75: 1397 – 1419.

McKenzie, D., 1969. Speculations on the consequences and causes of plate motions. Geophys. J. R. Astron. Soc., 18: 1 – 32.

McKenzie, D. P. and Sclater, J. G., 1968. Heat flow inside the island arcs of the northwestern Pacific. J. Geophys. Res., 73: 3173 – 3179.

Oxburgh, E. R. and Turcotte, D. L., 1968. Problem of high heat flow and volcanism associated with zones of descending mantle convective flow. Nature, 218: 1041 – 1043.

Oxburgh, E. R. and Turcotte, D. L., 1970. Thermal structure of island arcs Geol. Soc. Am. Bull., 81: 1665 – 1688.

Turcotte, D. L. and Schubert, G., 1973. Frictional heating of the descending lithosphere. J. Geophys. Res., 78: 5876 – 5886.

Zharkov, V. N., Trubicin, V. P. and Samsonienko, L. V., 1971: Fizika planet i Zemli. Nauka, Moscow, 383 pp. (in Russian).

INTERPRETATION OF MAGNETIC ANOMALIES BY POWER SPECTRUM ANALYSIS

A. MESKÓ and K. KIS

Department of Geophysics, Eötvös University, Budapest

Received: 1 Juli 1978

SUMMARY

Power spectra of magnetic field data have been used to estimate the average depth and some other parameters of magnetized bodies. In this paper, which consitutes Part I of a series, the foundations and applicability of the method are discussed in some details. The logarithms of the radial spectra due to prismatic bodies are investigated. It is shown that although the dominating term in the spectra is the term $-4\pi h_{top} f_r$, connected with the depth to the top of the magnetized bodies the influence of other parameters and their probability density functions can not be neglected.

The contribution of a deeper ensemble of prismatic bodies dissappears very rapidly with increasing f_r thus in the estimation of the average depth to the top of deeper sources the first few spectral lines may be used, only. The depth extent could be determined very seldom even for the shallower ensemble of sources.

Introduction

Spectral analysis of potential field data has become a standard tool for geophysical interpretation in recent years. Frequency spectra of the gravity and magnetic fields have been derived for a number of geometrical bodies and for various distribution of certain types of bodies including two- and three-dimensional dykes, two-dimensional structures with polygonal cross sections, random distributions of sources in a given depth interval, monopole and dipole coating in equivalent strata etc. (Odegard and Berg, 1965, Bhattacharyya 1965, 1966, 1971, Spector and Bhattacharyya, 1966, Spector and Grant, 1970, Syberg, 1972, Bhattacharyya and Leu, 1975, Sengupta and Dar, 1977 and others).

It has been found that the expressions of the spectra, besides other factors, consist of sums of exponentials with exponents which are linear functions of frequency. Therefore when plotted in a logarithmic scale the amplitude spectra or power spectra show frequency intervals, where the functions may well be approximated by straight lines. The slopes of these lines can be used to estimate certain characteristic parameters of the bodies (depths to the top of the prismatic bodies, or depths of the equivalent strata or depths to the bottom etc).

Analysis of measured gravity and magnetic field data have shown that the theoretical foundations are sound. Power spectra almost always indicate two distinct depths which may be related to a set of deeper and a set of shallow sources. In some cases the depth extent of one set of sources can also be estimated (Spector and Grant 1970, Naidu, 1970, Lehmann, 1970, Syberg, 1972, Bhattacharyya and Leu, 1975, Cianciara and Marcak, 1976, Hahn, Kind and Mishra, 1976). Though the good separation of sources at different depths, especially in the case of the gravity anomalies, needs a more satisfactory explanation than the one what the present theory provides, the method could be considered as well established in current practice.

The scope of this paper is to discuss the application and results of the method to vertical component anomalies of the magnetic field in the Pannonian Basin. Some of the preliminary results have been shortly summarized elsewhere (Meskó and Kis, 1977). In Part I we discuss the underlying principles of the method and report investigations by prismatic models.

Power spectrum of the magnetic field due to a vertical prismatic body

The vertical prism has been considered as the basic interpretational model of magnetic field components. This simple model has been used with success for estimating various parameters of the magnetized bodies from the magnetic anomalies (Peters, 1949, Vacquier, 1951, Steenland, 1962, etc). Spector and Grant (1970) attribute the success to the fact that magnetic anomaly patterns are largely shaped by the depths and horizontal dimensions of the sources besides the directions of their magnetization and they are influenced relatively little by the details of their boundaries. Thus we consider first the power spectrum of the magnetic anomalies due to single vertical prismatic bodies.

The expressions for the magnetic field vector components due to a vertical prismatic body as well as the corresponding Fourier spectra can be found in the literature (e. g. in Bhattacharyya, 1966). A general formula of the Fourier spectra including all cases of interest reads as

$$G(f_x,\ f_y) = \frac{2ab}{f_r}\,\mathrm{sinc}\,(af_x)\,\mathrm{sinc}\,(bf_y)(e^{-2\pi h_1 f_r} - e^{-2\pi h_2 f_r})\cdot I \qquad (1)$$

The factor I depends on several variables and it is related to the type of the anomaly field considered. When g(x, y) describes total magnetic field anomalies the factor I becomes

$$I = \frac{\pi m_0}{f_r}\left[-lLf_x^2 - mMf_y^2 + nNf_r^2 - \alpha_{12}f_xf_y + j\alpha_{13}f_xf_r + j\alpha_{23}f_yf_r\right]. \qquad (2)$$

The variables in the formulas denote the following quantities

a	width of the body,
b	length of the body,
h_1	depth to the top of the body,
h_2	depth to the bottom of the body,
m_0	intensity of magnetization within the body,
L, M, N	direction cosines of magnetization,
l, m, n	direction cosines of the geomagnetic field,
f_x and f_y	spatial frequencies (or wavenumbers) in the x and y directions, respectively,

$f_r = (f_x^2+f_y^2)^{1/2}$ radial spatial frequency.
The notations are explained in *Fig 1.*

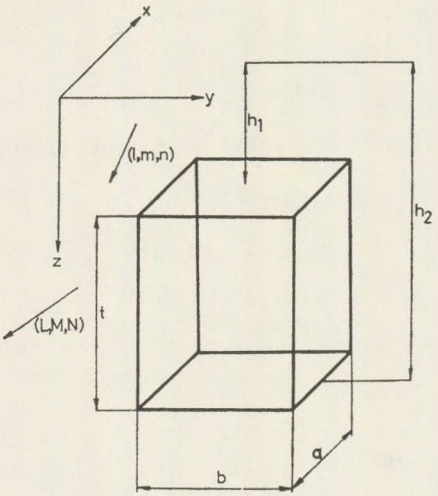

Fig 1. Notations used in the expressions describing the magnetic fields due to prismatic bodies

The functions α_{12}, α_{13} and α_{23} are defined by

$$\alpha_{12} = Lm+Ml, \tag{3.a}$$

$$\alpha_{13} = Ln+Nl, \tag{3.b}$$

$$\alpha_{23} = Mn+Nm. \tag{3.c}$$

When the body is magnetized in the direction of the geomagnetic field

$$l = L, \quad m = M, \quad n = N$$

and the formulas (3) become

$$\alpha_{12} = 2\ \mathrm{lm}, \tag{4.a}$$

$$\alpha_{13} = 2\ \mathrm{ln}, \tag{4.b}$$

$$\alpha_{23} = 2\ \mathrm{mn}. \tag{4.c}$$

When we consider vertical anomalies $l = m = 0$ and the factor I becomes

$$I = \frac{\pi m_0}{f_r}\left[N f_r^2 + jL f_x f_r + jM f_y f_r\right]. \tag{5}$$

The power spectrum can be derived by taking the squared modulus of the spectrum $G(f_x, f_y)$. Let us introduce polar coordinates in the frequency domain by $f_x = f_r \cos\alpha$, $f_y = f_r \sin\alpha$. Then we may write for the general case

$$|G(f_r, \alpha)|^2 \equiv E(f_r, \alpha) = K S^2(f_r, \alpha)\, R_T^2(\alpha)\, e^{-4\pi h_1 f_r}\,(1 - e^{-2\pi t f_r})^2, \tag{6}$$

with

$$K = (2\pi)^2 a^2 b^2 m_0^2,$$

$$S^2(f_r, \alpha) = \mathrm{sinc}^2(a f_r \cos\alpha)\,\mathrm{sinc}^2(b f_r \sin\alpha),$$

$$R_T^2(\alpha) = n^2 + (l\cos\alpha + m\sin\alpha)^2,$$

$$R_M^2(\alpha) = N^2 + (L\cos\alpha + M\sin\alpha)^2,$$

$$t = h_2 - h_1 \ \text{(depth extent)}.$$

The special cases, mentioned previously, are obtained by the following substitutions

$$R_T^2(\alpha) = R_M^2(\alpha)$$

(induced magnetization),

$$R_T^2(\alpha) = 1.$$

(vertical component of the magnetic field).

The radial power spectrum is obtained by integrating over the variable α, and it has an even simpler shape as follows

$$E(f_r) = K_r\, S_r^2(f_r)\, e^{-4\pi h f_r}\,(1 - e^{-2\pi t f_r})^2 \tag{7}$$

where

$$K_r = \frac{1}{2\pi}\int_0^{2\pi} K R_T^2(\alpha)\, R_M^2(\alpha)\, d\alpha, \tag{8}$$

$$S_r^2(f_r) = \frac{1}{2\pi}\int_0^{2\pi} S^2(f_r, \alpha)\, d\alpha = \frac{1}{2\pi}\int_0^{2\pi} \mathrm{sinc}^2(a f_r \cos\alpha)\,\mathrm{sinc}^2(b f_r \sin\alpha)\, d\alpha, \tag{9}$$

and $h = h_1$.

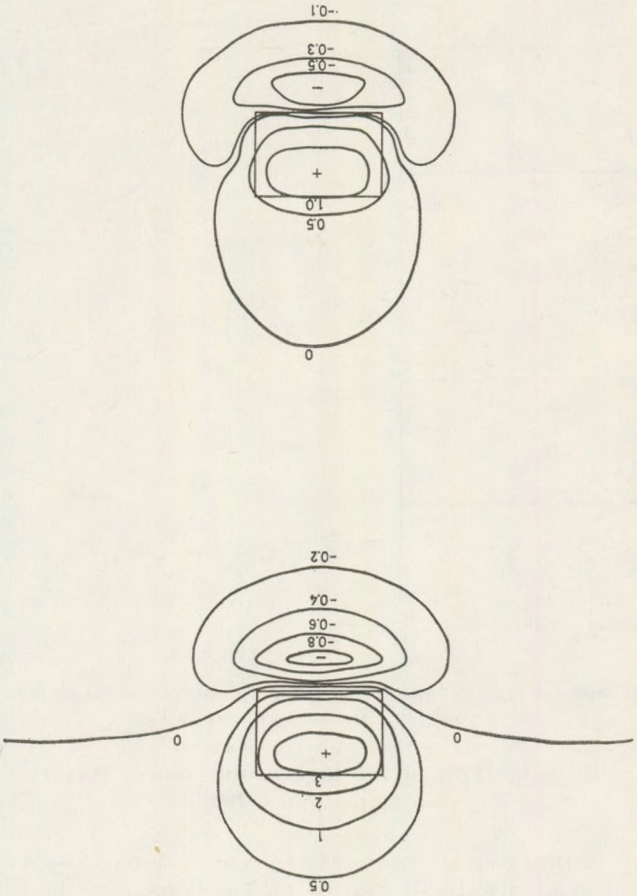

Fig. 2. Total magnetic field due to rectangular prisms with parameters
$a = 4, b = 6, h = 1, t = \infty$ (top) and
$a = 4, b = 6, h = 1, t = 1$ (bottom)
(induced magnetization is assumed in both cases, the geomagnetic field vector has inclination $I = 60°$, declination $D = 0°$)

The logarithm of the radial power spectrum than becomes

$$\ln E(f_r) = K + 2 \ln S_r(f_r) + 2 \ln(1 - e^{-2\pi t f_r}) - 4\pi h f_r . \qquad (10)$$

The dominating term is the linear function $-4\pi h f_r$ though $\ln S_r (f_r)$ and $\ln$ (1-exp(-$2\pi t f_r$)) may also modify the rate of linear decrease with increasing f_r. The extent of the effect of these factors have been investigated by numerical models.

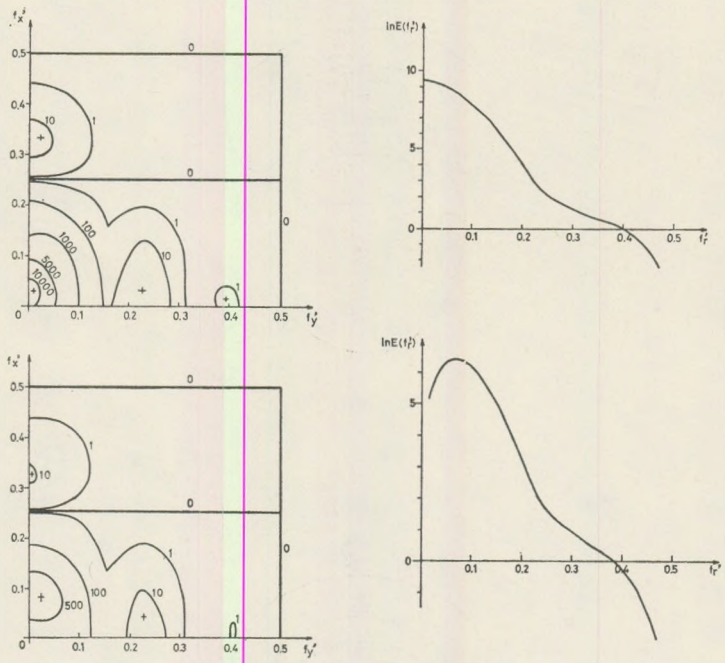

Fig 3. Two-dimensional spectra (on the left) and logarithmic radial spectra (on the right) of the magnetic field data shown in Fig. 2.

Investigations of the logarithmic power spectra due to prismatic bodies

In order to imitate the processing of real data as close as possible we computed the magnetic fields due to various prismatic bodies in 32×32 points forming a regular square grid. The origin of the coordinate axis x and y was placed above the center of the prism. The fourier transforms of the data have been determined by the FFT (Fast Fourier Transform) algorithm and radial power spectra have been derived by numerical integration of the squared modulus of the Fourier transforms. Data windows have not been applied.

Fig. 2. shows two examples of the computed magnetic anomaly due to prisms with parameters $a = 4$, $b = 6$, $h = 1$, $t = \infty$ and $a = 4$, $b = 6$, $h = 1$, $t = 1$ (dimensions are understood in the units of grid spacing) and with inclination 60°, declination 0°, induced magnetization in both cases. Computed data have been compared to magnetic fields for the same models published in the literature (A n d r e a s e n and Z i e t z, 1969) in order to estimate the accuracy of our method based on the Fourier transform approach. The two-dimensional Fourier transforms of the previous examples are given in *Fig. 3* together with the logarithmic power spectrum (on the right).

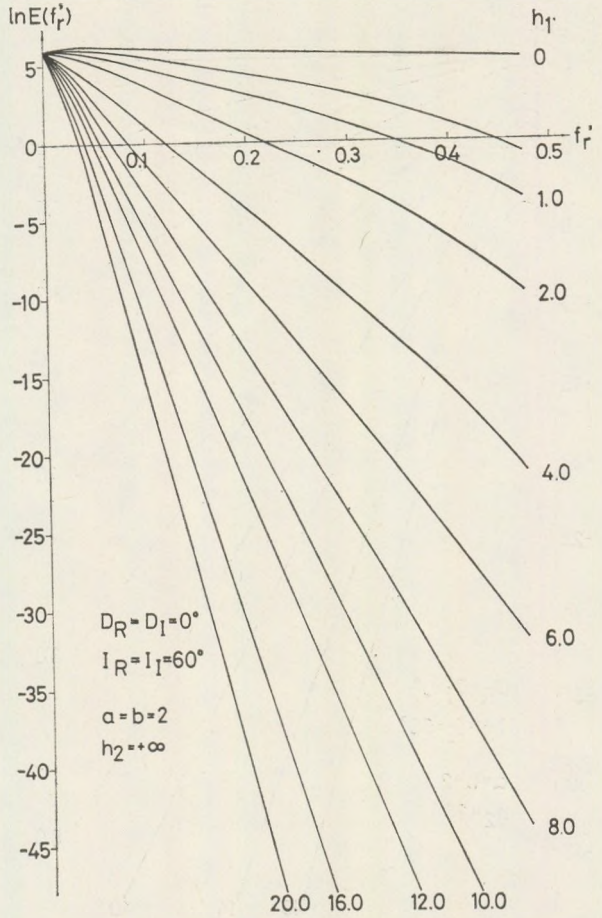

Fig. 4. Logarithmic radial spectra of magnetic fields (total field) due to prisms illustrating the effect of depth to the top of the bodies. Parameters are indicated. Map window is 32×32

Figures 4 – 10 show some of the results of model investigations.

Figure 4 illustrates the logarithmic spectra for prisms and shows the effect of the depth to the top of the prism. The horizontal dimensions are $a = b = 2$ the vertical extents are infinite and the depths to the top are equal to 0, 0.5, 1, 2, 4, 6, 8, 10, 12, 16 and 20. (All dimensions are expressed in units of grid spacing.) *Fig. 5* shows the logarithmic spectra for prisms with the same horizontal cross section (2×2) but for $h_2 = 20$ and $h_1 = 0$, 0.5, 1, 2, 4, 6, 8, 10, 14 and 18.

These figures proves that the effect of the depths to the top dominates at least for cases when the horizontal cross section is small enough compared to the dimensions of the map window (2×2 compared to 32×32).

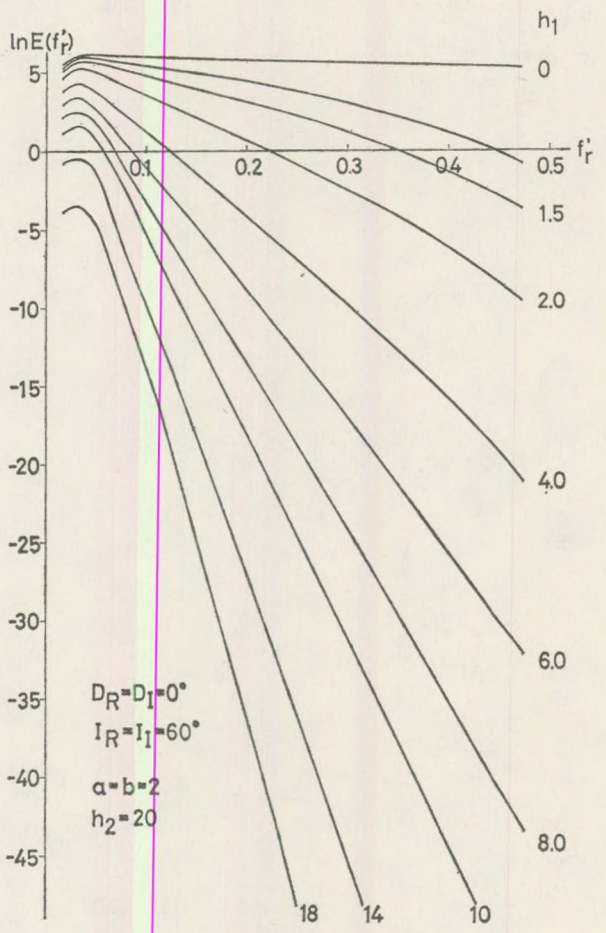

Fig. 5. Logarithmic radial spectra of magnetic fields (total filed) due to prisms, illustrating the effect of depth to the top of the bodies. Parameters are indicated. Map window is 32×32

The disturbing effects of larger horizontal dimensions could be evaluated by *Figs. 6 and 7*.

In *Fig. 6* logarithmic power spectra due to vertically infinite prisms with tops at 2 grid units are shown for various horizontal cross sections $a = b = 0.5, 1, 2, 4, 6, 8$ and 10. *Fig. 7* depicts logarithmic spectra for the same parameters except that now bottom is at 20 grid units. Doubled dashed lines in both figures indicate the direction of the linear term $-4\pi h f_r$. As it can be seen the increasing horizontal size tapers the spectra toward higher wavenumbers, i. e. it makes the slope steeper. Thus depth estimates derived from logarithmic spectra of bodies with large horizontal dimensions (large is understood again as compared to the size of the map) are too large. The influence, however, does not seen serious until $a \leq 2$.

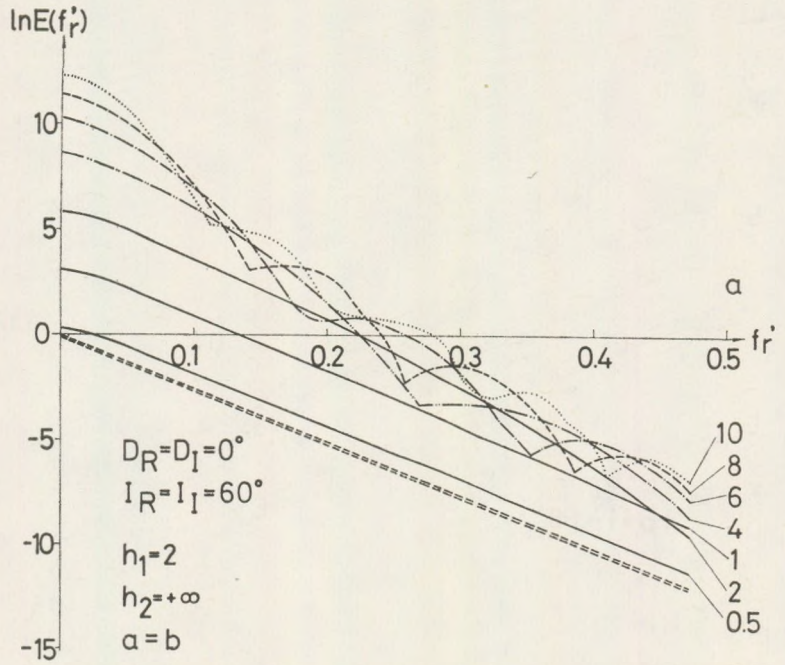

Fig. 6. Logarithmic radial spectra of magnetic fields (total field) due to prisms, illustrating the effect of horizontal dimensions. Numbers at the end of the curves indicate the values a = b. Doubled dashed line shows the dominating term $-4\pi h_1 f_r$

The effect of the depth extent is appreciable only, when both h and $t = h_2 - h_1$ are small. Let us consider the last two factors in equation (7),

$$g(h, t, f_r) = e^{-4\pi h f_r}(1 - e^{-2\pi t f_r})^2.$$

The product has a maximum, where

$$\frac{\partial g}{\partial f_r} = 0$$

which leads to the equation

$$2\pi t f_r = \ln\left(\frac{t}{h} + 1\right)$$

and it gives for the position of the maximum

$$(f_r)_{\max} = \frac{1}{2\pi t} \ln\left(\frac{t}{h} + 1\right). \tag{10}$$

The radial power spectrum and correspondingly the logarithmic power spectrum may posess a maximum. *Table 1* summarizes the $(f_r)_{\max}$ for some values of the parameters t and h. When t is small enough the combined effect

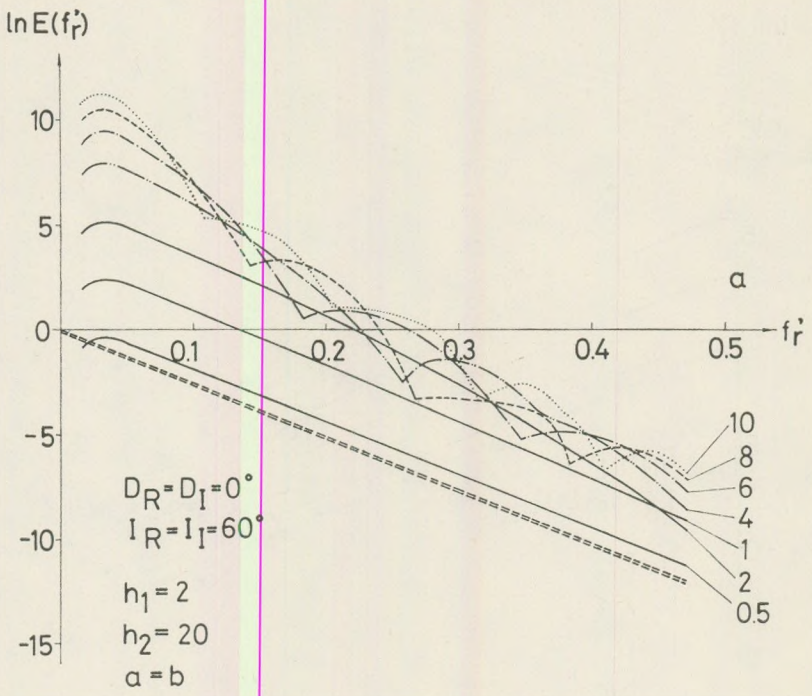

Fig. 7. Logarithmic radial spectra of magnetic fields (total field) due to prisms, illustrating the effect of horizontal dimensions. Numbers at the end of the curves indicate the values $a = b$. Doubled dashed line shows the dominating term $-4\pi h_1 f_r$

of t and h gives a pronounced peak in the logarithmic spectrum. With increasing t, however, the peak shifts toward smaller frequencies. We always deal with a finite number of data therefore when t becomes large the maximum can not be seen at all. The spectrum lines are at $(k/n;\ 1/M)$ $k = 0, \pm 1, \pm 2, \ldots, N/2$, $l = 0, \pm 1, \pm 2, \ldots, \pm M/2$ where N and M denote the dimensions of the map given in grid units therefore $(f_r)_{max}$. min $(1/N, 1/M)$ can not be seen. In *Table 1* (lower part) we also give the smallest $(f_r)_{max}$ which possibly can be detected for some reasonable number of data.

Finite vertical size is illustrated by *Figures 8, 9 and 10* for some realistic values of the parameters.

In *Fig. 8* $t = 0.1$ and $h_1 = 0$, 0.5, 1.5, 2.0, 2.5, 4, 6 and 8. In *Fig. 9* $t = 0.4$ and $h = 0$, 0.5, 1.0, 1.5, 2.0, 2.5, 3, 3.5, 4 and in *Fig. 10* $t = 1.0$, and $h = 0, 0.2, 0.4, 0.6, 0.8, 1.0, 1.2, 1.4, \ldots, 3.0$. The horizontal dimensions are for all the depicted cases $a = b = 2$.

The places of the maxima computed from (10) and observed in the logarithmic spectra can be compared in *Table 2*.

Table 1.

The position of the spectral peak $(f_r)_{max}$ for some values of 5 (depth of the top) and t (depth extent) 5 and t are given in km, f_r in $(km)^{-1}$ units

h / t	0.1	0.2	0.5	1.0	2.0	3.0	4.0	5.0	10.0
0.1	1.103	.645	.290	.152	.0776	.0522	.0393	.0315	.0158
0.2	.874	.552	.268	.145	.0758	.0514	.0388	.0312	.0158
0.25	.789	.516	.258	142	.0750	.0510	.0386	.0311	.0157
0.3	.735	.486	.249	.139	.0741	.0506	.0384	.0309	.0157
0.4	.640	.437	.234	.134	.0725	.0498	.0397	.0306	.0156
0.5	.570	.399	.221	.129	.0710	.0491	.0375	.0303	.0155
0,75	.454	.331	.194	.119	.0676	.0474	.0365	.0297	.0153
1.0	.382	.285	.175	.110	.0645	.0458	.0355	.0290	.0152
2.0	.272	.191	.128	.087	.0586	.0460	.0323	.0268	.0145
3.0	.182	.147	.103	.074	.0486	.0368	.0297	.0249	.0139
4.0	.148	.121	.087	.064	.0437	.0337	.0267	.0234	.0134
5.0	.125	.104	.076	.057	.0399	.0312	.0258	.0221	.0129
6.0	.109	.091	.068	.052	.0368	.0291	.0243	.0209	.0125
7.0	.097	.081	.062	.047	.0324	.0274	.0230	.0199	.0121
8.0	.087	.074	.056	.044	.0320	.0258	.0219	.0190	.0117
9.0	.080	.068	.052	.041	.0310	.0245	.0208	.0182	.0114
10.0	.073	.063	.048	.038	.0285	.0233	.0199	.0175	.0110
15.0	.053	.046	.036	.029	.0227	.0190	.0165	.0147	.0097
20.0	.042	.037	.303	.024	.0191	.0162	.0143	.0128	.0087
25.0	.035	.031	.025	.021	.0166	.0142	.0126	.0114	.0080
30.0	.030	.027	.022	.018	.0147	.0127	.0114	.0103	.0074

The smallest $(f_r)_{max}$ (in km^{-1}) which can be detected when number of data is $N \times N$ and grid spacing is s

s / N	0.5 km	1 km	2 km	5 km	10 km
16	0.1250	0.0625	0.0313	0.0125	0.0063
32	0.0625	0.0313	0.0156	0.0063	0.0031
48	0.0417	0.0283	0.0104	0.0042	0.0021
64	0.0313	0.0156	0.0078	0.0031	0.0016
128	0.0156	0.0078	0.0039	0.0016	0.0008
256	0.0078	0.0099	0.0020	0.0008	0.0004

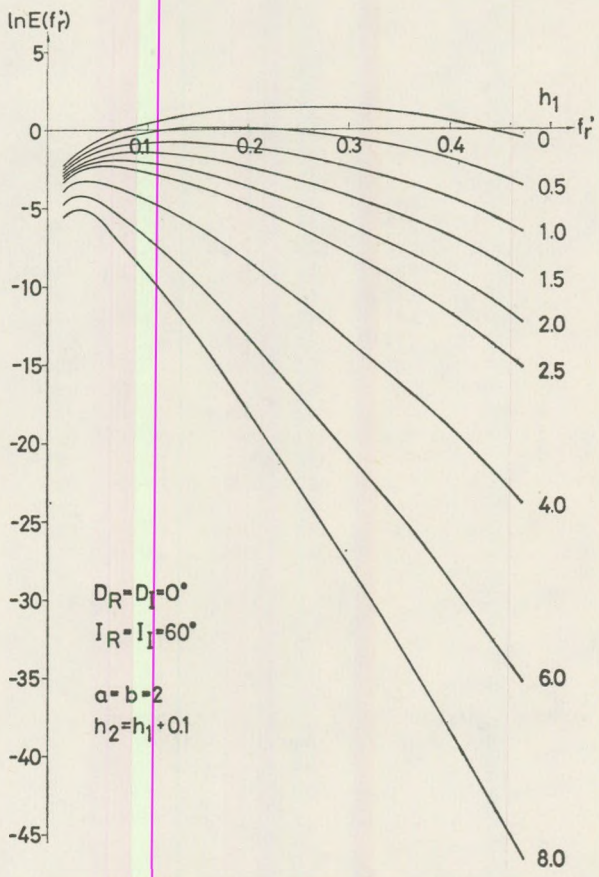

Fig. 8. Logarithmic radial spectra illustrating the effect of finite vertical size, $t = 0.1$ i.e. all cases correspond to very thin layers. Other parameters are indicated

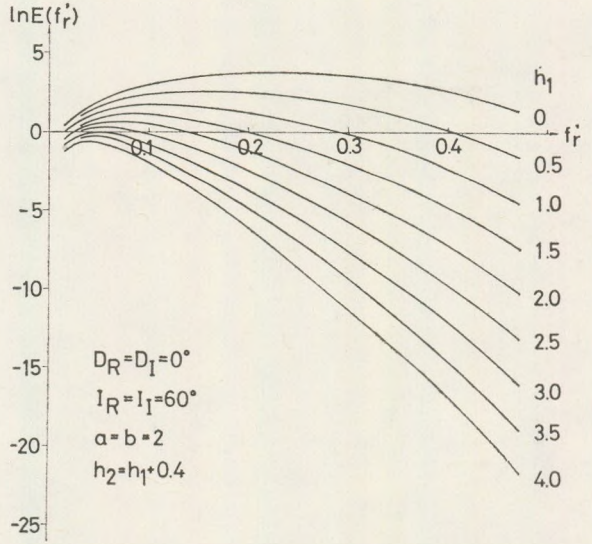

Fig. 9. Logarithmic radial spectra illustrating the effect of finite vertical size. $t = 0.4$, other parameters are indicated

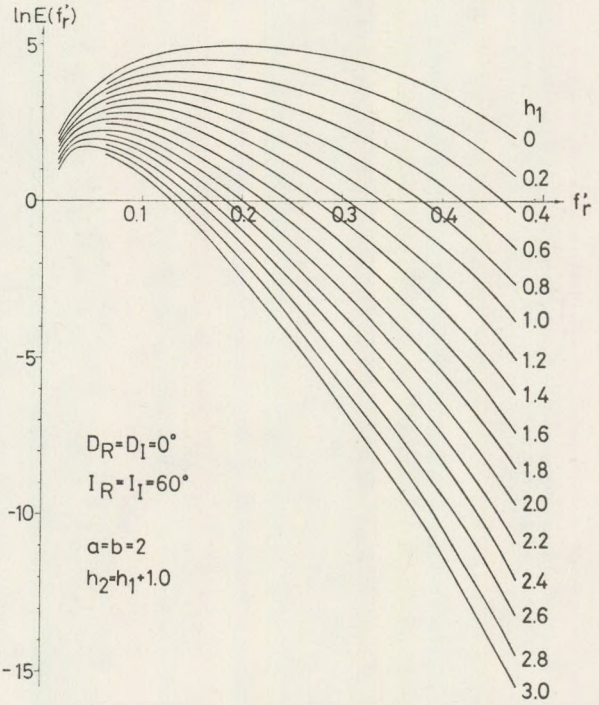

Fig. 10. Logarithmic radial spectra illustrating the effect of finite vertical size, $t = 1.0$, other parameters are indicated

Table II.

Position of the spectral peak computed from the approximation of Eq(10) compared to the position of spectral peaks in the spectra of model bodies. The spectra ln $E(f_r')$ are shown in Figs. 8, 9 and 10 respectively

$a = b = 2$ h_1	$t = 0.1$ h_2	approximate $(f_r')_{max}$ (Eq. 10)	model
0.5	0.6	0.2902	0.1717
1.0	1.1	0.1517	0.1231
1.5	1.6	0.1027	0.0934
2.0	2.1	0.0777	0.0717
2.5	2.6	0.0624	0.0629
4.0	4.1	0.0393	0.0371

$a = b = 2$ h_1	$t = 0,.4$ h_2	approximate $(f_r')_{max}$ (Eq. 10)	model
0.5	0.9	0.2339	0.1562
1.0	1.4	0.1339	0.1125
1.5	1.9	0.0941	0.0872
2.0	2.4	0.0725	0.0645
2.5	2.9	0.0591	0.0605
3.0	3.4	0.0498	0.0468
3.5	3.9	0.0431	0.0380
4.0	4.4	0.0379	0.0269

$a = b = 2$ h_1	$t = 1$ h_2	approximate $(f_r')_{max}$ (Eq. 10)	model
0.2	1.2	0.2852	0.1630
0.4	1.4	0.1994	0.1404
0.6	1.6	0.1561	0.1240
0.8	1.8	0.1291	0.1031
1.0	2.0	0.1103	0.0973
1.2	2.2	0.0965	0.0890
1.4	2.4	0.0858	0.0791
1.6	2.6	0.0773	0.0706
1.8	2.8	0.0703	0.0673
2.0	3.0	0.0645	0.0642
3.0	4.0	0.0458	0.0387

Power density spectra of randomly distributed prisms

Let us consider now the power spectrum of several prismatic bodies. The Fourier spectrum of the magnetic field due to the bodies is

$$G(f_x,\ f_y) = \sum_{i=1}^{n} G_i(f_x,\ f_y)\, e^{-j2\pi(f_x x_i + f_y y_i)}$$

where $G_i(f_x, f_y)$ denotes the spectrum of the ith prism and $(x_i,\ y_i)$ denotes the center of the ith prism (n is the number of prisms).

The power spectrum as the squared modulus of $G_i(f_x, f_y)$ becomes

$$E(f_x,\ f_y) = |G(f_x,\ f_y)|^2 = \sum_{i=1}^{n} |G_i(f_x,\ f_y)|^2 + \sum_{i=1}^{n} \sum_{\substack{k=1 \\ i \neq k}}^{n} H_i^r(f_x,\ f_y)\, H_k^n(f_x,\ f_y) +$$

$$+ \sum_{i=1}^{n} \sum_{\substack{k=1 \\ i \neq k}}^{n} H_i^{im}(f_x,\ f_y)\, H_i^{im}(f_x,\ f_y)$$

where $H_i^r\,(f_x, f_y)$ and $H_i^{im}\,(f_x, f_y)$ are abbreviations for

$$H_i^r(f_x,\ f_y) = G_i^r(f_x,\ f_y) \cos 2\pi(f_x x_i + f_y y_i) + G_i^{im}(f_x,\ f_y) \sin 2\pi(f_x x_i + f_y y_i)$$

and

$$H_i^{im}(f_x,\ f_y) = -G_i^r(f_x, f_y) \sin 2\pi(f_x x_i + f_y y_i) + G_i^{im}(f_x, f_y) \cos 2\pi(f_x x_i + f_y y_i).$$

If the centers $(x_i,\ y_i)$ are randomly distributed the cross-products cancel each other or at least their contribution becomes negligibly small compared to the dominating term, i. e. compared to the sum of the power spectra due to individual prisms. This assumption fails when the number of prisms is small or there is some regularity in their distribution. Keeping this restriction in mind we proceed with the (approximate) equation

$$E(f_r) = \sum_{i=1}^{n} E_i(f_r) \equiv \sum_{i=1}^{n} E(a_i,\ b_i,\ h_i,\ t_i,\ f_r). \tag{11}$$

Let us assume next that the parameters of the prisms are not arbitrary but follow some probability distribution. The sum may be replaced by the ensemble average multiplied by the number of prisms. The ensemble average, in turn, can be evaluated if we assume that the parameters are independent and we assign to each of them some probability distribution.

The joint probability density function, including all parameters becomes a product of probability density functions each containing one parameter, only

$$Pr(a,\ b,\ t,\ h,\ \ldots) = Pr(a)\, Pr(b)\, Pr(t)\, Pr(h)\ \ldots$$

when the parameters are independent.

A further assumption may be that the average values of the inclination and the declination of the magnetic moment vector, do not differ significantly from the inclination and declination of the geomagnetic field. It involves that magnetization is essentially induced. This can be verified by the shape of individual anomalies. When the assumption seems to be justified we can write for the expected values

$$\mathcal{E}\{R_T^2(\alpha)\} = \mathcal{E}\{R_M^2(\alpha)\}.$$

The probability distribution of the other parameters can not be deduced from the data and various assumptions have to be made concerning the shape of the distributions.

E. g. Spector and Grant (1970) assumed uniform distributions for all parameters. Other distributions e. g. Gaussian distribution may also be used.

The expected value of the power density spectrum becomes

$$\mathcal{E}\{E(f_r, \alpha)\} = \int \ldots \int E(f_r, \alpha)\, Pr(a)\, Pr(b) \qquad da\, db \ldots$$

Due to the simple structure of the assumed joint probability distribution the multiple integral can be factored into a product of integrals, each containing the contributions of some characteristic parameters

$$\mathcal{E}\{E(f_r\, \alpha)\} = 4\pi^2\, \bar{k}\, \mathcal{E}\{e^{-4\pi h f_r}\} \cdot \mathcal{E}\{(1 - e^{-2\pi t f_r})^2\} \cdot$$
$$\cdot\, \mathcal{E}\{S^2(f_r, a)\}\, \mathcal{E}\{R_T^4(a)\}. \tag{12}$$

where $\bar{k}$ denotes the expected value of abm_0.

When we take the radial power spectra by averaging over the variable α the last term becomes a constant factor. After taking the logarithm the constant factors become additive constants having no bearing upon the shape of $S(f_r)$. Three terms remain containing the effects of depth, depth extent and horizontal sizes, respectively. Each term will be discussed separately.

The influence of the depth (to the top of the prism)

Assuming first that h is uniformly distributed in the interval $(\bar{h} - \Delta h, \bar{h} + \Delta h)$ the expected value is obtained as follows

$$\mathcal{E}\{e^{-4\pi h f_r}\} = \frac{1}{2\Delta h} \int_{\bar{h}+\Delta h}^{\bar{h}-\Delta h} e^{-4\pi h f_r}\, dh = \frac{1}{2\Delta h} \left[\frac{e^{-4\pi h f_r}}{-4\pi f_r} \right]_{\bar{h}-\Delta h}^{\bar{h}+\Delta h} =$$

$$= e^{-4\pi \bar{h} f_r} \frac{sh(4\pi f_r\, \Delta h)}{4\pi f_r\, \Delta h}. \tag{13}$$

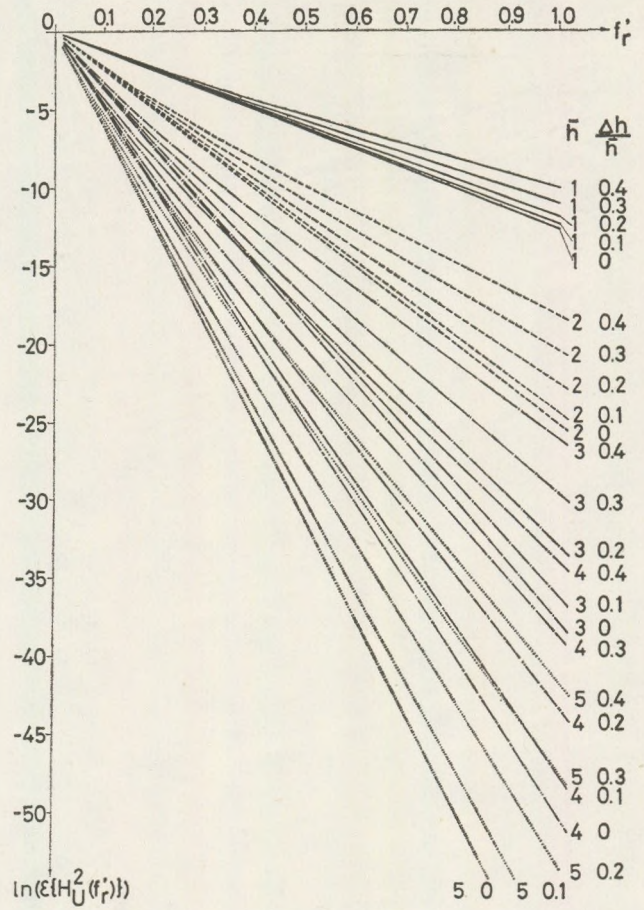

Fig. 11. The expected value of the dominating term $(-4\pi h f_r)$ if h follows a uniform distribution with expected value h and length Δh

The first factor dominate when $4\,\pi f_r\,\Delta h$ is sufficiently small. The effect of the length of the distribution can be estimated from *Fig. 11* which shows the logarithm of (13) for the average depths $\bar{h} = 1, 2, \ldots, 5$ and relative lengths $(\Delta h/\bar{h})$ of the uniform distribution $\Delta h/\bar{h} = 0.0,\ 0.1,\ 0.2,\ 0.3$ and 0.4.

Let us assume next that the probability of h is Gaussin with the parameters $(\bar{h}, \sigma)$. The expected value of the factor $\exp(-4\,\pi h f_r)$ then becomes

$$\mathcal{E}\{e^{-4\pi h f_r}\} = \frac{1}{\sqrt{2\pi}\,\sigma} \int_{-\infty}^{+\infty} e^{-4\pi h f_r}\, e^{-(h-\bar{h})^2/2\sigma^2}\, dh = e^{-4\pi \bar{h} f_r + 8\pi^2 \sigma^2 f_r^2}. \qquad (14)$$

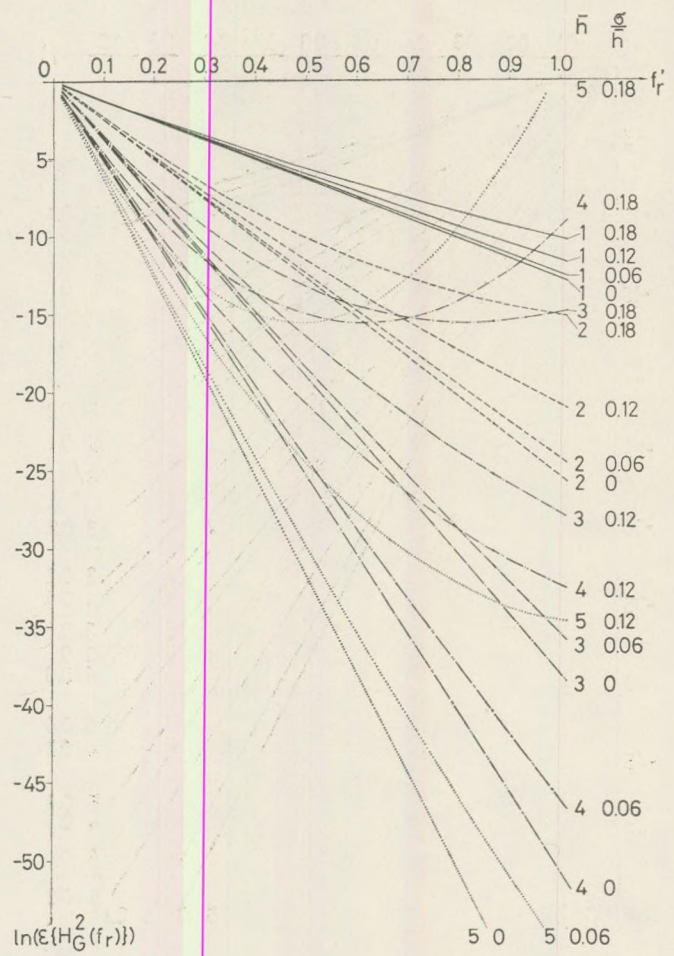

Fig. 12. The expected value of the dominating term $(-4\pi h f_r)$ if h follows a normal distribution with expected value h and standard deviation σ

The logarithm of the expected value contains now a parabolically increasing term $8\pi^2\sigma^2 f_r^2$ besides the linearly decreasing $-4\pi\bar{h}f_r$. Its effect is, again, negligible until σ remains sufficiently small. *Fig. 12* shows the logarithm of the expected value of $\exp[-4\pi f_r h]$ for some values of the parameters $\bar{h}$ and $\sigma/\bar{h}$.

The effect of the depth extent

The second factor, containing the variable t can be similarly evaluated. We obtain for $\mathcal{E}\{(1-e^{-2\pi i f_r})\}$ with the uniform distribution

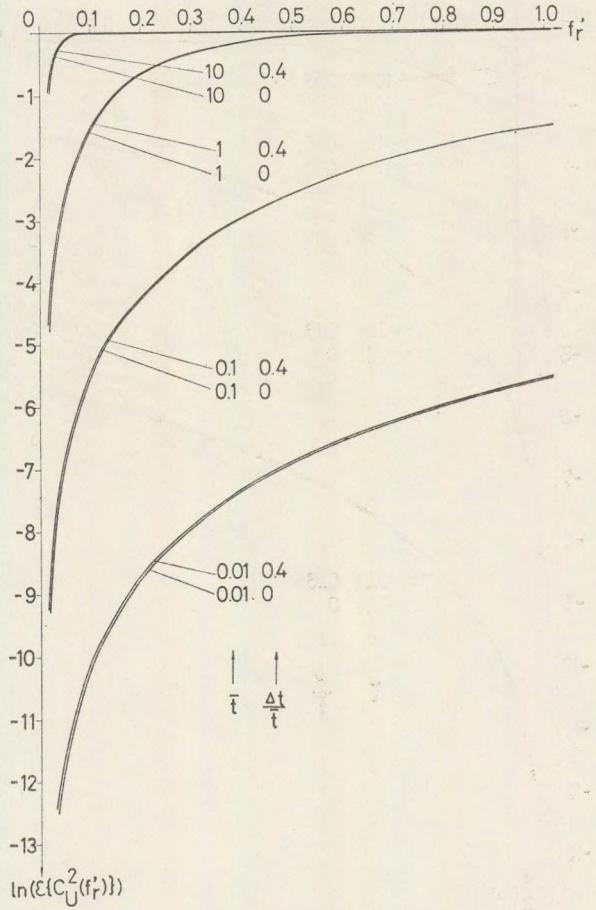

Fig. 13. The expected value of the term describing the effect of depth extent if t follows a uniform distribution with expected value t and length Δt

$$\mathcal{E}\{(1-e^{-2\pi t f_r})^2\} \equiv \mathcal{E}\{C_u^2(f_r)\} = \frac{1}{2\Delta t}\int_{\bar{t}+\Delta t}^{\bar{t}-\Delta t}(1-2e^{-2\pi t f_r}+e^{-4\pi t f_r})\,dt =$$

$$= 1-e^{-2\pi \bar{t} f_r}\,\frac{sh(2\pi\,\Delta t f_r)}{\pi \Delta t f_r} + e^{-4\pi \bar{t} f_r}\,\frac{sh(4\pi\,\Delta t f_r)}{4\pi\,\Delta t f_r}\,. \qquad (15)$$

and for the Gaussian distribution

$$\mathcal{E}\{C_G^2(f_r)\} = 1-2e^{-2\pi \bar{t} f_r + 2\pi^2\sigma^2 f_r^2} + e^{4\pi \bar{t} f_r + 8\pi^2\sigma^2 f_r^2}\,. \qquad (16)$$

The logarithms of the functions (15) and (16) are shown in *Figs. 13 and 14*, respectively.

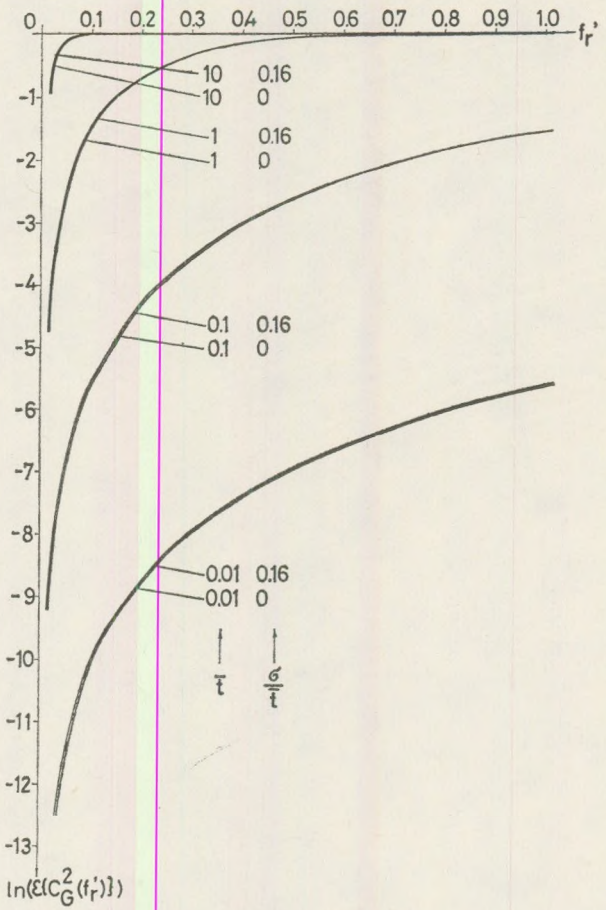

Fig. 14. The expected value of the term describing the effect of depth extent if t follows a uniform distribution with expected value t and standard deviation σ

It is worth to note, that the functions describing the depth extent hardly depend on the length of the uniform distribution Δt or on the standard deviation of the Gaussian distribution σ except for very small values of t.

Double ensembles of prismatic bodies

Let us consider last a double ensemble of prismatic bodies. When the parameters h and H (depths to the tops) in the ensembles separates well, and the distributions of the centers of bodies are random without correlation between the two ensembles the expected value of the power spectrum of the magnetic field due to all bodies can be approximated by

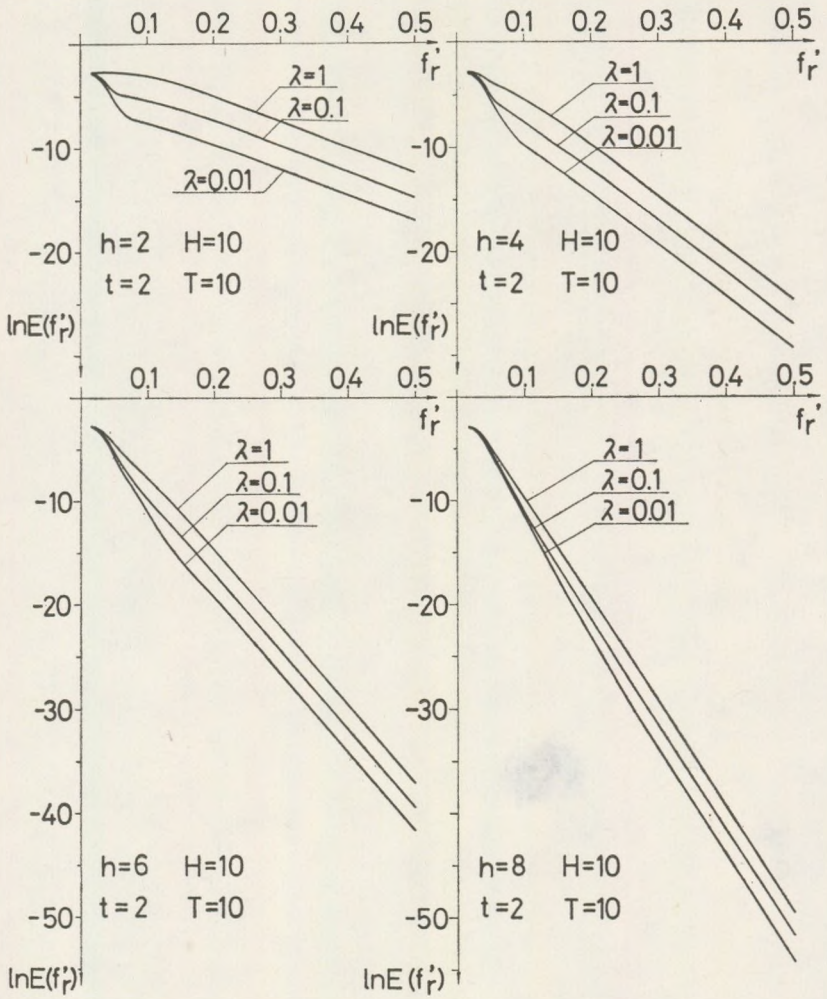

Fig. 15. Logarithmic power spectra for some double ensembles of magnetized bodies. Fixed parameters are: depth extents $T = 10$ (for deeper sources) and $t = 2$ (for shallow sources) and depth of the top of the deeper sources ($H = 10$). The four sets of curves correspond to four different h (depth to top of shallower sources). In each set three energy ratios are shown 1:1, 1:10 and 1:100

$$\mathcal{E}\{E(f_r\ \alpha)\} = 4\pi^2\,\overline{K}^2\mathcal{E}\{e^{-4\pi H f_r}\}\,\mathcal{E}\{(1-e^{-2\pi T f_r})^2\}\,\mathcal{E}\{S_1^2(f_r, d)\} + \\ + 4\pi^2\,\overline{k}^2\mathcal{E}\{e^{-4\pi h f_r}\}\,\mathcal{E}\{(1-e^{-2\pi t f_r})^2\}\,\mathcal{E}\{S_2^2(f_r, \alpha)\} \qquad (17)$$

where K, H, T and k, h, t denotes the expected value of the magnetic moment/unit depth, the depth to the top, the depth extent of the first and the second ensembles of bodies, respectively.

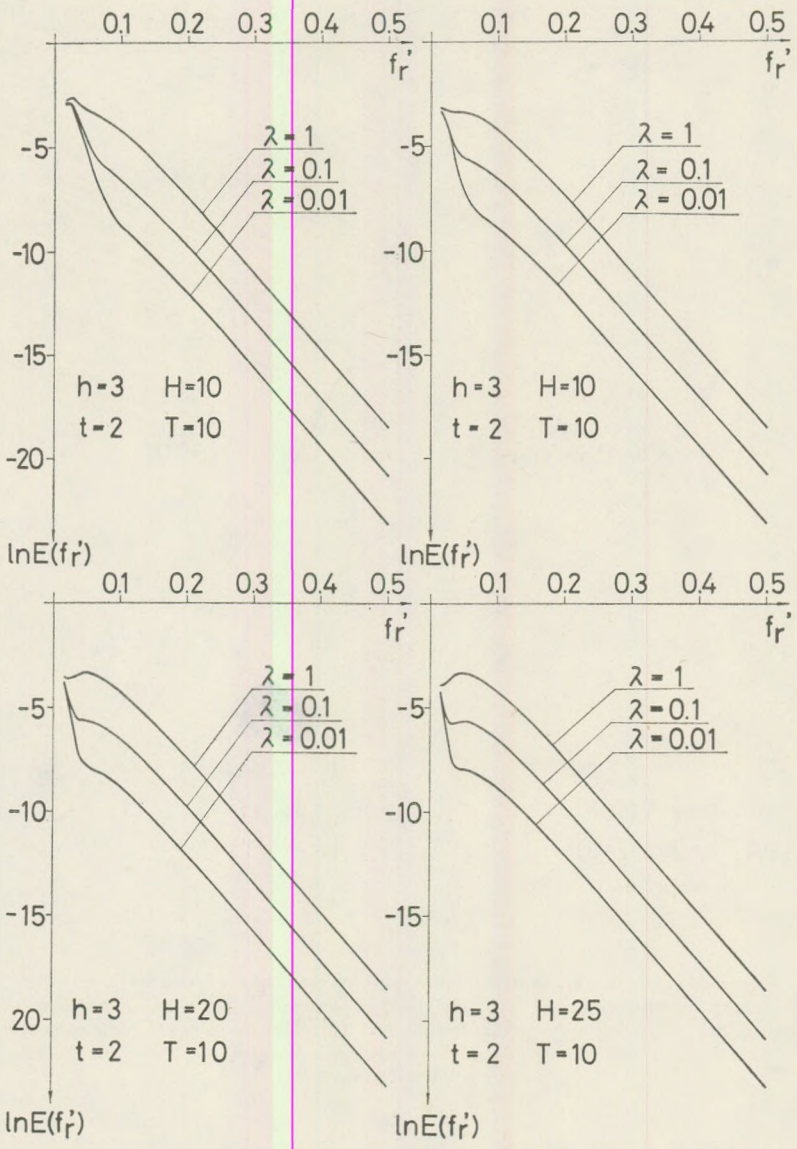

Fig. 16. Logarithmic power spectra for some double ensembles of magnetized bodies. Fixed parameters are: depth extents $T = 10$ (for deeper sources) and $t = 2$ (for shallow sources) and depth of the top of the shallower sources ($h = 3$). The four sets of curves correspond to four different H (depth to top of deeper sources). In each set three energy ratios are shown 1:1, 1:10 and 1:100

$\mathcal{E}\{S_1^2(f_r, a)\}$ and $\mathcal{E}\{S_2^2(f_r a)\}$ contain the effects of the horizontal sizes for the ensembles. In order to get an impression of the behaviour of this rather complicated expression let us assume that $\overline{K}^2 = (\lambda \overline{k})^2\, \mathcal{E}(S_1^2(f_r, \alpha)\} = \mathcal{E}\{S_2^2(f_r, \alpha)\}$ and the parameters H, T, h and t are deterministic. Then (17) simplifies to

$$E_r(f_r) = C[\lambda^2 e^{-4\pi H f_r}(1 - e^{-2\pi T f_r})^2 + e^{-4\pi h f r}(1 - e^{-2\pi t f_r})^2]. \qquad (18)$$

Figures 15 and 16 show the logarithm of the radial power spectra for some realistic combinations of the parameters λ, H, T, h and t. In *Fig. 15* $H = 10, T = 10, t = 2$ and h varies, while in *Fig. 16* $h = 3, t = 2, T = 10$ and H varies. Both cases are depicted for three different values of the parameter λ.

The most important conclusion which can be drawn from the sets of curves is, that the contribution of the deeper ensemble very rapidly disappears with increasing f_r, i.e. in the estimation of the depth of the deeper sources the first few spectral lines can be used, only. The second conclusion is that t could be determined very rarely and the peak caused by the limited extent of the deeper sources (T) appears at very small frequencies, thus it could be observed very rarely in the spectra of real magnetic data.

REFERENCES

Andreasen, G. E., Zietz, I., 1969: Magnetic fields for 4×6 prismatic model, Geological Survey, Professional Paper 666.

Bhattacharyya, B. K., 1965: Two-dimensional harmonic analysis as a tool for magnetic interpretation, Geophysics, Vol. 30, pp. 829–857.

Bhattacharyya, B. K., 1966: Continuous spectrum of the total magnetic field anomaly due to a rectangular prismatic body, Geophysics, Vol. 31, pp. 97–121.

Bhattacharyya, B. K., 1971: Analysis of a vertical dike, infinitely deep, striking north by Fourier transform, Pure and Applied Geophysics, 89, pp. 134–138.

Bhattacharyya, B. K., Lei-Kuang Leu, 1975: Analysis of magnetic anomalies over Yellowstone National Park: Mapping of Curie point isothermal surface for geothermal reconaissance, Journal of Geophysical Research, Vol. 80, No. 32, pp. 4461–4465.

Cianciara, B., Marcak, H., 1976: Interpretation of gravity anomalies by means of local power spectra, Geophysical Prospecting, Vol. 24, pp. 273–286.

Hahn, A., Kind, E. G., Mishra, D. C., 1976: Depth estimation of magnetic sources by means of Fourier amplitude spectra, Geophysical Prospecting, Vol. 24, pp. 287–308.

Kis, K., Meskó, A., 1977: Application of the Logarithmic Power Spectrum in the Interpretation of Magnetic Data Contributions of the XXII International Geophysical Symp., Prague (in press).

Lehmann, M. J., 1970: Examples for the separation of fields of magnetic sources in different depths by harmonic analysis method, Boll. Geofis. Teor. Appl. 12: 97–117.

Naidu, P. S., 1970: Statistical structure of aeromagnetic field, Geophysics, Vol. 35, pp. 279–292.

Odegard, M. E., Berg, J. W., 1965: Gravity interpretation using the Fourier integral, Geophysics, Vol. 30, pp. 424–438.

Peters, L. J., 1949: The direct approach to magnetic interpretation and its practical application, Geophysics, Vol. 14, 290–320.

Sengupta, S., Das, S., 1977: Interpretation of the gravitational effect of two-dimensional dike by Fourier transform, Geoexploration, Vol. 15, pp. 251–261.

Spector, A., Bhattacharyya, B. K., 1966: Energy density spectra and autocorrelation functions due to simple magnetic models, Geophysical Prospecting, Vol. 14, pp. 242–272.

Spector, A., Grant, F. S., 1970: Statistical models for interpreting aeromagnetic data, Geophysics, Vol. 35, pp. 293–302.

Steeland, N. C., 1962: Gravity and Aeromagnetic Exploration in the Paradox Basin, Geophysics, Vol. 17, pp. 73–89.

Syberg, F. J. R., 1972: A Fourier method for the regional-residual problem of potential fields, Geophysical Prospecting, Vol. 20, pp. 47–75.

Vacquier, V., Steeland, N. C., Henderson, R. G., Zeitz, I., 1971: Interpretation of aeromagnetic maps, Geol. Soc. Am., Memoir, 47.

INVESTIGATIONS ON THE ENERGY BALANCE OF THE ATMOSPHERE

MAKAI CSÁSZÁR M.

Department of Meteorology, Eötvös University, Budapest

(Received 1 Sept. 1977)

РЕЗЮМЕ

В работе проведено исследование энергетических условий ограниченного пространства атмосферы, пригодного для исследования синоптических процессов. Были оценены польная потенциальная и кинетическая энергия исследуемого диапазона а также и та потенциальная энергия которой владеет кинетическая энергия и которая может преобразоваться в нее. Были определены соотношения отдельных видов энергии к кинетической и эти соотношения сравнивались с теми, которые характеризуют атмосферу в глобальном масштабе. Высшеупомянутые соотношения оказались больше соответствующих глобальных значений, и это объясняется тем, что в исследуемом отрезке времени в данном диапазоне происходила интенсивная деятельность циклонов. На это указывают и величины «активности кинетической энергии» и «времени затухания»-параметров, введенных для характеристики интенсивности процессов в атмосфере. Был определен и переход резервированной потенциальной энергии в кинетическую на примере образования и развития одного средиземноморского циклона. Величины, характеризующие процессы перехода, были определены с применением детального вертикального подразделения, но в работе приводим только результаты, характеризующие процессы во всей тольщине данного диапазона. Результаты приведены в виде изображения на картах.

The intensity and stability of the general circulation depends on the equilibrium between the production and dissipation of the kinetic energy. The only source of the kinetic energy is the available potential energy, defined by L o r e n z (1955) as the deviation between the total potential energies of the natural state of the atmosphere and of a reference state formed in the course of an adiabatic rearrangement of the air masses, (total potential energy = gravitational potential energy + internal energy + latent energy). By the introduction of this concept Lorenz gave the connection between the driving mechanism and the atmospheric energy cycle. In viscous fluids part of the mechanical energy dissipates into heat and this process leads to a gradual loss of the kinetic energy. Thus there must be a continuous energy production, if we want that the kinetic energy should be maintained. The mean order of magnitude of energy transformation is known, but we have very few knowledge of the extent of connection between the parameters of friction and macrosynoptical flow.

According the estimation of Lorenz the ration of the average available potential energy of the Earth and of the total potential energy is 1/200, that of the kinetic energy and of the available potential energy is 1/10. But

because the total potential energy of the atmosphere exceeds well the kinetic energy of it – the order of which is 1/2000 –, when investigating the ration between production and dissipation of the kinetic energy it is practical to compare the kinetic energy with the available potential energy. If we represent the summed up values of the potential, internal and latent energy for a given atmospheric domain, we know only the energy store of the domain. Such a representation has no significance in itself, but it plays an accentuated role in case of an investigation of the general circulation processes, when we want to know, which regions of the Earth possess a big energy store and where can we find the deficient domains. In this sense, namely, the unevenly distributed energy content may be handled as a katalitic effect producing primarily available energy and stimulating the atmosphere towards movements in order to solve the contradiction being inherent is the differences of non-adiabatic warmings up. The mobility represented by the total energy store of a domain can be estimated only by a comparison with other domains. According to the computations of Dutton and Johnson (1969) the total potential energy can be estimated in the summer months to $2.58 \cdot 10^{12}$ ergcm^{-2}, while in the winter months we have an estimated amount of $2.51 \cdot 10^{12}$ ergcm^{-2}. At the same time the available potential energy in the winter months was estimated to $4.46 \cdot 10^{9}$ ergcm^{-2}, while in the summer monthy it amounted only to $1.57 \cdot 10^{9}$ ergcm^{-2}. Though we have the total potential energy at our disposal, owing to the above considerations we will pay attention only to the connection between the available potential energy and the production and dissipation of the kinetic energy.

In a previous study we investigated the role of the efficiency factor and the non-adiabatic heating between 00 GMT on the 19th October 1970 and 12 GMT on the 21th, when in the course of a slow eastwards shifting of a large North-Europian cyclone and its filling up a cyclone of smaller dimension appeared over the Mediterranean and later over the Europian territory of the Soviet Union. Our energy-calculations were made also on the basis of the said time interval, but owing to the largeness of the material we will show the detailed results only in the characteristical phases of development of the Mediterranean cyclone.

The kinetic energy of the domain of x area S lying between the pressure levels p_1 and p_2 can be given by the formula

$$K = \frac{1}{g} \int_S \int_{p_2}^{p_1} \frac{u^2 + v^2}{2} \, dp \, dS, \tag{1}$$

its potential energy by the expression

$$\Phi = \frac{1}{g} \int_S \left[\int_{p_2}^{p_1} RT \, dp + p_1 z_1 - p_2 z_2 \right] dS, \tag{2}$$

its internal energy is

$$I = \frac{1}{g} \int_S \int_{p_2}^{p_1} c_v T \, dp \, dS , \tag{3}$$

its latent energy reads as

$$L = \frac{1}{g} \int_S \int_{p_2}^{p_1} Hq \, dp \, dS , \tag{4}$$

and finally the available potential energy can be given, as

$$A = \int_S \frac{1}{g} \int_{p_2}^{p_1} c_p \Theta \frac{p^\varkappa - p_r^\varkappa}{p_{00}^\varkappa} dp \, dS , \tag{5}$$

where u and v are the horizontal components of the wind velocity V, g is the gravity acceleration, T is the temperature, Θ the potential temperature, c_v the specific heat at a constant volume, q is the specific humidity, H is heat of condensation, p is the pressure, $p_{00} = 1000$ mb, p_r is the so called reference pressure belonging to the potential temperature assumed by the isentropic surfaces after the rearrangement, $k = R/c_p$, R is the gas constant and c_p is the specific heat at constant pressure.

The total energy content of the domain can be seen is Table I. The comparison with the global energy store directs our attention to a few important facts. According to the data of the Table the greatest variability is represented by the latent energy. The average kinetic energy is $21{,}1 \cdot 10^5$ joule m^{-2}, somewhat greater, than the global yearly mean. Holopainen (1963) obtained for the mean kinetic energy of the layer below 200 mb the value: $23{,}6 \cdot 10^5$ joule m^{-2}, Smith (1969) got: $11.75 \cdot 10^5$ joule m^{-2}, Oort (1964) gave: $15 \cdot 10^5$ joul m^{-2} Taking into account the fact that during the time interval under investigation an intensive cyclonic activity took place in our domain, the obtained value of $21\,1 \cdot 10^5$ joule m^{-2} does not seem as an exaggerated one. The date of the above authors refer only to average time conditions, in the actual daily values we have to calculate with great and significant oscillations. E.g. Danard (1964) obtained for the value of the kinetic energy of an intensive cyclone $33.4 \cdot 10^5$ joule m^{-2}. He carried out his computations for a domain of area $10.5 \cdot 10^{12}$ m^2, which is comparable with the conditions of the domain of area $15.41 \cdot 10^{12}$ m^2 studied by us.

The variation of the potential energy oscillated between $4.5 \cdot 10^{10}$ and $155 \cdot 10^{10}$ kwatt, while for the latent energy the limits were: $292 \cdot 10^{10}$ resp. $2180 \cdot 10^{10}$ kwatt. It is worth while to cast a look at the ratio of the kinetic energy and of the available potential energies as compared with the other kind of energy (Table I., columns 7., 8., 9.), Although the latent energy is

Results of energetical calculations of the demain of

1	2	3	4	5	6	7	8	9
Date	$\frac{K}{10^{14}}$	$\frac{\Phi}{10^{17}}$	$\frac{I}{10^{17}}$	$\frac{L}{10^{17}}$	$\frac{A}{10^{15}}$	$\frac{K}{I+\Phi+L}$ 10^{-4}	$\frac{K}{I+\Phi}$ 10^{-4}	$\frac{K}{A}$ 10^{-2}
	K joule							
19^{00}	307,16	105,82	339,05	66,28	349,8	6,12	6,9	8,8
19^{12}	313,64	105,15	338,88	56,83	341,6	6,26	7,1	9,1
20^{00}	322,30	104,80	337,71	52,92	338,2	6,51	7,3	9,5
20^{12}	324,18	104,82	337,72	51,65	328,1	6,65	7,3	9,9
21^{00}	356,55	104,48	337,01	53,14	333,6	7,20	8,1	106
21^{12}	333,65	105,04	336,68	50,79	318,8	6,80	7,6	104
Mean value for an area of 1 m^2	21,1 10^5	68,1 10^7	219,2 10^7	37 10^7	216 10^5	6,5 10^{-4}	7,1 10^{-4}	9,7 10^{-2}
	joule m^{-2}							

about the tenth part only of the potential as well as of the internal energies, after all it plays an important role concerning the mobility of atmospheric processes. In this form we are able to characterize in order of magnitude that released energy, which from thermodynamical point of view represents a potential energy influencing drastically – in case of its release – the kinetic energy, and thus the weather too.

The mean distribution of the individual energies in joule m^{-2} units is to be seen on Fig. 1. (the value of the kinetic energy is reduced by 10^3); for the distribution of the potential energy – according to its definition – we got values increasing with height. The latent and internal energies show their highest values in the lower third part of the troposphere. The sharp decrease of the latent energy with height could be expected owing to the vertical gradient of temperature and humidity. The kinetic energy reaches its highest value on the average in the layers between 400 and 200 mb, the highest concentration, however, can be found in the layers between 350 and 250 mb.

On the Fig. 2. we find the mean variability of the individual energies. (Unit for the internal, potential and latent energies is watt m^{-2}, that for the kinetic energy: 10^{-2} watt m^{-2}). The latent energy showed its strongest variation in the near surface layer, but it had a secondary maximum in the level of cloud development (corresponding to the autumn season in

Table I.

15,4 · 10^{12} m² area reaching from the ground up to the 100 mb level

10	11	12	13	14	15	16	17	18	19
C_k 10^8	$\frac{\partial K}{\partial t}$ 10^8	$\frac{\partial \Phi}{\partial t}$ 10^8	$\frac{\partial I}{\partial t}$ 10^{10}	$\frac{\partial L}{\partial t}$ 10^{10}	$\frac{\partial A}{\partial t}$ 10^{10}	C_{ks} 10^8	D_s 10^8	K_s 10^{13}	Depletion time in the friction layer in hours
kwatt									
1390						+406,0	−333	93,1	7,8
	+149,9	−155,0	− 38,8	−2180	−18,9				
+ 589						+477,1	−303	84,2	7,4
	+200,0	− 79,0	−273,1	− 907	− 7,8				
+1060						− 95,7	−384	89,5	8,7
	+ 43,5	− 4,5	+ 2,4	− 292	−23,5				
+ 582						+359,0	−348	106,0	6,3
	+749,0	− 76,5	−162,0	+ 346	+12,7				
− 233						+466,1	−275	74,9	7,5
	−530,0	+141,0	−767,0	− 544	−34,3				
−1020						−419,1	−257	74,3	8,0
+2,5	+0,78	−22,6	−160,8	−259,2	−9,3	+1,2	−2,1	5,6 10^4 joule m^{-2}	7,6
watt m^{-2}									

the layer between 850 and 750 mb.). It is somewhat surprising that we have a similar march for the variability of the potential as well as kinetic energy in the upper part of the troposphere. When looking at the curve it seems that the troposphere obtains the kinetic energies of movements taking place in its lower part from the changes going on in the internal energy, and more precisely in the lantent energy, while the kinetic energy of the movements setting in the upper levels is due to the changes of the value of the potential energy. The kinetic energy reached its strongest variation in the vicinity of the 250 mb level, but we could observe a secondary maximum too between the layers of 850 and 750 mb. On the Fig. 2. we can well see that the change of the internal energy is of a lower order of magnitude when compared to that of the other energies, while the change of the latent energy surpasses the added values of variation taking place in the potential and internal energies. For the mean variability of the individual energies Borisz enkov (1960) has obtained similar values with the exception that he did not calculate separately the latent energy, but he took it into account in the value of the internal energy, using virtual temperature instead of the common one. As regards the detailed energy values of the domain the contribution of the latent energy to the potential energy being at the disposal of the kinetic energy represents a significant value, even in the development of the northern cyclone. It seemed that it had its part in

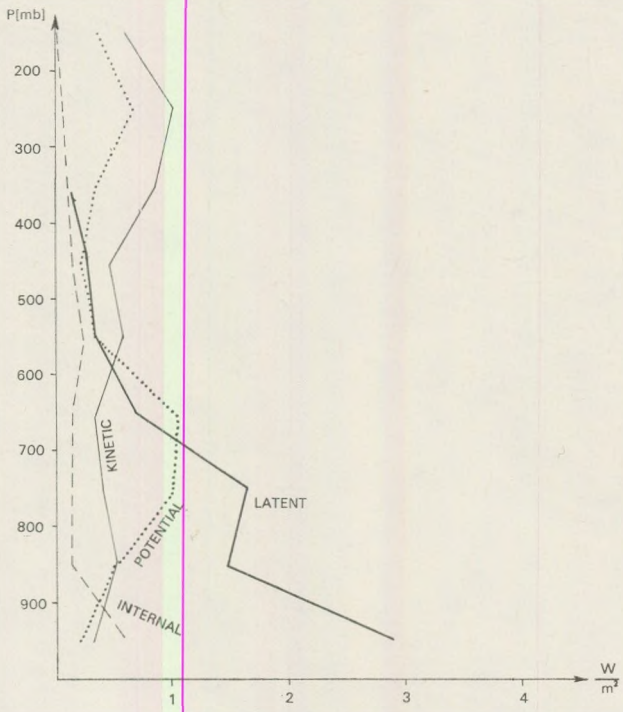

Fig. 1. Vertical distribution of the mean values of various energies: the value of the potential, internal and latent energy is given in 10^6 joule m^{-2}, that of the kinetic energy in 10^3 joule m^{-2} units.

the stability of the large cyclone, and as regards its activity, the latent energy can be taken as the primary energy source of the Mediterranean cyclone.

This supports the previous conclusion that the latent heat release can lead to a significant intensification of cyclones of middle latitudes. The first attempts for taking into account the effect of condensation on the development of cyclones have been made by S m a g o r i n s k y (1956), who found that the computed vertical velocity can be increased by an order of magnitude partly by taking into account the horizontal change of the statical stability, partly because in those domains, where latent heat release occurs, vertical velocity will be induced. The non-adiabatic contribution of the released latent heat may – in some cases – surpass the order of magnitude of the absorbed solar radiation by one or two orders of magnitude. Supposedly, the increased amount of available potential energy in the domain of the Mediterranean may be attributed also to the effect of non-adiabatic contributions connected to the latent heat variations. On the series of Figures 3. we see the changes of areal distribution of available potential and kinetic energies at 12^h on the 19th, at 00 as well as 12^h on the

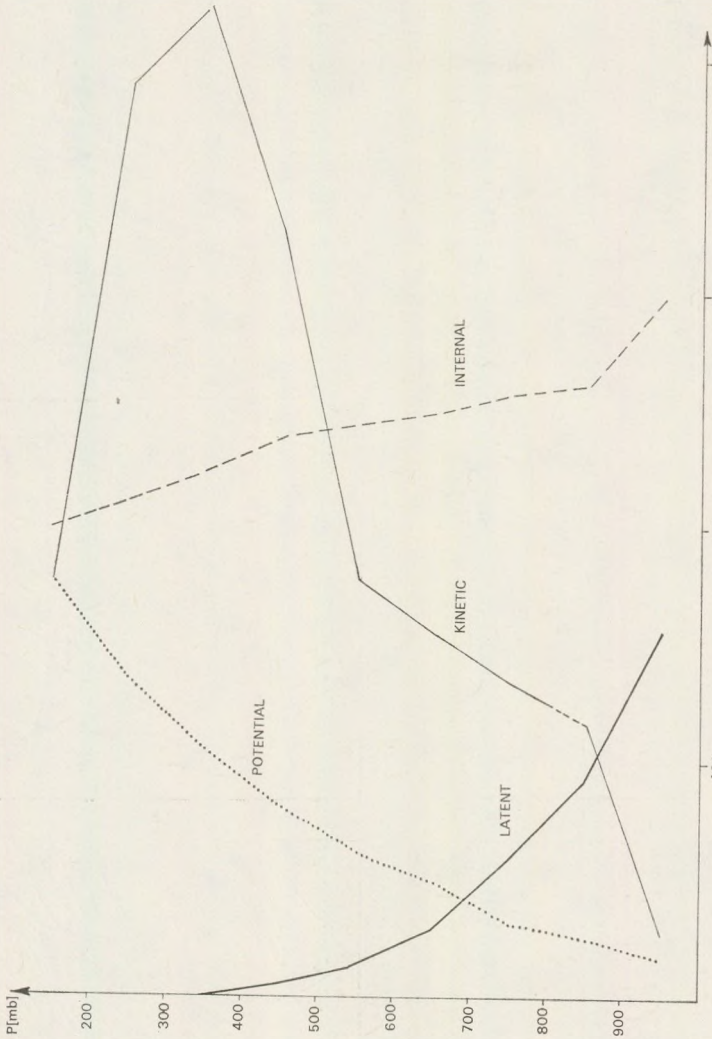

Fig. 2. Vertical distribution of mean variability of various energies: the changes of the potential, internal and latent energy in 10^2 watt m^{-2}, that of the kinetic energy in 10^{-1} watt m^{-2} units.

20 th, while on Figs 4. and 5. we show the variations taking place in the potential, internal and latent energies. The variations of the latent heat show the maximum concentration in the Mediterranen, but we can find significant values also on the area of the North-Europian cyclone too. In the indicated domains the latent heat plays a double role. On the one part it increases the non-adiabatic contribution of the available potential energy in the domains of a positive efficiency factor, while on the other part the induced rising currents within the relatively warmer air supported the conversion into kinetic energy. One can not neglect – owing to the presence of the Mediterranean-sea the contribution of the observable heat supply in

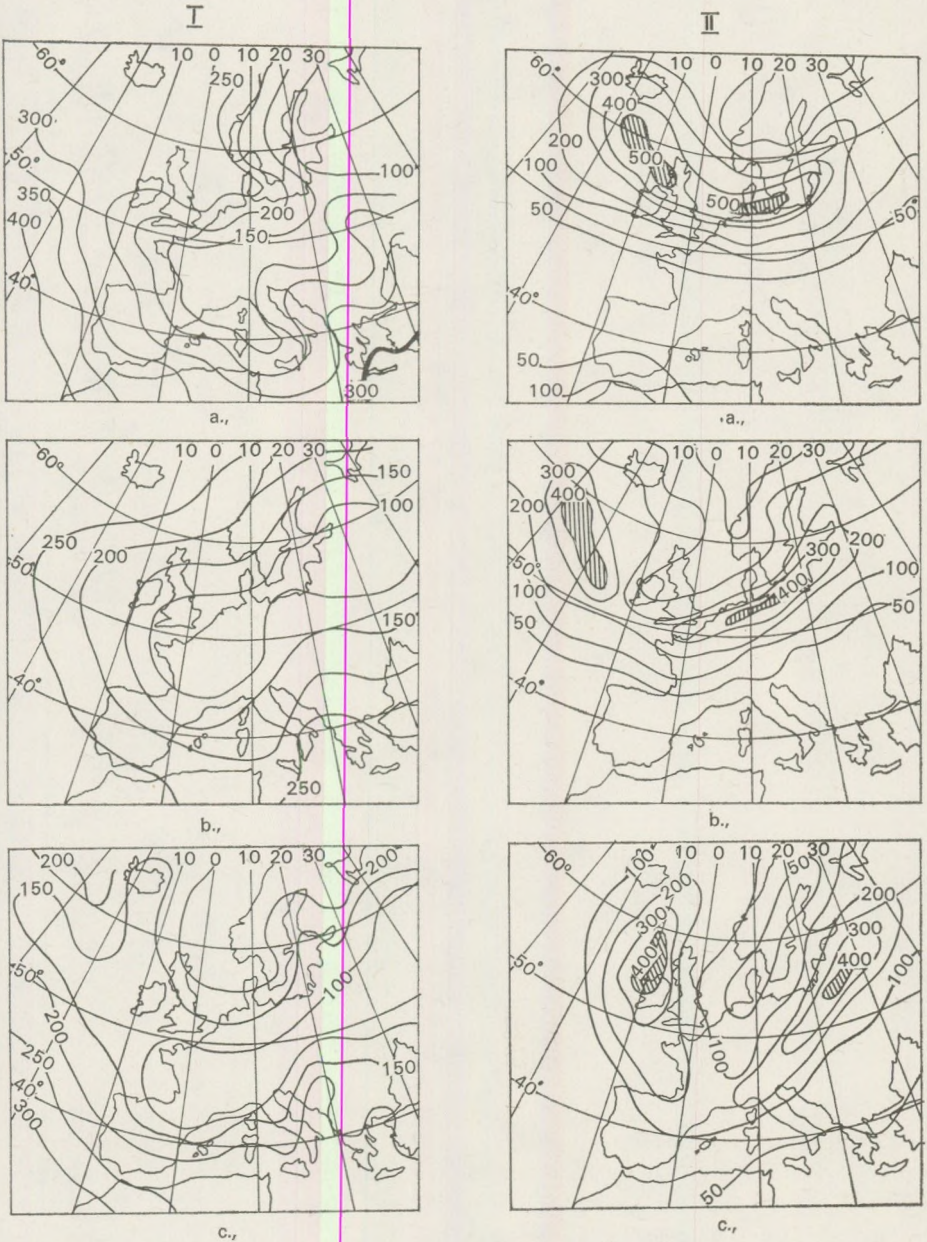

Fig. 3. Areal distribution of the I: available potential energy in 10^{13} kjoule units; and II kinetic energy in 10^{12} kjoule units. Values refer to the volume from the ground up to th 100 mb surface level over areas of 2.5 degrees of width and 2.5 degrees of length each
a) for 19th October 1970, 12 GMT,
b) for 20th October 1970, 00 GMT and
c) for 20th October 1970, 12 GMT.

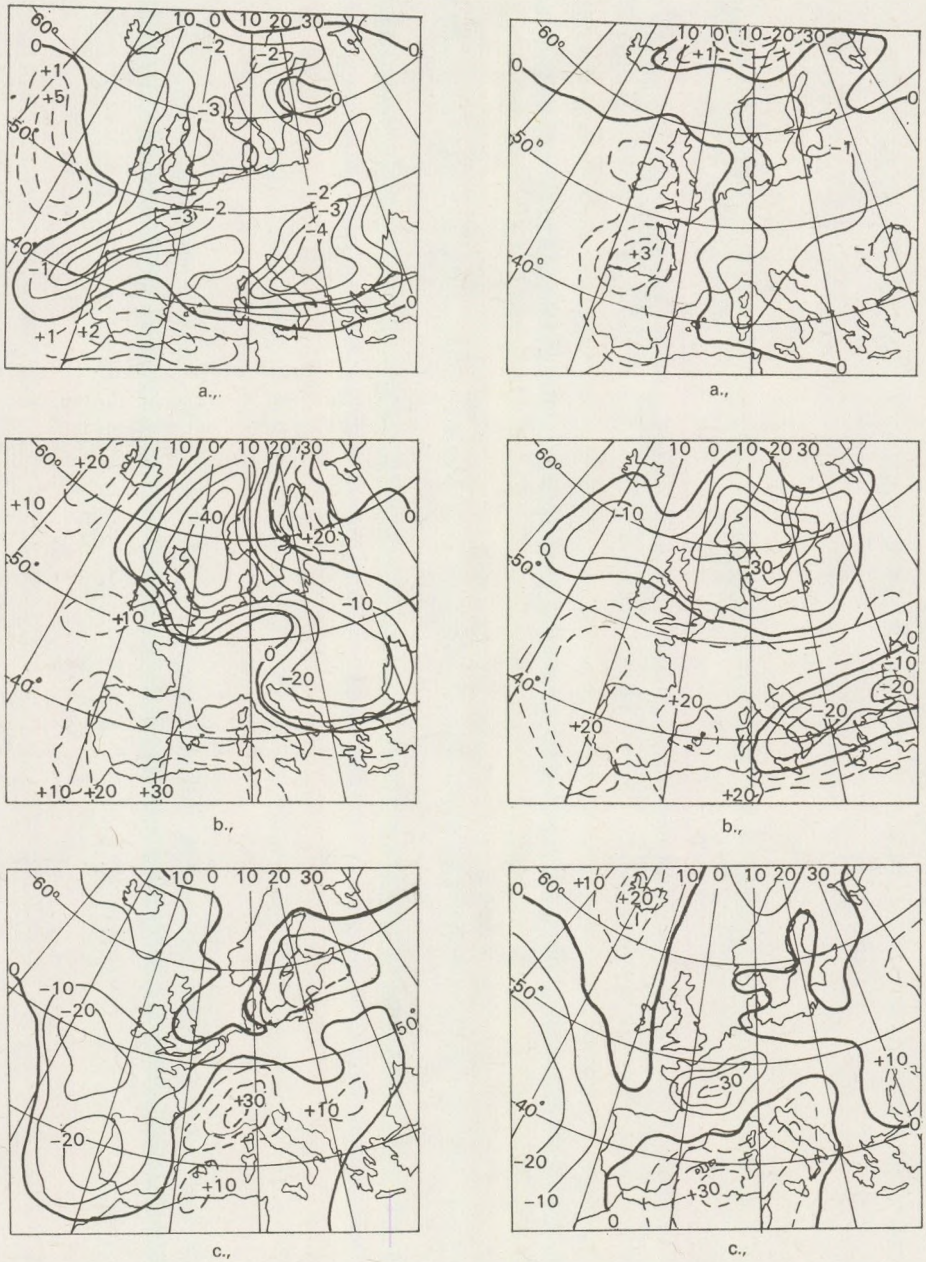

Fig. 4. Areal distribution of the variation of the energies in 10^9 kwatt, from 19th Oct. 12 GMT and 20th Oct. OOGMT; *a)* potential energy, *b)* internal energy, *c)* latent energy

Fig. 5. Areal distribution of the variation of the energies in 10^9 kwatt, from 20th, Oct. OOGMT to 20th Oct. 12 GMT.

developing potential energy. P e t t e r s s e n (1962) made calculations concerning the development of the cyclone of the Atlantic and according to him the contribution of the observable heat of 1 cal cm^{-2} order of magnitude played an accentuated role.

Regarding the development of the Mediterranean cyclone this can be linked first of all with global reasons, it appears in the first phase of its development as a marginal cyclone of a large central one, as a result – according to the maps representing the changes of the individual energies – at first of the contribution of the decrease in potential energy, then setting in motion processes having as a consequence a further development fed first of all on local sources. So, in a later stage the latent energy could be stated as a primary source.

Although the available potential energy might be extremely high at cases, we can not be sure that this transforms partly or completely into kinetic energy. If the flow is purely zonal and the mass, as well as the rotational momentum distribution is in dynamicaly stable equilibrium, then the kinetic energy will not be realized. This appears also immediately, if we consider the figure series 3. We observe extremely high amounts of the available potential energy on the area of the subtropical high pressure belt, while at the same time we encounter in this domain very low values if we follow the distribution of the kinetic energy.

Our foregoing analysis has given answer only to one of the basic problem of the energetics of the atmosphere: how much is the available energy in case of maximum favourable conditions. No answer has been given as yet to the question, which part of this transforms into kinetic energy and this can be given only on the basis of a closer knowledge of the mechanism triggering and determining the process. The answer to this question is made possible only through the use of the whole hydro-thermodynamical equation system, of which we will deal here first of all with the determination of the parameters marking the transformation mechanism as well as with the comparison of the amount of dissipation.

The local change of the kinetic energy can be written in the following form, obtained by a transformation of the horizontal motion equation:

$$\frac{\partial K}{\partial t} = -\frac{1}{g}\int_S \int_{p_2}^{p_1} \left(\nabla kV + \frac{\partial (k\omega)}{\partial p} + V \nabla \varphi - V \nabla F \right) dp\, dS + \\ + \frac{1}{g}\int_S \left(k_1 \frac{\partial p_1}{\partial t} - k_2 \frac{\partial p_2}{\partial t} \right) dS \qquad (6)$$

where $\nabla kV + \frac{\partial (k\omega)}{\partial p}$ is the horizontal and vertical advection of the kinetic energy across the boundaries, $V \nabla \varphi$ is the formation of kinetic energy within the volume due to the effect of horizontal pressing forces, and finally $V \nabla F$ is a simple expression of the frictional loss of kinetic energy.

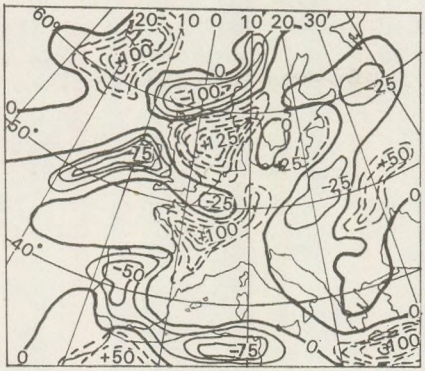

a.,

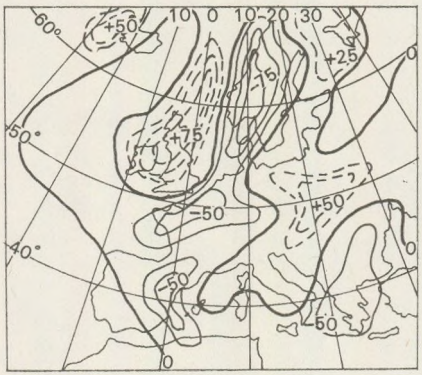

b.,

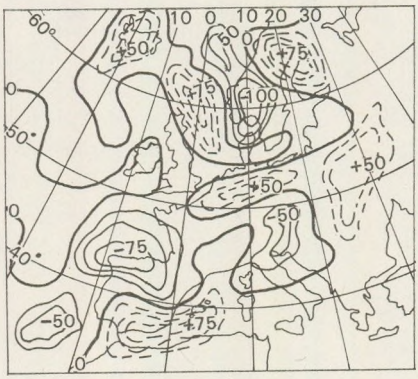

c.,

Fig. 6. Conversion of available potential energy into kinetic one in 10^9 kwatt units,
a) 19 thOct., 1970. 12 GMT
b) 20 th Oct., 1970. OOGMT,
c) 20 th Oct. 1970 12 GMT.

The explicit ness of the expression of $V \nabla \varphi$ is very favourable both of physical sense as well as of the point of view of the analysis of the observed meteorological data. The kinetic energy develops from the potential energy on the expenst of the work exerced by the horizontal pressure force to the air mass, when there is a flow component in the negative direction of the geopotential. If we apply the form of the continuity equation in a p – coordinate-system and the basic equation of the statics, the expression $V \nabla \varphi$ can be written in the following form

$$V \nabla \varphi = \nabla V \varphi + \frac{\partial \omega \varphi}{\partial p} + \alpha \omega \tag{7}$$

Substituting into (6) we get for the local variation of the kinetic energy

$$\frac{\partial K}{\partial t} = -\frac{1}{g} \int_S \int_{p_2}^{p_1} \left[\nabla k V + \frac{\partial \omega k}{\partial p} + \alpha \omega + \nabla V \varphi + \frac{\partial \omega \varphi}{\partial p} - V \nabla F \right] dp dS \tag{8}$$

While the redistribution term $\nabla V \varphi + \frac{\partial \omega \varphi}{\partial p}$ presents itself as the indicator of the effective development of the kinetic energy, the term $\alpha \omega$ can be taken as the indicator of the release of the available potential energy. If the term $\alpha \omega$ is written in the form of the areal average and of the deviation of it we get

$$\alpha \omega = \overline{\alpha \omega} + \alpha' \omega' \tag{9}$$

and in this alternative the conversion is in connection with the space correlation of α' and ω'. On the parts, where the air warmer than its sourroundings rises and the cooler air descends, the positive circulation supports the conversion into kinetic energy, while on areas, where the negative (indirect) circulation takes place – this being connected with a destruction of kinetic energy –, the increase of the available potential energy sets in. This is apparent immediately also form the equation describing the local change of the available potential energy, which can be written – after calculations not given here is detail – and differentiating equation 5. – in the following form:

$$\frac{\partial A}{\partial t} = \frac{1}{g} \int_S \int_{p_2}^{p_1} \left[(\dot{Q} + \delta) \left(1 - \frac{p_r^\varkappa}{p^\varkappa} \right) + \alpha \omega - \nabla \left(1 - \frac{p_r^\varkappa}{p^\varkappa} \right) V c_p T - \right.$$

$$\left. - \frac{\partial \left(1 - \frac{p_r^\varkappa}{p^\varkappa} \right) \omega}{\partial p} \right] dp \, dS +$$

$$+ \int_S \left[c_p \left(\frac{p_1^\varkappa - p_{r1}^\varkappa}{p_1^\varkappa} \right) T_1 \frac{\partial p_1}{\partial t} - \left(\frac{p_2^\varkappa - p_{2r}^\varkappa}{p_2^\varkappa} \right) T_2 \frac{\partial p_2}{\partial t} \right] dS \tag{10}$$

where Q is the heat added to or taken out of the unit mass, the individual forms of which can be: evaporation, condensation, various components of radiation, the sensible heat- contribution etc., σ is the friction heating, this being always positive; the term

$$\nabla\left(1-\frac{p_r^{\varkappa}}{p^{\varkappa}}\right) V c_p T + \frac{\partial\omega\left(1-\frac{p_r^{\varkappa}}{p^{\varkappa}}\right)}{\partial p}$$

is the horizontal and vertical advection of the potential and internal energy across the boundaries, while the last term reflects the change of the vertical boundaries; we find also the term $\alpha\ \omega$ marking the transformation with opposite sign, representing here the transformation of the available potential energy into kinetic one.

Since the determination of the $\alpha\omega$ conversion term depends according to (9) strongly on that how can we estimate ω from the operationally smoothed and modified data (obtained by means of adiabatic, quasigeostrophic or kinematic methods) the reliability of the conversion term can be uncertain on areas, where the boundary conditions set by one or another method are not fulfilled

In the course of our investigation we have determined ω in the expression $\alpha\ \omega$ concerning the development of kinetic energy by a kinematic method for the layer between the ground and 100 mb, supposing that this layer incorporates the most part of the influence of processes of synoptic scale, but the value of ω has been certainly underestimated at the places, where the release of latent heat is significant. Also here – as we did earlier – we do not present the whole material owing its largeness, but we show the term $\alpha\ \omega$ only in the dates of the three ascents indicated, (Figs 6. a., b and c.).

The highest values of conversion are found to the left – when looking. with the direction of the flow – from the centres representing the highest values of the kinetic energy. The maximum values of the kinetic energy appear on these areas after the next 12 hours, while in the spots of the previous centers the highest reduction of the kinetic energy, i.e. a negative conversion can be found, and at the same time the available potential energy is significantly increased. When looking back again to the formation period of the Mediterranean cyclone and to the maps showing the variation of potential as well internal energies we find a decreasing march. In reality we have here the strongest withdrawal of air and the highest vertical divergence of the velocity is also formed here in connection with the ascending movement within the cyclone. As a matter of fact, part of the released energy is used up for the expansion work and for the kinetic energy of the vertical movements. In the whole domain, the transformation value computed from data of the six ascents was oscillating – according to the data of Table I. – between $+139\cdot10^8$, $+589\cdot10^8$ $+106\cdot10^8$, $+582\cdot10^8$, $-233\cdot10^8$, $+102\cdot10^8$ kwatt, and this values were strongly influenced by the terms representing the horizontal and vertical advection. While the vertical transport is

only of a modificating influence, the horizontal energy transport may be especially singificant at the jet level. This indicates that the local production of the kinetic energy dies not necessarily feed on sources available on the spot.

Regarding the significance of the energy transport across the boundaries we can read in a theoretical study of Van Mieghem (1967). The application of his ideas from the point of view of cyclogenesis has been studied theoretically by Eliassen (1952), while from the diagnostic aspect it was Sechrist who has treated them (1968). The boundary-processes in the variation of the available potential and kinetic energy of an open system play so much an important part, the smaller the domain is, for the conditions of which the processes are treated. To demonstrate this we can apply – among others – also in the case of the Mediterranen cyclone the circomstance that, if we restrict ourselves to the domain marked by Radinovic (1968) in the formation phase of a Mediterranean cyclone, i.e. we write the summed up transformation term for the area between the 0° and East 17.5° meridians, respectively between the latitudes 30° N and 47.5° N, we get the values: $-1{,}06 \cdot 10^{10}$ kwatt at 12^h on the 19 th, $-0.8 \cdot 10^{10}$ kwatt at 00^h and $+3.6 \cdot 10^{10}$ kwatt at 12^h, i.e. in the formation stage of the cyclone the summed up values does not seem to support the transformation into kinetic energy. More detailed investigation has shown that the positive values of the transformation into kinetic energy on these days could be found only in the lower third of the troposphere, while in the upper parts we get negative values and this surpassed the lower positive conversion value in the course of summation. Because in the regional domain there was present a very significant amount of released latent heat, by all certainly the computation of the vertical velocity by a kinematical method has led to an underestimation of the real vertical movements, to which the energy transport across the boundary was added as a significant component. In the last column of Table I. we see the dissipation values of a lower, about 1000 m thick layers of the troposphere. According to the data of the six escents the dissipation oscillated between $257 \cdot 10^8$ and $448 \cdot 10^8$ kwatt. If we compare this value with the average kinetic energy (column 18., Table I.) of the lower layer we find that in case the rate of dissipation does not change and if we have no assurance for the replacement of the kinetic energy, this would be taken out of the layer of the troposphere indicated above during an average time of 7.8 hours. To similar result came also Boriszenkov, according to the computation of whom the kinetic energy of the lower layer would be dissipated in less than one day, while the total troposphere would give away its complete kinetic energy in 3–4 days. Kung (1966) has carried out computations concerning the connection between the kinetic energy of the lower layer and its dissipation. His results show that in case of a rate of the dissipation as high as 2.21 wattm^{-2} the kinetic energy would be dissipated from the lower layer in an average time of 4.3 hours.

According to Kung (1966) about 31% of the complete dissipation takes place in the lower layer of 1 km thickness. If we take into account this

ratio, and using the dissipation value obtained we can get the exhaustion time for the entire domain, which can be estimated – according to Kung – to 2.73 days. The average depletation time computed from the data of the single days amounted to 4 days in our case.

The results discucced above attire the attention – among others – of the scientists to the circumstance that models applied to the forecasting of weather can promise reliable results only in case they will be completed by a suitable model of the energy transformation.

REFERENCES

Ворисенков Е. Н. 1960: Вопросы энергетики атмосферных процессов. Гидрометеоиздат Ленинград.

Danard, M. B., 1964: On the influence of released latent heat on cyclone development. Journal of Applied Meteorology. 3 pp. 27 – 37.

Dutton. A., Johnson, D. R., 1969: The theory of available potential energy and a variational approach to atmospheric energetics. Advances in Geophysics 12 pp. 333 – 436.

Eliassen, A., 1960: On the initial development of frontal waves. Publ. Danski Meteor. Institut Meddelser No. 13.

Holopainen, E. O., 1963: On the dissipation of the kinetic energy in the atmosphere. Tellus 15. 3. pp. 26 – 32.

Kung, E. C., 1966: Large scale balance of kinetic energy in the atmosphere. Monthly Weather Review. 94. No. 11. pp. 627 – 640.

Lorenz, E. N., 1955: Available potential energy and the maintenance of the general circulation. Tellus 7. No. 4. 157 – 167.

Makainé Császár Margit 1973: The role of efficiency factor and nonadiabatic agents for the development of the mediterranean cyclone. Annales Sectio Geologica XVII. Budapest 315 – 322.

Oort, A. H. 1964: On estimates of the atmospheric cycle. Monthly Weather Review 92. pp. 483 – 493.

Petterssen, D. L., Bradbury, X., Pedersen, K., 1962: The Norvegian cyclone models in relations to heat and cold sources, Geophysiske Publikasjoner Geophysica Norvegica V. XXIV. pp. 243 – 286.

Radinovic, Dj., Mesinger, F., 1968: Dinamicke i energetske karakteristike razvoja ciklona od 24 oktobre u zapadnom sredozemlju. Prirodne – Matematicki Faktultet w Beogradu – Meteoroloski Zavod, Beograd.

Sechrist, F. S., 1968: Energy conversion in a developing cyclone. Ph. D. Thesis, Dept. of Meteorology, Pensylvania State Unio.

Smagorinsky, J., 1968: On the inclusion of moist adiabatic processes in numerical prediction models. Berichte des deutschen Wetterd. 5. No. 38. 82 – 90.

Smith, Ph. J., 1969: On the contribution of limited region to the global budget. Tellus 21. No. 2. pp. 202 – 207.

Smith, Ph., J.,1973: Midlatitude synoptic scale systems: their kinetic energy budgets and role in the general circulation. Monthly Weather Review. 10 pp. 757 – 761.

Van Mieghem, J., 1960: Energy transport across internal boundaries. Beiträge zur Physik der Atmosphäre. 40. pp. 1 – 6.

EULERIAN ANGLES AND THE PSEUDOSYMMETRY OF THE PLAGIOCLASE

L. ÖRKÉNYI-BONDOR

(Department of Mineralogy and Petrography, Museum of Sciences, Budapest)

Received: 22. December 1976

SUMMARY

Theoretical evidence for the solution of a practical problem has been given in the paper. Basing on measurements made by means of a Fedorov table new plagioclase twin laws were described in 1974, but the authors did not deal with the elimination of error caused by pseudosymmetry. Normal twin laws according to (110) and $(1\bar{1}0)$ as well as according to (130) and $(1\bar{3}0)$ could not be separated when basing only on external symmetry, since the angle deviation falls between the limits of measuring errors. But the relative position of crystallographic symmetry and of the optical indicatrix unequivocally determines whether in a given case we have to deal with a right or left form. For a correct determination of the plane index we have to state the relative position of the rectangular coordinate axes of irrational index taken of the basis of triclinic cristallographic directions.

When two new plagioclase twins were described *(L. Bondor—H. Szeberényi*, 1974) on the basis of data obtained from optical measurements by universal-stage, in all cases the Eulerian angles helped us to distinguish the right forms from the left ones. There was no problem to determine in the way of drawing on a stereographic net that the twin plane is the (110) or $(1\bar{1}0)$ face and in the other case it is the (130) or $(1\bar{3}0)$ face. It did not seem to be necessary to give the theoretical evidence of the applied method.

Because several mineralogists have doubted the possibility of the separation of the right and left forms, it seems to be necessary to return to this question.

The limit of error of the optical measurements is generally greater than it is in the case of measurements by goniometer. This fact may lead to an erroreous determination of the indices indeed in case of pseudosymmetry. But if the optical orientation is compared with the crystallographic one, the correct indices can be determined.

In the case of plagioclase crystals the triclinic crystallographic system of co-ordinates compared with the indicatrix would be a difficult thing. If we choose a Cartesian but irrational set after C. Burri *(C. Burri—R. L. Parker—E. Wenk*, 1967) it will be possible to use Eulerian angles, because the Eulerian angles relate to Cartesian set with the same origo.

The axes of the chosen crystallographic system of co-ordinates are indicated as XYZ

$$X = \frac{\perp [001]}{(010)} \qquad Y = \perp (010) \qquad Z = [001]$$

The optical axes are indicated as ABC

A = the highest optical elasticity direction, or optical main vibration direction

B = the medium optical elasticity direction

C = the lowest optical elasticity direction

In an other paper will be described the calculation of the indices on the basis of the optical and crystallographical data obtained from measurements by universal-stage.

Here we are dealing with the problem how the correct signs of the vector components and of the indices in the case of pseudosymmetry may be defined.

The first figure shows a plagioclase intergrowth which consists of six twin members, but the sixth is not measurable. In the first complex the intergrowth plane is the (010) face. Between the first and second individuals an Albite twin law is valid. The data are as follows:

Individual 1.	$n_a = 262.5°$	$h_a = 37°$
	$n_b = 18.5°$	$h_b = 30°$
	$n_c = 136°$	$h_c = 39°$
Individual 2.	$n_a = 190.5°$	$h_a = 36.5°$
	$n_b = 75°$	$h_b = 30°$
	$n_c = 317.5°$	$h_c = 39°$
Individual 3.	$n_a = 224.5°$	$h_a = 29°$
	$n_b = 318.5°$	$h_b = 8°$
	$n_c = 62{,}5°$	$h_c = 60°$
Individual 4.	$n_a = 267°$	$h_a = 38.5°$
	$n_b = 9.5°$	$h_b = 15°$
	$n_c = 122°$	$h_c = 48°$
Individual 5.	$n_a = 36°$	$h_a = 80.5°$
	$n_b = 144.5°$	$h_b = 2.5°$
	$n_c = 235°$	$h_c = 10°$

The data of the measurement of the intergrowth planes:

	$n_I = 317°$	$h_I = 0°$
	$n_{II} = 79.5°$	$h_{II} = 22°$
The lines of growth:	$n_g = 317°$	$h_g = 1°$
Cleavage:	$n_{cl} = 80.5°$	$h_{cl} = 21°$

The figure 2. shows the data of the measurements.

In the second complex there are three measurable twin members. Between the third and fourth individuals there is an Albite-Carlsbad complex twin law, the twin axis is equal to the X axis in the system of

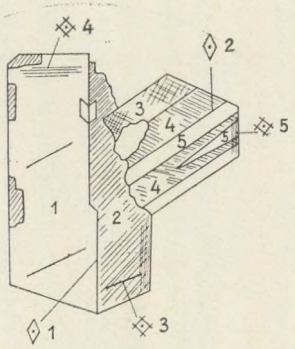

Fig. 1.

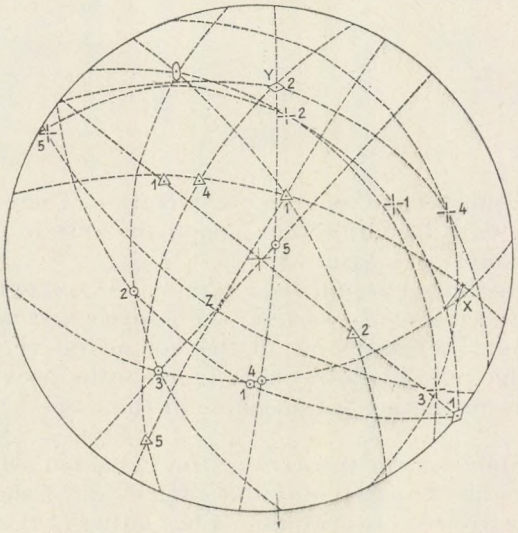

Fig. 2.

co-ordinates. Between the third and fifth members there is a Carlsbad twin law, and the twin axis is equal to the Z coordinate axis. The fourth and the fifth are Albite twins, the normal of the (010) plane is the Y axis.

If we choose such a stereographic projection plane which is the same as on the table 2. *(C. Burri – R. L. Parker – E. Wenk,* 1967) the Z axis will be in the centre, and the X and Y axes will be on the outline of the circle. (Figure 3.)

Between the second individual and the third one there is a twin law and we want to define the twin axis. The second stereogram may be fitted on the table 2. in four different way (Figures 4a, 4b, 4c and 4d). So the requested twin axis may be near the (130) face and the $(1\bar{3}0)$ also. This uncertainty is caused by the fact that the positive and negative directions

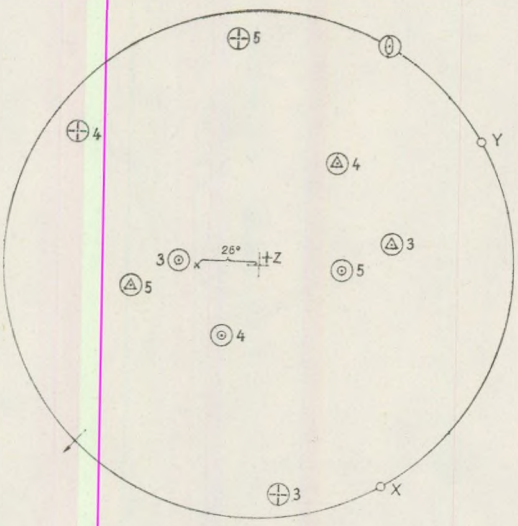

Fig. 3.

of the axes have not been taken into consideration. There are not sufficient crystallographic data to define the signs of the axes in many cases of investigation by universal-stage.

If this Cartesian set would be a rational crystallographic set (in the orthorhombic, and tetragonal system) the positive and negative directions of the axes would be invertable in the holohedral classes, because the symmetry of the right-angles system of co-ordinates requires all those points which are in the projection plane in the case of the four different fittings.

In the triclinic system the axes of the Cartesian set are not rational crystallographic directions, so only one fitting out of the four is possible. The inversion centre requires two points but either of them is on the lower half of the sphere.

The Eulerian angles proposed by C. Burri help us to choose the correct fitting.

The anortite content of the individuals may be read off on the plate IX. (*C. Burri — R. L. Parker — E. Wenk*, 1967). The anortite content varies between 75 — 78%. We can see the I., II., and III. kinds of Eulerain angles in catalogue 41. of the above authors. That fitting will be correct, in which the correct Eulerian angles can be read off. When the third individual shows the corresponding Eulerian angles the twin axis coincides with the ($\bar{1}30$) face (Figure 4a). The second individual shows the twin axis to coincide with the ($1\bar{3}0$) face at the corresponding Eulerian angles.

The result of the drawing there is a twin law according to ($1\bar{3}0$).

That has been an example how the problem should be solved by drawing. Now the theoretical evidence of the solution must be given.

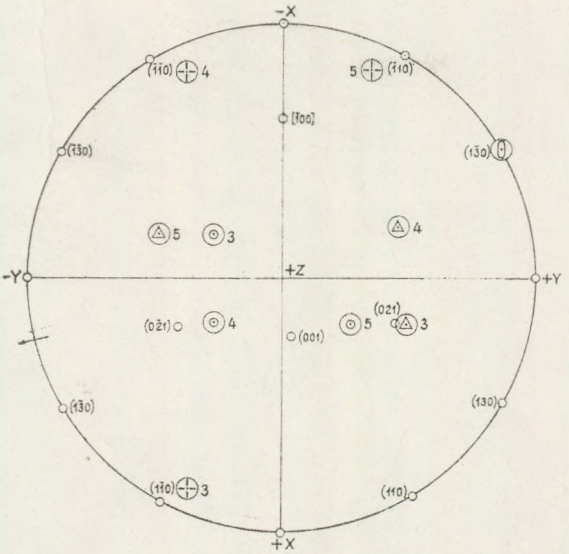
-X
(1̄10) 4
5 (110)
[100]
(1̄30)
(130)
5
3
4
+Z
-Y
+Y
(021)
(0ž1)
4
(001)
5
3
(1̄30)
(130)
(1̄10) 3
(110)
+X

Fig. 4a.

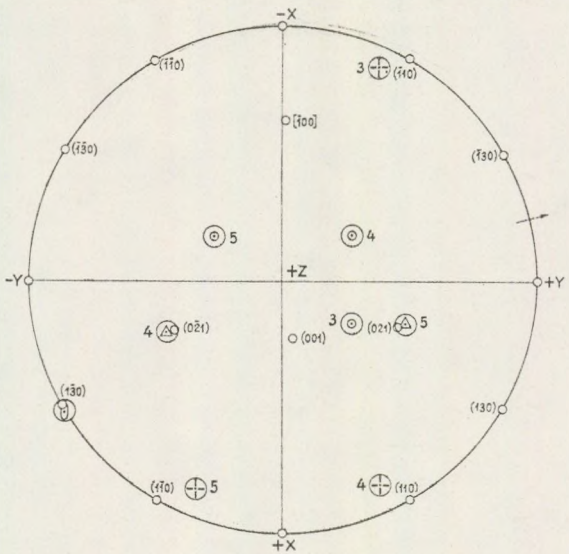
-X
(1̄10)
3 (110)
[100]
(1̄30)
(130)
5
4
+Z
-Y
+Y
4 (0ž1)
3 (021) 5
(001)
(130)
(1̄30)
(1̄10) 5
4 (110)
+X

Fig. 4b.

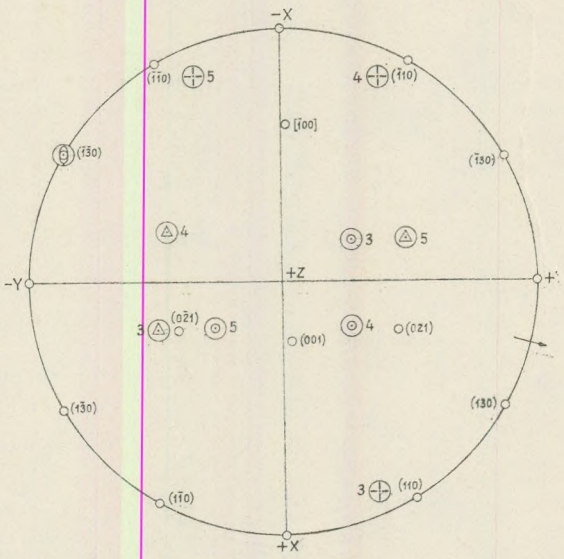
-X
(1$\bar{1}$0) 5
4 (110)
[100]
(1$\bar{3}$0)
(130)
4
3 5
-Y
+Z
+Y
3 (0$\bar{2}$1) 5
(001)
4 (021)
(13$\bar{0}$)
(130)
(11$\bar{0}$)
3 (110)
+X

Fig. 4c.

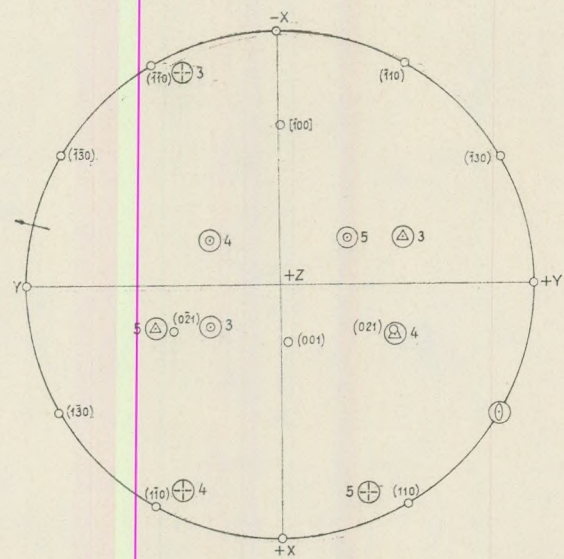
-X
(1$\bar{1}$0) 3
(110)
[100]
(1$\bar{3}$0)
(130)
4
5 3
Y
+Z
+Y
5 (0$\bar{2}$1) 3
(001)
(021) 4
(13$\bar{0}$)
(1$\bar{1}$0) 4
5 (110)
+X

Fig. 4d.

What is unknown during the calculation or the drawing are those axial directions of the XYZ system of co-ordinates having a positive sign. If one of the three axes is taken with the opposite sign the set will be one of left-handed rotation. This mistake would not be committed if the rotation of the axes would be taken into consideration. All the axes can be inverted withouth an error, the result are the same, because the plagioclase crystals have an inversion centre.

Only one case should be examined i.e. when the sign of two axes are changed.

Point P is the position of the pole of a particular face. The coordinates of point P in the XYZ system of co-ordinates are indicated as $P(x, y, z)$. The vector of the normal of the face is:

$$p = xi + yj + zk$$

The same point P in the ABC set is indicated as P(a. b, c), the normal of the face:

$$p = am + bn + co \quad \text{if} \quad m, n \quad \text{and} \quad o$$

are the unit vectors in the directions of the corresponding axes.

Transformating the XYZ system of co-ordinates into the ABC system, the components of the point P are as follows:

$$a = x \cos (\widehat{AX}) + y \cos (\widehat{AY}) + z \cos (\widehat{AZ})$$

$$b = x \cos (\widehat{BX}) + y \cos (\widehat{BY}) + z \cos (\widehat{BZ})$$

$$c = x \cos (\widehat{CX}) + y \cos (\widehat{CY}) + z \cos (\widehat{CZ})$$

$$p = [x \cos (\widehat{AX}) + y \cos (\widehat{AY}) + z \cos (\widehat{AZ})]m + [x \cos (\widehat{BX}) + y \cos (\widehat{BY}) +$$

$$+ z \cos (\widehat{BZ})]n + [x \cos (\widehat{CX}) + y \cos (\widehat{CY}) + z \cos (\widehat{CZ})]o$$

If we take the opposite direction of the X and Y axes as positive directions and the indication of these are as X' and Y', and we take a point P' which has the same coordinates as the point P, then P'(x', y', z'). The value of x', y' and z' in the X'Y'Z system of co-ordinates are the same as those of x, y and z are in the XYZ set. Transformating the X'Y'Z system of co-ordinates into the ABC set, the components are as follows:

$$a' = x \cos (\widehat{AX'}) + y \cos (\widehat{AY'}) + z \cos (\widehat{AZ})$$

$$b' = x \cos (\widehat{BX'}) + y \cos (\widehat{BY'}) + z \cos (\widehat{BZ})$$

$$c' = x \cos (\widehat{CX'}) + y \cos (\widehat{CY'}) + z \cos (\widehat{CZ})$$

If the three members of the sum are different from one another and from zero, the value of the sum cannot remain the same if two of the members are taken with opposite sign. If are there any cases when $a = a'$,

$b = b'$, $c = c'$ or $a = -a'$, $b = -b'$, $c = -c'$ errors are possible, and we cannot eliminate the uncertainty of the indices. The first three equalities cannot be realized if x and y differ from zero.

The above second three equalities may exist in some special cases. Two members of the sums are zero, if all the three axes of the ABC system of co-ordinates coincide with the axes of the XZY set. The variations are as follows:

If	$A = X$	$B = Y$	$C = Z$
then	$a = x$	$b = y$	$c = z$
	$a' = -x$	$b' = -y$	$c' = -z$
if	$A = Y$	$B = Z$	$C = X$
then	$a = y$	$b = z$	$c = x$
	$a' = -y$	$b' = -z$	$c' = -x$
if	$A = Z$	$B = X$	$C = Y$
	$a = z$	$b = x$	$c = y$
	$a' = -z$	$b' = -x$	$c' = -y$

In the other three cases we take the negative directions of the axes of either of the two system of co-ordinates. The absolute values of the components are different independence on the axes of the ABC set coincide with which axis of the XYZ system. Consequently $a = -a'$, $b = -b'$, $c = -c'$. Because the absolute values of the co-ordinates are the same as all the three have an opposite sign, it is impossible to define the correct indices.

In another special case one axis of the XYZ system of co-ordinates coincide with one axis of the ABC set. The other four axes must be in one plane.

If we choose the opposite sign of those two axes of the XYZ set which lie in the common axial plane, then one member of two sums will be zero. Taking the other two members with an opposite sign will give the same absolute value. The third component has two members equalling zero.

Let us see that case, when $C = Z$. The XYZ system of co-ordinates transformating into the ABC system:

$$a = x \cos (\widehat{AX}) + y \cos (\widehat{AY})$$

$$b = x \cos (\widehat{BX}) + y \cos (\widehat{BY})$$

$$c = z$$

$$a' = -[x \cos (\widehat{AX})] - [y \cos (\widehat{AY})]$$

$$b' = -[x \cos (\widehat{BX})] - [y \cos (\widehat{BY})]$$

$$c' = -z$$

So $a = -a'$, $b = -b'$, $c = -c'$ equalities exist in this case also.

Any other symmetrical position is geometrically impossible between the two systems of co-ordinates.

Practically we cannot define the correct indices in two special cases: 1. The axes of the two systems of co-ordinates are near each other. 2. One axis of the ABC set is near one axis of the XYZ system of co-ordinates, and the other axes are near in one plane.

We may say it in an other sense that the transformation of a Cartesian set into another right-angles system of co-ordinates (with the same origo) is unambiguous excepting the above mentioned two special cases.

Working with Eulerian angles on the plane of the stereographic projection the solution of that problem is more simple. Taking the first kind Eulerian angles the drawing is as follows:

The axes of the first system of co-ordinates are n_α, n_β, and n_γ optical vibration directions which must be transformed into the XYZ set. First we make a right-handed rotation around Z as an axis of rotation, so the line of intersection between the XY and the n_β n_γ planes must fall into the X direction. The rotation angle is $-\Phi$, if the n_β direction is in the negativ part of the Y axis after rotation. Making a right-handed rotation around the $+$X axis n_α falls into the $+$Z direction. The rotation angle is Θ. Finally we make a right-handed rotation around Z, so n_β falls into $+$X and n_γ falls into $+$Y. The rotation angle is Ψ.

The other two kinds of Eulerian angles are obtained by left-handed rotation.

The second kind Eulerian angles: Making a left-handed rotation around axis Z, the line of intersection between the XY and the n_α n_γ planes falls into the X axis. The rotation angle is R, so n_β falls in the positive part of the Y axis. We make a left-handed rotation around $+$X, the n_β falls into $+$Z, the rotation angle is I. Then we make a left-handed rotation around $+$Z, the n_γ falls into the $+$X, the rotation angle is L.

The third kind Eulerian angles are as follows: First we make a left-handed rotation around axis Z as an axis of rotation, so the line of intersection between the XY and n_α n_β planes must fall into the X axis. The rotation angle is D, n is in the $+$Y axis. Then making a left-handed rotation around $+$X, so the n_γ falls into the $+$Z axis. The rotation angle is N. Finally we make a left-handed rotation around $+$Z so the n_α must fall into the $+$X axis. The rotation angle is K.

If the opposite directions of two axes of the XYZ set will be taken as positive axes, and the rotation will be made as above, the result is as follows:

. $-\Phi' = 180° - \Phi$	$\Theta' = \Theta$	$\Psi' = \Psi$
. R′ = 180°+R	I′ = I	L′ = L
. D′ = 180°+D	N′ = N	K′ = K

One of the three Eulerian angles is certainly not the same as it is in the first case.

If the $-\Phi$ angle is near 90° and the Ψ is also near 90°, the n_γ vibration direction falls near the negative direction of the Y axis. At the law-temperature plagioclase crystals in the case of 20% anorthite content the $-$Y axis and the n_γ vibration direction form an angle of 1.3°. Here a very

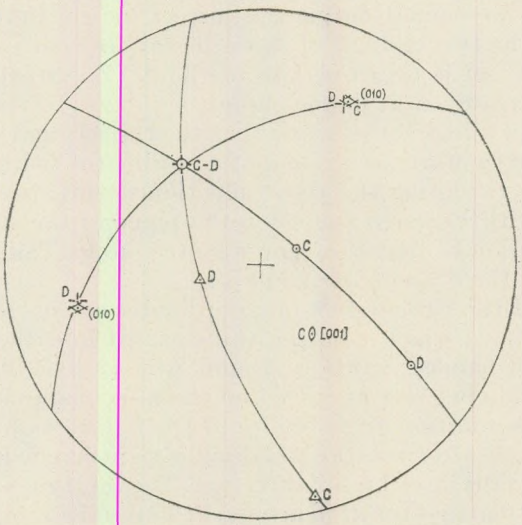

Fig. 5.

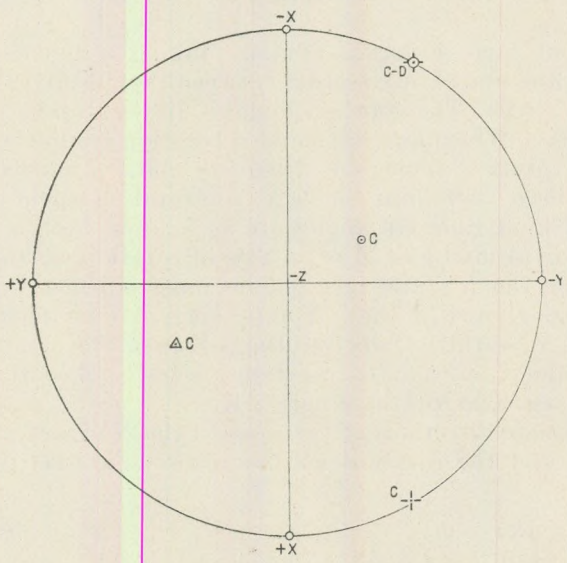

Fig. 6.

precise microscope and universal-stage is needed to eliminate the error. In the case of the other members of plagioclase series there is no problem like this.

The way in which the optical vibration directions relate to the crystallographic orientation is a characteristic feature of the minerals. In plagioclase crystals it is a lucky circumstances that the indicatrix and the crystal-

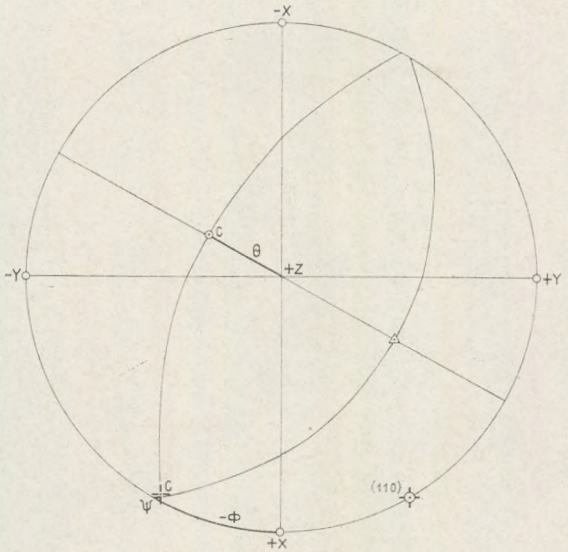

Fig. 7.

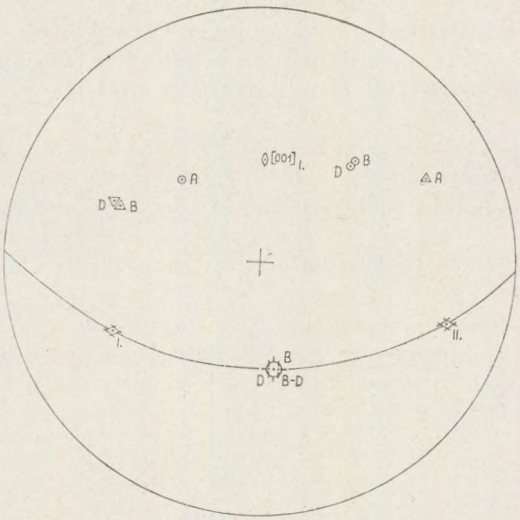

Fig. 8.

lographic orientation are in a general position and therefore the position of the ABC system of co-ordinates and of the XYZ set is also a general one.

The figures 5 – 9 show how the sign of the axes can be defined. The figure 5 shows the measured data of the C and D members of a plagioclase twin crystals.

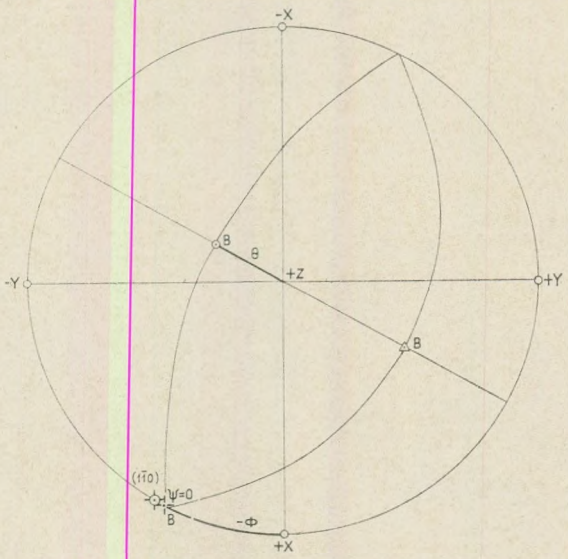

Fig. 9.

On the figure 6 the rotated member C can be seen, the projection plane being the XY plane. If this is rotated with 180° around the X axis, the figure 7 will show the Eulerian angles and the correct sign of the angles.

Figure 8 shows the measured data of the A, B and D members of an other plagioclase intergrowth. In the figure 9 the individual B is rotated into the XY plane. The Eulerian angles can be seen withouth further rotation.

Eulerian angles may also be used at monoclinic minerals in a similar way.

Eulerian angles and right-angle cristallographic co-ordinate systems in the literature are proposed only for plagioclase crystals. A Cartesian set can be established for any mineral whatever, provided that the most frequent faces and zone axes are taken into consideration.

LITERATURE

Burri, C. (1974): Vereinfachte Berechnung der Euler-Winkel Charakterisierung der Plagioklasoptik. SMPM 54, 33 – 38.

Burri, C., R. L. Parler, E. Wenk (1967): Die optische Orientierung der Plagioklase. Basel, Birkhäuser.

Burri, C., Örkényi-Bondor, L., Vincze-Szeberényi, H. (1976): Rechnerische Auswertung von U-Tischoperationen durch elementare Vektormethoden. SMPM 56, 1 – 38.

Örkényi-Bondor, L., Vincze-Szeberényi, H. (1974): (1$\bar{1}$0), (110), (130) and (1$\bar{3}$0) plagioclase twinning in andesite from Hungary. Acta Geol. Acad. Scientiarum Hungaricae, 18, 99 – 138.

ВАРИАНТ АППАРАТУРЫ ДЛЯ РАДИОВОЛНОВОГО ПРОСВЕЧИВАНИЯ

В. ИВАНОВА, С. ПИЩАЛОВ

SUMMARY

The paper deals with instrumenttechnical and methodological problems of geophysical prospecting of ore deposits based on radiowave – transillumination. Instruments and methods elaborated have been successfully applied to industrial practice.

Кафедра геофизических методов разведки Софийского горногеологического института проводит работы по выяснении возможности метода радиоволного просвечивания на полиметаллических месторождениях в Н. Р. Болгарии.

Для проведения этих исследований разработан комплект аппаратуры для шахтнового варианта метода комплектованный с миниаторным скважинным передатчиком. При создании аппаратуры учитывая характеристики и особенностей существующих вариантов ставились следующие требования:

а) относительно простое схемное решение с необходимой стабильностью и точностью работы и сравнительная простота обслуживания в процессе наблюдений;

б) небольшие габариты и вес при достаточно большой мощности передатчика и высокой чувствительности приемника, обеспечивающие оптимальные интервалы просвечивания.

В разработанный комплект аппаратуры для шахтного варианта радиоволнового просвечивания входят: передатчик, приемник и комплект генераторных и приемных антен.

Блок-схема передатчика показана на рис. 1. Задающий генератор с кварцевой стабилизацией работает на четырех фиксированных частотах – 0,46; 1; 3,5 и 8 мгц. Буферный каскад ослабляет влияние усилителя мощности на задающий генератор и таким путем повышается стабильность частоты генератора.

От усилителя мощности сигнал высокой частоты подается в антенну, в качестве которой могут быть использованы штырь или рамка.

Передатчик выполнен на пальчиковых радиолампах по принципальной схеме, показанной на рис. 2. Задающий генератор выполнен на лампе 6 НЗП (левый триод) по емкостной трехточечной схеме. Частота

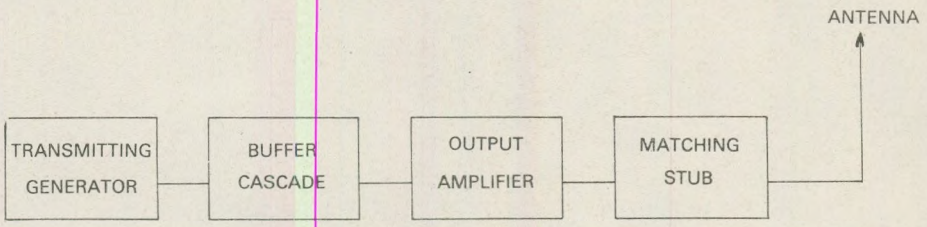

Рисунок 1. Блок схема передатчика

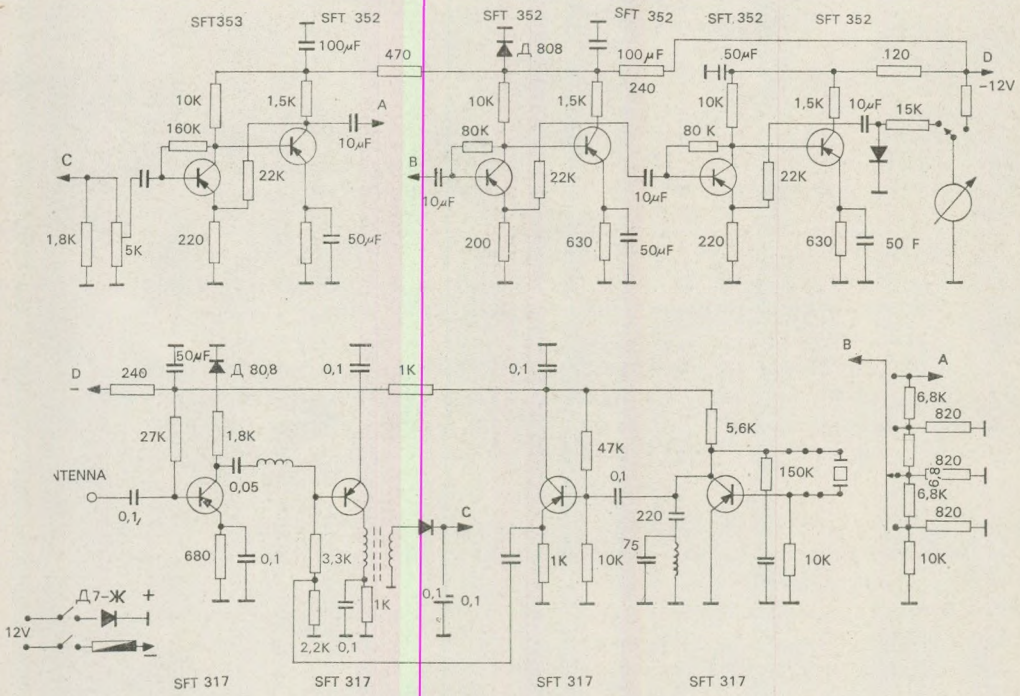

Рисунок 2. Принципиальная схема передатчика

генератора стабилизирована кварцевым резонатором, включенным между сеткой и анодом лампы. Необходимо отметить, что стабилизация частоты кварцем является самым эффективным методом частотной стабилизации в области высоких частот и относительная нестабилность по частоте при термостатировании кварца достигает 10^{-7}. С целью сохранения постоянного выходного напряжения задающего генератора при работе на различных частотах анодное напряжение лампы меняется ступенчато (сопротивления 68 к и 120 к).

Буферный каскад выполнен на лампе 6Н3П (правый триод) по схеме катодного повторителя. Катодный повторитель имеет большое входное и малое выходное сопротивления. Напряжение анодного питания

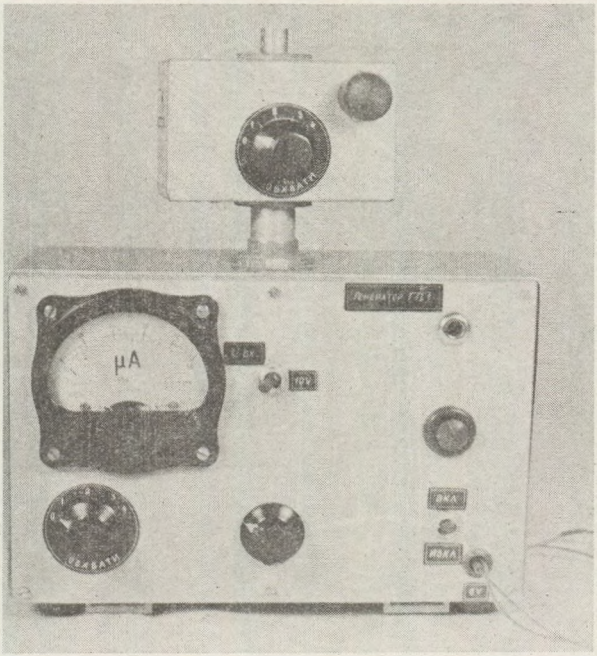

Рисунок 3. Общий вид передатчика

задающего генератора и катодного повторителя подается через развязывающий RC—фильтр (800 ом и 500 пф). Высокочастотное напряжение, которое подается с выхода катодного повторителя на вход усилителя мощности, может плавно регулироваться (потенциометр 5 к.).

Усилитель мощности (оконечный каскад) выполнен на пентоде 6П15П по параллельной схеме питания. Ввиду этого антенна не находится под постоянным напряжением, что отвечает требованиям техники безопасности при работе в штольнях с повышенной влажностью.

Антенна передатчика, штыревая или рамочная, включается в анодную цепь усилителя мощности посредством согласующего устройства. Для контроля выходной мощности часть высокочастотного напряжения на выходе измеряется с помощью амплитудного вольтметра. Через потенциометр 5к задается перенапряженный режим в оконечном каскаде и выходное напряжение не требует наличия абсолютной настройки антенны. Это в значительной мере облегчает работу с генератором. Для получения напряжения анодного питания используется транзисторный преобразователь напряжения.

Постоянное напряжение с аккумулятора (6 V) с помощью двухтактного блокинг-генератора преобразуется в напряжение прямоугольной формы, которое выпрямляется мостовой выпрямительной схемой. Трансформатор преобразователя имеет ферритовый сердечник, что способствует повышению коэффициента полезного действия. Для предох-

ранения обоих транзисторов SFT –213 от обратного (неправильного) включения питающего напряжения в схеме включен защитный диод SFR –136.

Для накала всех ламп генератора используется постоянное напряжение 6 V от аккумулятора.

Внешний вид передатчика показан на рис. 3. Конструктивно он выполнен в виде параллелепипеда, размерами 230×155×130 мм, имеет вес 1,9 кг. и следующие технические данные:

рабочие частоты – 0,456; 1; 3,5 и 8 мгц;
выходная мощность – 1 вт
потребляемая мощность – 15 вт
(питание генератора осуществляется от двух аккумуляторов сц–10).

Основной частью аппаратуры является приемник. В известной аппаратуре для радиоволнового просвечивания приемник обычно выполняют по супергетеродинной схеме с большим резонансным каскадом, обеспечивающих высокую селективность приема. Такие приемники имеют значительные габариты и в процессе работы недостаточно стабильны.

В разработанном приемнике использованы некоторые новые схемные решения, которые отличают его от известных.

Блок-схема приемника показана на рис. 4. Приемная антенна рамочая и путем настройки согласовывается с входным сопротивлением высокочастотного усилителя.

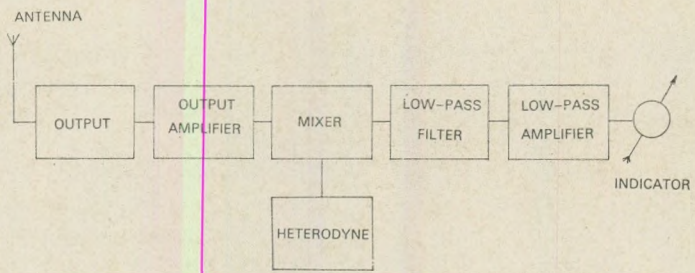

Рисунок 4. Блок схема приемника

Частота гетеродина подобрана так, чтобы промежуточная частота попадала в звуковой диапазон (она порядка 50–100 гц). Смеситель диодный. Ввиду низкой промежуточной частоты используется обычный низкочастотный усилитель с суженной полосой пропускания. Применением низкочастотного усилителя вместо резонансного достигнуто значительное увеличение стабильности работы приемника.

Это важное преимущество при проведении измерений в неблагоприятных условиях (повышенная влажность, непостоянство температуры и др.).

В нормальном супергетеродине распределение частот показано на рис. 5.

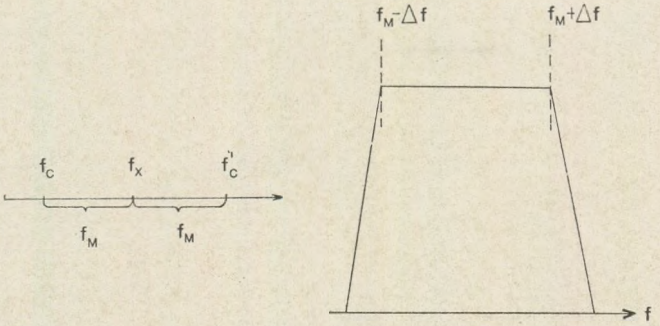

Рисунок 5. Распределение частот в нормальном супергетеродине

где:

f_c – частота принимаемого сигнала;
f'_c – частота зеркального канала;
f_x – частота гетеродина;
f_m – промежуточная частота.

Отношение $\frac{f_m}{f_m + \Delta f_m}$ очень близко к единице и требуемая селективность обеспечивается сложными резонансными системами.

В предложенный приемник распределение частот дано на рис. 6. где отношение $\frac{f_m}{f_m + \Delta f_m}$ значительно меньше единицы – например:

$$f_m = 30 \text{ гц}; \quad \Delta f_m = 90 \text{ гц}; \quad \frac{f}{f_m + \Delta f_m} = \frac{30}{120} = \frac{1}{4}.$$

Видно, что требуемая селективность при одной и той же полосе пропускания в этом случае может быть обеспечена более простым фильтром.

Ввиду того, что промежуточная частота очень низка, не требуется применение резонансного фильтра. В разработанной схеме приемника используется обычный низкочастотный RC фильтр.

Напряжение звуковой частоты на выходе приемника измеряется амплитудным вольтметром.

Принципальная схема приемника, собранного полностью на транзисторах, показана на рис. 7.

Входной усилитель выполнен на малошумящих транзисторах SFT –317. Основное усиление получается от первого транзистора, который имеет апериодическую нагрузку. Второй транзистор используется в схеме эмитерного повторителя с трансформаторным выходом. Для выравнивания усиления на разных частотах используется частотно-корректирующая цепь, которая связывает оба транзистора.

Питание входного усилителя стабилизовано с помощью кремниевого стабилитрона Д–808.

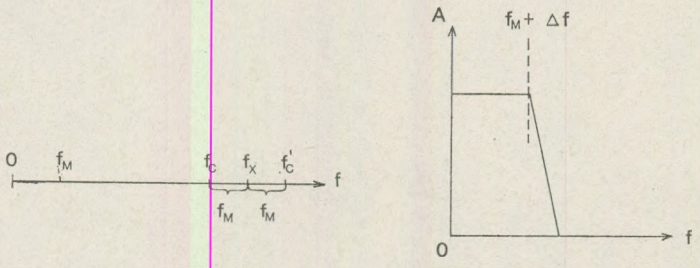

Рисунок 6. Распределение частот в предложенном приемнике

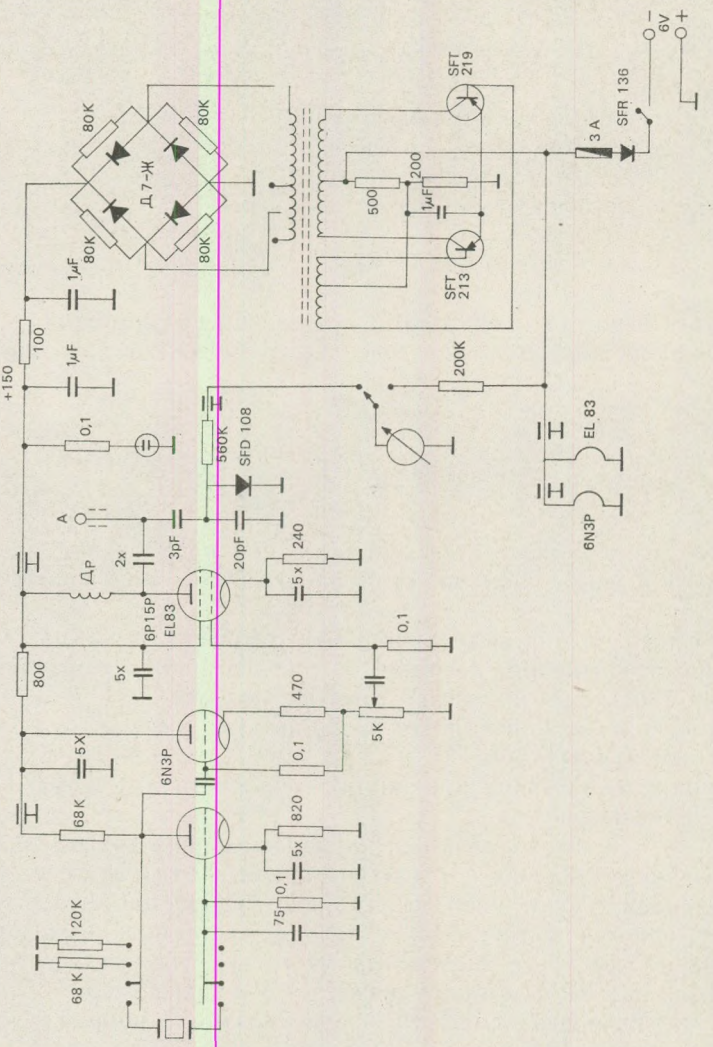

Рисунок 7. Принципиальная схема приемника

Гетеродин выполнен на двух транзисторах SFT–317 и имеет кварцевую стабилизацию частот. Превый каскад- это задающий генератор с кварцем, включенным между коллектором и базой транзистора. Нагрузка апериодическая. Второй каскад (эмитерный повторитель) буферный, что повышает стабильность частоты задающего генератора. Буферный каскад работает в режиме ограничения и ввиду этого амплитуда выходного напряжения гетеродина не зависит от рабочей частоты.

Смеситель выполнен на обычном диоде с трансформаторной связью.

Низкочастотный усилитель 3-х каскадный. В каждом каскаде используются два транзистора SFT–352 или SFT–353. Каждый каскад охвачен глубокой отрицательной обратной связью по постоянному и переменному току, благодаря чему режим и усиление всего низкочастотного усилителя остается стабильным при больших изменениях питающего напряжения и температуры. Ввиду этого не требуется постоянной регулировки коэффициента усиления приемника, что в большой степени упрощает работу с аппаратурой. После первого каскада включается аттенюатор, с помощью которого чувствительность приемника меняется ступенчато. Питающее напряжение второго каскада стабилизовано кремниевым стабилитроном Д–808. Напряжение на выходе низкочастотного усилителя измеряется амплитудным вольтметром с линейной шкалой.

Основные достоинства разработанной схемы приемника по сравнению с существующими в аналогичной аппаратуре заключается в следующем:

1. Частота, на которой проводится основная селекция, очень низка, вследствие чего простыми приемами достигнута селективность выше, чем при использовании высокой промежуточной частоты.

2. Величины сопротивлений и емкостей RC -фильтра определены путем расчета и поэтому отпадает необходимость в подстройке фильтра. Это улучшает технологические качества схемы.

3. Основное усиление осуществляется низкочастотным усилителем, который ввиду использования отрицательных обратных связей очень стабилен, независимо от неблагоприятных внешних факторов (температура, непостоянство питающего напряжения и др.). Это особенно важно при использовании в схемах транзисторов. Благодаря этому отпадает необходимость в калибровке при каждом измерении.

Конструктивно приемник выполнен в форме параллелепипеда (рис. 8.) размерами 230×155 и 130 и вес 2,3 кг вместе с батереями питания.

Техническая характеристика приемника следующая:

рабочие частоты f – 0,45; 1; 3,5 и 8 мгц;
потребляемая мощность – 11 – 17 вт×30–50 мА;
питание – 4 батареи×4,5 V, обеспечивающие непрерывную работу приемника в течение 20 часов;
чувствительность –0,33; 1; 3,3; 10; 33, 100 и 330 мкв для всей шкалы.

Уровень собственных шумов, приведенных к входу, не превышает 0,01 мкв.

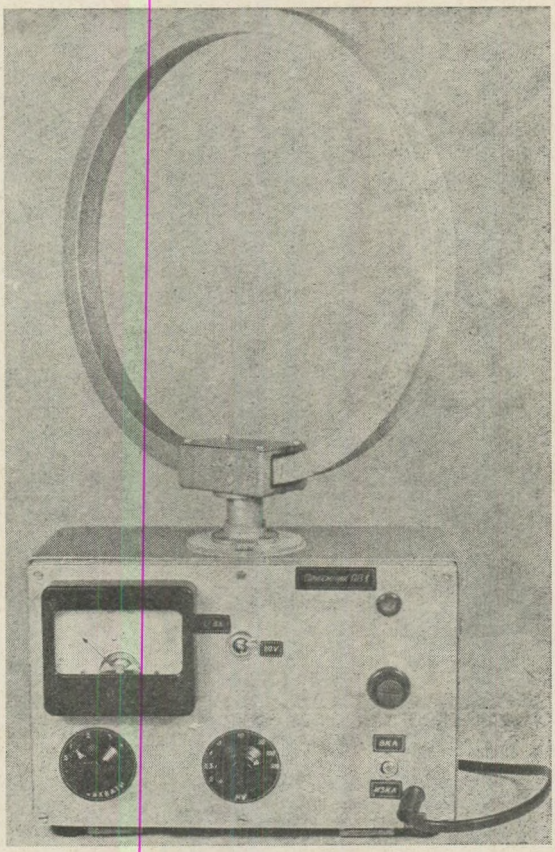

Рисунок 8. Общий вид приемника

В комплект антенн аппаратуры включены рамочные антенны 8 штук соответственно по четыре приемных и передающих для частот 0,468; 1,0; 3,0; и 8,0 мгц. Диаметр антени 30 см., вес 0,3 кг.

Штыревая передающая антенна. Рабочая длина 120 см. вес 0,3 кг. Предусматривается при необходимости использование дополнительных элементов для увеличения ее действующей высоты.

Для расширения технических возможностей применения метода радиоволнового просвечивания при подземных геологоразведочных работах, разработанный шахтный вариант аппаратуры дополнительно укомплектован миниатюрным скважинным передатчиком, работающим на фиксированной частоте 1 мгц. и скважинным приемником.

На рис. 9 показана схема скважинного передатчика. Задающий генератор стабилизован кварцем. Апериодическая схема выбрана ввиду ее высокой стабильности и отсутствия регулирующих элементов. Следующий каскад передатчика выполнен по схеме эмитерного повторителя.

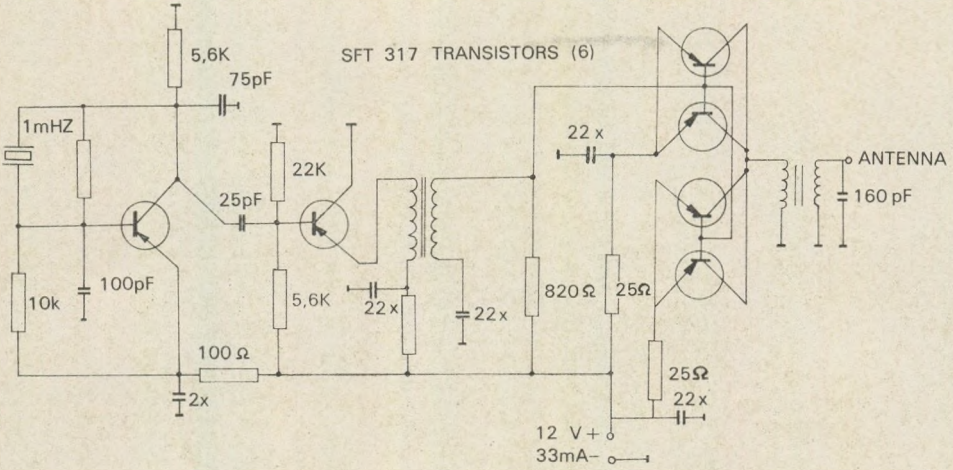

Рисунок 9. Принципальная схема скважинного передатчика

Оконечный каскад собран на нескольких маломощных высокочастотных транзисторах.

При параллельной работе нескольких транзисторов обычно они нагружены неравномерно и возможен выход из строя некоторых из них. В разработанном передатчике для устранения этого явления использованы два отдельных эмитерных сопротивления, а транзисторы в каждой группе подбираются. На выходе передатчика включен параллельный колебательный контур для настройки антенной цепи. Согласование с нагрузкой осуществляется с помощью трансформатора с ферритовым сердечником.

В качестве антенны используется кабель длиной 4м.

Внешний вид скважинного передатчика показан на рис. 10 а размещение электронной схемы в скважинном снаряде на рис. 11. Вес передатчика вместе с питанием 1,4 кг, диаметр 30 мм, длина 850 мм.

Техническая характеристика:

рабочая частота	– 1 мгц
выходная мощность	– около 0,2 вт
потребляемая мощность	– 12 V×33 МА.

Скважинный приемник состоит из высокочастотной приставки, включающей в себе приемную антену с автономном пытанием и низкочастотным блоком.

Для низкочастотного блока использована часть шахтного приемника в котором сохранен его основной принцип построения. Селективность достигнута на базе принимаемой и осциляторной частоте, с разницей друг от друга на нескольких сот герц. Схема высокочастотной приставки показана на рис. 12. Она состоит из четырёх германиевых транзисторов.

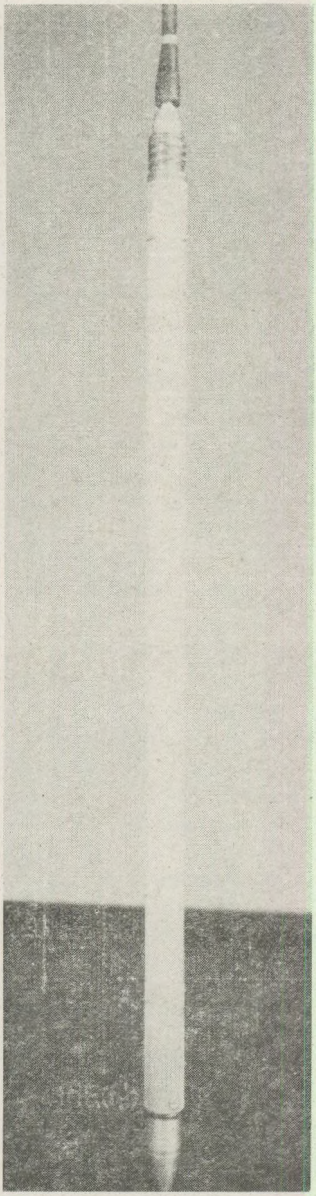

Рисунок 10. Общий вид скважинного передатчика

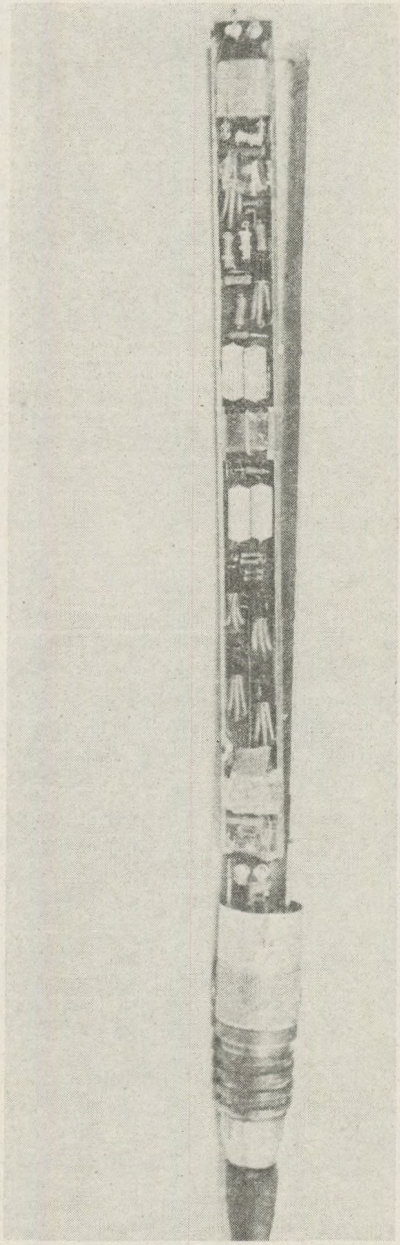

Рисунок 11 Размещение электронной схемы скважинного передатчика

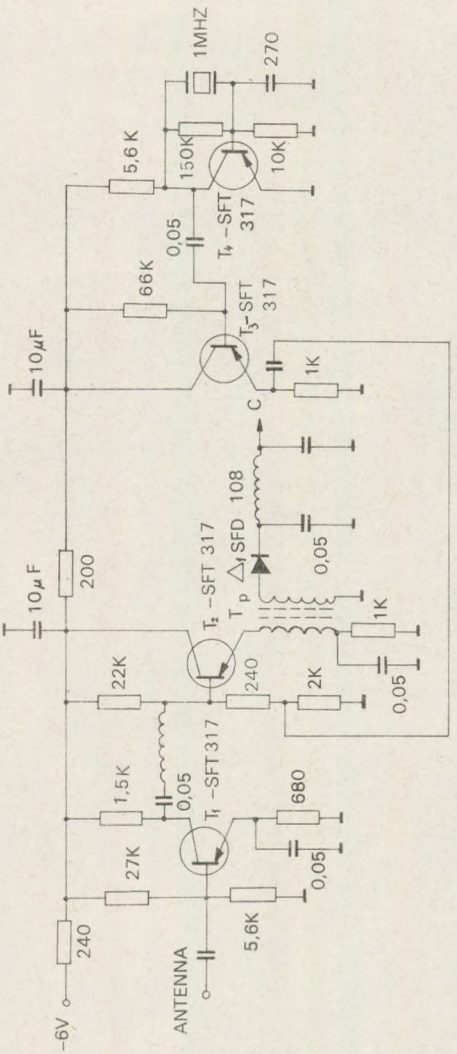

Рисунок 12. Схема высокочастотной приставки

Индуцируемый сигнал скважинного генератора через капацитет с минимальным значением перебрасывается на вход трептящего круга с самоиндукцией L_1. Далее сигнал подается к L_2 с коэфициентом трансформации 10 : 1. Транзистор T_1 SFT – 317 работает как широколентов усилитель с общим эмитером. Усиленный сигнал подается на транзистор T_2 SFT – 317, который работает как эмитерный повторитель. Одновременно с входным сигналом на базу T_2 подается сигнал от осцилятора T_4 SFT – 317. Смешивание осуществляется в диоде D_1, SFD – 108. После диода напряжение с частотой нескольких сот герц подается на низкочастотный П-фильтр со самоиндукцией L_3. Далее сигнал попадает на

специальном проводнике который связан с шахтным приёмником. Питание схемы осуществляется четырех элементов СЭЛ–2.

Конструктивно зонд состоит из двух частей: металлическая труба с внешним диаметром $d = 40$ мм и длиной $l = 700$ мм, в которой размещена электронная схема вместе с питанием и пластмасовую трубу с диаметром $d = 40$ мм и длину $l = 1500$ мм, в которой поставлена антена. Общая длина зонда 2200 мм.

Опробование разработанной аппаратуры в различных геофизических условиях показало, что она отвечает основным требованиям производства. При изменении сопротивления вмещающих пород в пределах от 60 до 400 омм дальность действия меняется соответственно от 60 до 140 м. для частоты 0,468 мгц и от 20 до 70 м для частоты 8 мгц. Аппаратура характеризуется большой стабильностью работы, а ее портативность и простота обслуживания обеспечивают высокую производительность наблюдений.

На основании результатов производственного испытания аппаратуры и многообразия задач, предстоящих к решению в условиях месторождений с различными геоэлектрическими характеристиками, намечены следующие основные направления по ее дальнейшему усовершенствованию:

а) увеличение дальности действия путем повышения чувствительности приемника;

б) разработка и включение в комплект аппаратуры устройства для прямой радиосвязи операторов, обслуживающих передатчик и приемник, что особенно необходимо при радиопросвечивании между двумя горизонтами.

ЛИТЕРАТУРА

Иванова В., Пищалов С., Мутафов С., 1968.: Ефективност на метода на радиоволновото просветяване в условията на оловно-сребърното находище «Чипровци». Сборник на трудове – НИС ВМГИ.

Несынов Ю. В., 1968.: Фазовые двухчастотные измерения в радиоволновых методах. Известия ВУЗОВ. Геология и разведка, кн. 1.

Петровский А. Д., Изюмов И. Ф.: Вариант аппаратуры и методики радиоволнового просвечивания из скважин. Труды ЦНИГРИ, вып. 33. 1959.

Светов Б. С., Петровский А. Д., Ершов Е. М. Каменецкий Ф. М. и др., 1966. Электромагнитные методы разведки в рудной геофизике. Изд. Недра, Москва.

Kaspar Milan, 1967.: Spolencue Ceskoslovensko-nemerue dulni geofizikalni mereni junzni oblasti Zlatich Hor Geol. pruzkum, no. 11.

Kaspar Milan, 1964.: Messapparatus für die neuen radiotechnische Bohrlochverfahren – Freiberger Forschungs., no 226.

Kelleuer R., 1966.: Some statistical properties of the ground diffraction patterns of vertically reflected radio waves. Atmos and Terr. Phys., N. 2.

Pistaloff St., Ivanova W., 1969.: Die Effektivität der unterirdischen geophysischen Methoden unter den Bedingungen der Blei-silber „Tschiprovzi", Geophys. und Geologie, Folge 13, Leipzig.

INDEX

A kiadásért felelős: az Eötvös Loránd Tudományegyetem rektora — A kézirat nyomdába érkezett:
1978. november — Megjelent: 1979. december — Terjedelem: 14,5 (A/5) ív +1 melléklet —
Példányszám: 1550 — Készült monó szedéssel, íves magasnyomással,
az MSZ 5601—59 és az MSZ 5602—55 szabvány szerint

79.1147. Állami Nyomda, Budapest
Felelős vezető: Bresztovszky Péter igazgató